The Evolution of Damage in Ceramic Matrix Composites

Thesis by

Mark E. Walter

In Partial Fulfillment of the Requirements

for the Degree of

Doctor of Philosophy

California Institute of Technology

Pasadena, California

1996

(Submitted 09/26/95)

Zum Andenken an:

Martha und Albert Elser & Maria und Eugene Walter.

To Mom and Dad.

"Because what we can achieve technically has always been limited by the weaknesses of the materials of construction this new science [the science of strong materials] is important. Instead of accepting our materials as something provided, arbitrarily, by Providence – as people used to until very recently – we can understand why they behave as they do and moreover, we can see much more clearly how they might be modified and improved. As a consequence, we are beginning to see our way to making radically better materials, unlike anything which has existed before, and they may open up quite new possibilities to the engineers."

J.E. Gordon, *The Science of Strong Materials*
(or Why you don't fall through the floor)

Acknowledgments

Acknowledging those who have helped me during the five years that I have spent at Caltech is a non-trivial task. It is especially troubling that I cannot mention all the names of people who have made my stay here more pleasant and more fulfilling. Although I have always made it sound like Caltech was all work and no play, there are many people with whom I have played various sports, several with whom I have spent time exploring California's wilderness, and many who have endured my presence during parties, barbecues, dinner parties, *etc.* Thanks to all of you for sharing these times with me.

My parents, to whom this work is dedicated have supported me in countless ways. Their love and encouragement has brought me to where I am. It would be remiss not to also mention the loving support of my brother and sister. When I began studying at Caltech three of my grandparents were alive. In these five short years all of them have now passed away. I carry many of their values and dreams, and it deeply saddens me that they are not here to share in my life. This thesis is written with their memory in mind.

I believe that it will be hard to find a more efficient and enjoyable place to study and do research. I have benefited immensely from the presence of dedicated secretaries and staff. In particular, I would like to thank Joe Haggerty in the machine shop for helping me in all phases of my experimental research and Oon-Gil Paik his help keeping our computer cluster running. The often demanding environment at Caltech is made bearable by fellow students. I am particularly fortunate to have had Dr. C.R. Schultheisz to teach me how to navigate the GALCIT labs; Dr. P.H. Geubelle for showing me how to work hard and play hard; Dr. G. Vendroux for teaching me electronics and how to work a DSP; Dr. W. Chen for many laboratory collaborations; and Dr. D.M. Owen for his array of laboratory skills and help with last minute SEM photos. I am also lucky that Gustavo Gioia and Eduardo Repetto arrived when they did to listen to my complaints and to make suggestions regarding my trials with finite elements. No acknowledgment of supporting colleagues would be complete without mentioning Dr. J.M. Lambros. Our discussions, both technical and non-technical, were certainly one of the most enjoyable parts of living and working at Caltech.

All of the professors whom I have worked with or taken classes from have taught me a great deal. I am especially lucky to have had 9 terms worth of courses with Professor J.K.

Knowles, whose rigor, consistency and good humor in the classroom are second to none. Professor W.G. Knauss deserves my thanks for showing me the importance of physical insight into mechanics problems and for generosity with GALCIT resources. I have also benefited from having taken classes from and discussing fracture mechanics with Professor A.J. Rosakis. In the last few weeks of my work, I have spent an inordinate amount of time with Professor J.F. Hall. As well as having taught me finite element basics three years ago, Professor Hall has more recently taught me what it means to be rigorous in research. Without his encouragement I would have left several important issues "unfinished." I also hope that I can emulate the way Professor Hall gave me his undivided attention each time that I stepped into his office. The numerical phase of my research could not have been attempted without the help of Professor M. Ortiz. He has been extremely generous in providing me with finite element code and in spending time with me to explain many mechanics and numerical issues. Considering what I have learned from Professor Ortiz, I am quite fortunate that his time at Caltech has coincided with my stay here. No acknowledgments would be complete without many thanks to my advisor, Professor G. Ravichandran. He has given me the freedom and resources to pursue my own ideas, and he has steered me back on course with his incredible knowledge base and intuition. Thanks to his generosity, I have had the opportunity to attend several major conferences throughout the country. I think that Professor Ravichandran's advice regarding presentation of oneself and and one's research will benefit me greatly in the years to come. I am most fortunate to have had Professor Ravichandran as my advisor during my time at Caltech.

Financial support for my studies and research has come from a variety of sources. The Mechanical Engineering and Applied Mechanics Departments initially provided with me a TA and subsequently funded me through a C.L. Powell Fellowship. The Aeronautics Department has also generously provided me with various TAs and other sources of funding. My research has been funded primarily by a Presidential Young Investigator award from the National Science Foundation to Professor G. Ravichandran, grant number MSS-9157846. In addition, Digital Signal Processing hardware and software was donated by Motorola, and many hours of Cray CPU time have be provided by the Jet Propulsion Laboratory through the Caltech Concurrent Supercomputing Facilities. All of this support is gratefully acknowledged.

Abstract

In an effort to better understand the evolution of damage in brittle matrix composites, the mechanical behavior of a ceramic matrix composite, unidirectional SiC/CAS (SiC fibers reinforcing a calcium aluminosilicate matrix), was studied. The presented results are based on uniaxial tension experiments for specimens with the fibers aligned in the loading direction. Post-test optical and scanning electron microscopy was also used to identify the various micromechanisms of damage; axial and transverse strain gauges on all four gage section surfaces and *in situ* acoustic emission and ultrasonic wave speed measurements were used to monitor the evolution of damage. The experimental results demonstrate the existence of "zones of deformation" which are associated with the onset of different damage mechanisms. The energy dissipated in each of these zones was calculated. It is shown that the observed stress-strain behavior can be qualitatively explained in terms of the material properties of the matrix and the fiber, the material processing, and the postulated zones of deformation.

The experimental results for SiC/CAS were compared with an existing shear-lag model, and the shortcomings of the model are discussed. By approximating matrix cracks as penny shaped cracks, a micromechanical model was used to estimate the change in the axial modulus of the composite. These results also present another way to interpret the acoustic emission data.

The evolution of damage in the SiC/CAS experiments was found to be strain rate dependent even within the quasi-static strain rate regime. For higher rate experiments, the transition from elastic to matrix cracked occured at a stress level that was nearly twice that of the same transition in the lower rate experiments. This phenomenon and the mechanisms which cause it was further investigated with a model material system (a brittle epoxy resin sandwiched between aluminum strips). *In situ* quantification of the stress during damage initiation and propagation was realized by the optical method of Coherent Gradient Sensing. Based on these results, the reasons for strain rate dependence of the composite are postulated.

Detailed understanding of aspects of the evolution of damage in brittle matrix composites was achieved with finite element simulations. This modeling was based on an axisymmetric unit cell composed of a fiber and its surrounding matrix. The unit cell was discretized into linearly elastic elements for the fiber and the matrix and cohesive elements which allow cracking in the matrix, fiber-matrix interface, and fiber. The cohesive elements failed according to critical stress and critical energy release rate criteria (in shear and/or in tension). After failing, the cohesive elements could slide with Coulomb friction. The tension and shear aspects of failure were uncoupled. The cohesive elements were used to simulate a Dugdale penny shaped crack in a homogeneous cylinder; results compared well to the analytical solution. In order to solve the composite axisymmetric unit cell problem, inertia and viscous damping were added to the formulation. The resulting dynamic problem was solved implicitly using the Newmark Method. Results were compared to the experiment by assuming that only a given number of unit cells were active at any point during the simulation. The effects of changing material properties (*e.g.*, interface strength and toughness and matrix toughness) and loading rate are discussed. Several aspects of the experimentally observed material response of SiC/CAS composite were reproduced by the numerical simulations.

Table of Contents

List of Figures

CHAPTER 1

Introduction

1.1 Motivation

A large part of the engineering community is devoted to finding ways to move faster and further more efficiently and with reduced cost. Examples of projects which embody these wishes include safe, lightweight, high speed, reliable and efficient land, sea, air and spacecraft; using and developing alternate energy sources; and replacing and developing infrastructure. These applications reflect not only the desires of consumers, but they are also key ingredients for providing a sustainable future.

Future engineering applications require materials which are lightweight and can withstand the hostile environments (high temperatures, chemical reactivity, wear situations, high loads, impact, fatigue, *etc.*) in which they must function. It is believed that the main limitation to rapid advancement of technology is not a lack of design ideas, but rather, the availability of materials with "high performance" properties. Not only must advanced materials be developed, but they must also be understood before they can be used in engineering design.

Candidate materials for future engineering applications include monolithic ceramics, intermetallics, nano-crystalline materials, graded materials and ceramic matrix composites. Although conventional metallic materials can typically provide the required toughnesses for structural applications (*i.e.*, they are able to withstand over stressing without catastrophic failure), they generally have high mass density and are incapable of sustaining high temperatures. Monolithic ceramics, on the other hand, are highly refractory but lack the required

toughnesses. Ceramic composites take advantage of the refractory nature of the ceramic constituents while increasing toughness through energy absorbing damage mechanisms. This has placed ceramic matrix composites at the forefront of advanced materials research.

The process of developing advanced materials for engineering applications could proceed as shown in Fig. 1.1.1. A range of experiments are performed to obtain the material response directly and also to determine the damage mechanisms active during a particular loading history. Through modeling efforts, knowledge of the damage mechanisms also yields the material response. Valuable information regarding life prediction could be extracted from suitable models. Once the material response is known (particularly in terms of the active damage and deformation mechanisms), it is probable that improvements could be made through processing and constituent selection optimization. From a futuristic point of view, material selection would be a simple matter of the design engineer specifying the desired constitutive behavior in terms of material requirements such as stiffness, ultimate strength, operating environment and expected life. A model would then iteratively determine the optimal material system and manufacturing parameters. Presumably, the model could generate this information because known damage mechanisms would be associated with each material system and manufacturing process. In any case, before ceramic matrix composites can be reliably incorporated into designs, viable models for predicting the constitutive behavior under thermomechanical loading conditions are required. The first step in such a modeling effort requires fundamental understanding of the initiation and accumulation of internal damage for a particular composite system. Experimental investigations are seen as a means of determining and quantifying the relevant damage mechanisms.

1.2 Review

Although the word "composites" conjures up images of ultra-modern materials, composites in various forms have been used for at least 5000 years. There are biblical references to reinforcing bricks with straw, and roadways in ancient Babylon were made with rein-

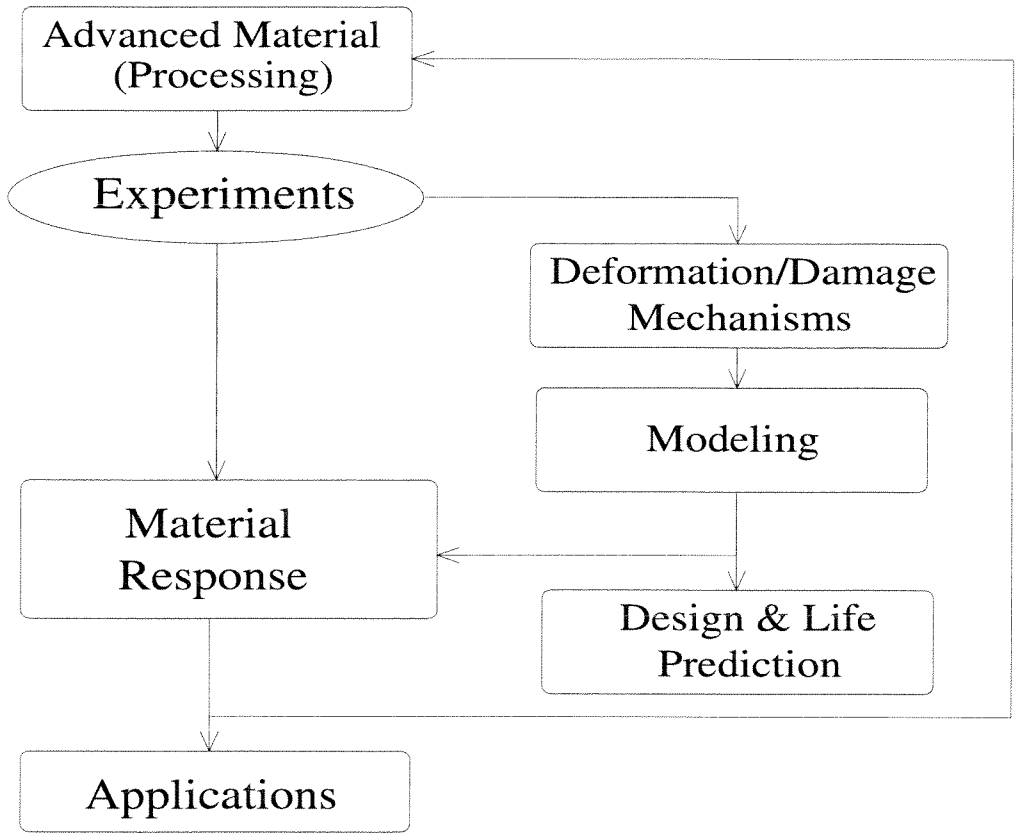

FIG. 1.1.1 The role of experiments in advanced materials research and development.

forced bitumen.* Paper and concrete are both composites and were well known in Roman times. In actuality, many natural load bearing materials (*e.g.*, wood, bone, muscle) are also composites, implying that composites have been in existence forever.

The development of composite structures other than roads and buildings is significantly more modern. Papier-mâché, a composite known to most elementary school students, was used in ancient times, and it was then revived and used in World War II for fuel tanks and other aircraft parts. The use of more common resins began in the early 1900's with the invention of Bakelite resin, and then in the 1920's with phenolic resin. Both of these materials could be molded into complicated shapes. Bakelite was often reinforced with whiskers or particles. Phenolic resins were often reinforced with cellulose, and significant

* An asphalt of Asia Minor used in ancient times as a cement and mortar.

effort was put into developing cellulose-reinforced sheet to replace aluminum sheet in aircraft during World War II. This effort was unsuccessful because of the expansion and contraction of the composites in various (not necessarily extreme) environmental conditions.

Towards the end of World War II, inorganic fibers were introduced. This is what led to the growth of the composites industry and to the general sense that composites are modern, high-tech materials. In particular glass fibers and their use in "fiberglass" changed the composites industry. Although the trend is towards high stiffness composites, it is instructive to mention a few facts about fiberglass. Some of the earliest fiberglass structures were radomes.** Now, high performance racing cars, and nearly all recreational boats are made of fiberglass. It is noted that these are all shell like structures. This takes advantage of the directional properties of composite materials. Metals are generally isotropic; therefore thin shells of metal dent and buckle easily. The limitation of fiberglass is that its work of fracture is on the order of 70 kJ/m^2 which is low compared to steel. The low toughness leads to reduced crash worthiness, and this fact has left fiberglass with only a limited role in the automotive industry.

Although the toughness of fiberglass is low compared to steel, it is relatively high, considering that the toughnesses of the individual constituents is extremely low. Although stiffness (and to some degree, strengths) are linear combinations of the composite components, toughness is certainly not. The work of fracture of composites is greatly enhanced by crack trapping and crack bridging combined with frictional sliding and pull-out. The existence of these toughening mechanisms has given researchers hope that materials composed of more brittle components could be made "useful" in composite form. This is desirable since more brittle components are generally much stiffer and have better high temperature and wear characteristics. Thus, research into high stiffness composites began.

Experimental investigations into fiber reinforced composites did not begin in earnest until the mid 1960's. These early investigations typically dealt with materials such as

** Dome-like fiberglass structures which housed radar scanners during World War II.

carbon fiber (graphite) reinforced epoxy. The work by Cook and Gordon (see Gordon, 1979) contains some of the earliest studies of fiber bridged matrix cracking. Ceramic matrix composites lagged behind because they were difficult to manufacture and therefore were expensive and wholly unpredictable. Glass-ceramic composites were first to be manufactured since the glassy phase allows the ceramic to flow at lower temperatures. Since the early 1970's, advances in highly refractory, high stiffness fibers has enabled researchers to consistently produce glass-ceramic matrix composites which do not fail in a completely brittle fashion. Philipps (1974) was one of the first to study a glass-ceramic matrix which was reinforced with carbon fibers. These composite materials have low density, are chemically inert and have some degree of toughness. However, the glassy phase in the matrix and the carbon fibers led to less-than-spectacular high temperature capabilities. In addition, these materials have a relatively low ultimate strength, even when the fibers are aligned in the loading direction. As is typical for fiber reinforced composites, tensile strengths are non-existent under off axis loading. The next advanced composite material beyond glass-ceramic matrix composites are fully crystalline ceramic composites. Although these materials provide improved stiffness, strength and temperature resistance, they are still difficult and expensive to manufacture. However, since materials processing technology is constantly improving, these ceramic composites will most likely play important roles as future high temperature structural materials. Despite the limitations associated with glass-ceramic matrices, due to significant innovation in fiber technology coupled with the continued difficulties in processing fully crystalline ceramics, glass-ceramic composites remained readily available as a research material.

In the early 1980's a high strength SiC fiber by the name of Nicalon (Nippon Carbon Co., Yokahama, Japan) was introduced. These fibers are readily available in bulk, and this has led to a tremendous amount of brittle matrix composites (BMC) research using glass-ceramic matrix composites. The first Nicalon composite system commonly available to the research community was Nicalon SiC fibers reinforcing Lithium AluminoSilicate

(LAS) which was produced at UTRC (United Technologies Research Center, Hartford, Connecticut) by Brennan and Prewo (1982). The early work with SiC/LAS dealt primarily with presenting the mechanical behavior and identifying the damage mechanisms (Brennan and Prewo, 1982; Mah *et al.*, 1985a; Marshall and Evans, 1985). With regards to the development of tough composites, this research into mechanical behavior was important in that it showed which micromechanisms were important enough to require individual attention.

Previous studies (Marshall and Ritter, 1987; Evans, 1990) have shown that toughening in BMCs is achieved by the energy absorbing processes of damage development. It is well known (Ashby and Jones, 1980) that although the toughnesses of each individual constituent in a composite are quite low, the crack trapping and deflection and frictional sliding in composites can lead to relatively large toughnesses (work of fracture). The following toughening mechanisms have been identified for fiber reinforced ceramic matrix composites: matrix cracking, fiber bridging, debonding and delamination, and fiber pull-out. In their review article, Evans and Marshall (1989) present analytical results for several of the individual micromechanisms. Much of the early work was done with flexural loading conditions. This creates non-uniform and to some extent unknown stress fields within the specimen. More recently Sorensen *et al.* (1992), Daniel *et al.* (1993) and Walter and Ravichandran (1995) have performed tension tests and characterized damage for the full loading history.

Recent research in brittle matrix composites has also branched into areas related to the individual damage mechanisms. Most models of matrix cracking which include bridging effects are based primarily on the shear-lag concept (see Section 3.1). However, there are also models which have modified the shear-lag approach. Danchaivijit and Shetty (1993) use a new shear-lag formulation with a stress intensity approach which accounts for bridging and frictionally sliding fibers. Dharani and Tang (1990) have used a modified ("consistent") shear-lag model which allows the matrix to carry normal stress as well as shear stress. This

approach is logical since for brittle matrix composites, the matrix is nearly as stiff as the fibers and thus initially carries a significant portion of the load. There are also matrix cracking investigations which do not incorporate the shear-lag concept. Weitsman and Zhu (1993) have based their matrix cracking analysis on an energy criterion, as have Kuo and Chou (1995). Wijeyewickrema and Keer (1991) have used fracture mechanics to analyze various potential crack configurations in fiber composites. Pagano and Brown (1993) have developed an axisymmetric full-cell cracking model; this model can also account for non-uniform fiber distributions which are believed to play an important role in matrix cracking (Sørensen *et al.*, 1992). Curtin (1993) has developed a model which includes fiber breaks and Weibull statistics. Spearing and Zok (1993) have also considered statistics of initial flaw distributions in determining the evolution of crack density. Similarly, Cho *et al.* (1992), theorized that local variations in matrix strength will have significant influence on the spacing of matrix cracks.

There are many experimental investigations into matrix cracking. By making surface replicas of tensile composite specimens Kim and Pagano (1991) have studied the initiation and propagation of matrix cracks. Beyerle *et al.* (1992), Pryce and Smith (1992) and Wang and Pavizi-Majidi (1992) have experimentally observed the development of matrix cracks and have provided plots of the matrix crack density for the compete loading history. Some authors have used acoustic emission to qualitatively visualize matrix cracking (*e.g.*, Kim and Pagano (1991); Harris *et al.*, 1992; Walter and Ravichandran, 1995).

For all of the active damage mechanisms in ceramic matrix composites, the interface between the fiber and the matrix plays a key role. Thus, another large fraction of the research effort to toughen BMCs has focused on the fiber-matrix interface (*e.g.*, Kerans *et al.*, 1989). This specialization has taken the form of numerical, analytical and experimental investigations and models. It has been postulated that the fiber-matrix interface properties determine the extent of fiber pull-out (Evans and Marshall, 1989; Kerans *et al.*, 1989) and have important effects on material response (Cao *et al.*, 1990; Llorca and Singh, 1991). Fiber

pull-out and push-in tests have been developed to study the energy dissipation of the fiber pull-out process (Marshall and Oliver, 1987) and to determine interface properties (Weihs and Nix, 1991; Laracurzio and Ferber, 1994). More recently a "microcomposite" specimen (a single coated fiber surrounded by an annulus of matrix) was developed for determining interface properties (Lamon *et al.*, 1995). Among others, Kerans and Parthasarathy (1991), Freund (1992) and Marshall (1992) have developed models of the pull-out/push-in process. The effect of temperature on the fiber-matrix interface properties has important implications for the thermomechanical response of ceramic matrix composites. These implications are outlined below, within the context of high temperature testing of ceramic matrix composites.

Fiber-matrix debonding has also been investigated. Charalambides and Evans (1989) and Hutchinson and Jensen (1990) have developed analytical models of debonding which take residual stresses and frictional sliding into account. Dharani and Recker (1991) have used their consistent shear-lag model to study initiation and propagation of debonding. More recently Budiansky *et al.* (1995) approximate the stresses need to initiate and propagate fiber-matrix debonding from a matrix crack. Experimentally, due to the difficulties in visualizing debonding, relatively little work has been done in the area of debonding. However, the experimental works of Wooh and Daniel (1994) and Walter and Ravichandran (1995) have used ultrasonics to investigate debonding.

Ceramic matrix composites were originally proposed as the high temperature material of the future (Katz and Kerans, 1988). Despite this proposition, there has been relatively little high temperature work with ceramic matrix composites. Most likely one of the first high temperature investigations with a glass-ceramic composite reinforced with Nicalon SiC fibers was that of Prewo and Brennan (1980). For temperatures up to 700°C no degradation in material properties was observed. Since then authors (Mah *et al.*, 1985; Luh and Evans, 1987; Prewo *et al.*, 1989) have found that there is a transition to a brittle, notch sensitive material at temperatures greater than 1000°C. Attention has focussed on embrittlement of the interface as the primary cause for this transition (Bischoff *et al.*, 1989; Kim *et al.*, 1991).

Since creep is an important issue at high temperature, researchers have also focussed on determining the mechanisms of creep (Wu and Holmes, 1993; Weber *et al.*, 1994). Park and Holmes (1992) have modeled the high temperature creep process with finite elements. Meyer *et al.* (1993) used creep to characterized the interface and found that an amorphous SiO_2 layer flows viscously at high temperatures.

Many engineering materials must be able to function in fatigue environments, and within their realm of proposed applications, ceramic matrix composites provide no exception. Fatigue has been investigated by Butkus *et al.* (1993) at high temperatures. It has been found that the matrix damage and matrix creep at high temperatures is the limiting factor for fatigue life of ceramic matrix composites. Interesting studies of frictional heating by Holmes and Cho (1992) have found temperature rises of more than 100°K during fatigue loading of a ceramic matrix composites.

Unidirectional fiber composites have meaningful strength only in the fiber direction. It is clear that in actual applications, composite laminates will be used. There is a large body of research into epoxy matrix laminates; much of this work regards determining the effective elastic properties (see Hashin, 1983). Only more recently have ceramic matrix composite laminates been investigated (Wang and Parvizi-Majidi, 1992; Xia and Hutchinson, 1994; Daniel and Anastassopoulos, 1995). Most of this work with laminates is concerned with determining when and how cracks propagate through the different laminates. More recently Kuo and Chou (1995) have developed an energy criterion for evaluating the onset of damage in cross-ply ceramic matrix composites. Other studies have concerned themselves with macro crack (notch) propagation in ceramic composite laminates (*e.g.*, Cady *et al.*, 1995). A new technique for examining damage uses SPATE (stress pattern analysis from thermoelastic emission) to measure small temperature changes associated with changes in hydrostatic stress (Mackin *et al.*, 1995). This technique has been used to study damage in notched ceramic matrix composites. In addition, fatigue studies with laminates have also been performed (Habib *et al.*, 1993; Karandikar and Chou, 1993).

This brief review of composites in general and ceramic matrix composites in particular shows that composites have been in existence for a long time and that there is a large body of research related to composites (particularly in the last decade). However, extensive research will continue into the future since the improved understanding of the mechanical response of composites together with the improvement of processing methods will increase the use of composites in practical applications.

1.3 Approach and Objectives

Since future ceramic matrix composites are of the same system as glass-ceramic composites (*i.e.*, stiff fibers reinforcing a brittle matrix), investigations with glass-ceramic composites are also relevant for future composites applications. In addition, by placing the existence and evolution of damage in terms of fundamental mechanics, it is anticipated that many of the results encountered with glass-ceramic composites can be applied to other composites systems. As was mentioned above, in actual applications, composite laminates will most likely be used. Despite this fact, only unidirectional composites are studied in the present investigation. This specialization is required because composite properties are best in the fiber direction, and improvement of composites as an overall structural material will occur only if properties in the fiber direction are improved. Furthermore, unidirectional composites are the building blocks of laminates, and therefore fundamental understanding of unidirectional composites is necessary for understanding laminate response.

Determining the existence, sequence and extent of damage mechanisms in unidirectional brittle matrix composites is the main goal of this investigation. A secondary, but equally important goal is determining the effects of strain rate on the damage process. The realization of these goals is attempted through a combination of experiments and numerical simulations.

In the next chapter, experiments with a glass-ceramic matrix composite (unidirectional SiC reinforcing a calcium aluminosilicate matrix) are described. Post-test microscopy was

used to establish the existence of different damage mechanisms. *In situ* strain, ultrasonic and acoustic emission measurements were used to track the evolution of damage. The results indicate that there are "zones" which are dominated by individual damage mechanisms. In addition the percentage of the unrecoverable energy absorbed by each zone (damage mechanism) is estimated. A separate chapter is devoted to analyzing the usefulness of two models of matrix cracking.

The effect of strain rate on the damage evolution is studied in Chapters 3 and 4. In Chapter 3 the same composites studied earlier were tested at two different strain rates within the quasi-static strain rate regime. Significant changes in the material response were observed. A model composite system was designed and tested at various strain rates; the results are presented in Chapter 5. Similarities to the response of the actual composite were noted. The advantage of the model system was the ability to make full-field optical measurements in order to observe the evolution of damage.

In the final chapter numerical simulations with a unit cell composite are described. Parametric studies with the interface toughness and strength and matrix toughness were performed. In addition, the propagation of matrix cracks and the initiation of debonds was observed. Several aspects of the experimentally determined material response of SiC/CAS composite were reproduced by the numerical simulations.

CHAPTER 2

Ceramic Composite Experiments

2.1 Introduction

Experiments were undertaken to understand the details of how ceramic matrix composites deform. The ceramic matrix composite used for these experiments was a research material called SiC/CAS (calcium aluminosilicate reinforced with silicon carbide fibers). An array of different measurements were made and based on these measurements and on observations, the deformation (damage) history is postulated. All experiments were performed with unidirectional composite specimens and the load was always applied in the fiber direction. The results presented in this chapter are all for "lower" strain rates. Interesting changes in material response arise when the strain rate is increased. Chapter 4 is devoted to these "higher" strain rate experiments.

Until very recently, much of the testing of ceramic matrix composites has been flexural testing. This has been primarily because of the complications in designing specimens and grips for valid tension experiments. However, flexural specimens are loaded by non-uniform stress fields, making the interpretation of damage evolution difficult. This has been realized, and since approximately 1990 various specimen geometries and gripping methods have been presented for tension testing of ceramic matrix composites. Cranmer (1991) has grouped these methods into the following categories: pin-loaded, edge-loaded, and tabbed, and he summarized the advantages and disadvantages of each. To date, there is still no published standard for tension testing of ceramic matrix composites or monolithic ceramics.

Previously published experimental work in ceramic matrix composites has been outlined in Chapter 1; most of the research referenced therein is with SiC/CAS. Throughout this chapter, reference will be made to only relevant published research. The CAS matrix is preferred over other glass-ceramic matrices because it is nearly fully crystalline (>99%). This gives it better high temperature performance and more closely resembles future fully crystalline ceramic composites (*e.g.*, SiC/SiC, SiC/Al_2O_3).

Although it is clear from Chapter 1 that there is a large body of research on brittle matrix composites, it is believed that there are still fundamental issues to be resolved. For this reason work is continued with a unidirectional composite system with loading in the fiber direction. The results presented in this chapter are unique in that the postulated deformation mechanisms are used to explain macroscopic measurements. In addition, several new observations and measurements have been made. This chapter proceeds as follows: after introducing specifics related to the SiC/CAS material system, the experimental procedure is presented. Particular attention is given to the specimen and grip design and strain, acoustic emission and ultrasonics measurements. The next section of the chapter is devoted to presentation and discussion of the experimental results and observations. Based on these results, the history of damage evolution is postulated in the subsequent section. The chapter concludes with a brief summary.

2.2 Material System

The experimental Brittle Matrix Composite (BMC), used in the present investigation was obtained in plate form from Corning Inc. (Corning, New York). The silicon carbide fibers are Nicalon SiC (Nippon Carbon Co., Yokahama, Japan) and the matrix material is Corning CAS-II (calcium aluminosilicate). This composite is commonly called SiC/CAS and is available in various layups (fiber orientations). As the introduction indicated, this material is quite prevalent in the research community; however, to date, it is not used in any engineering applications. For the present study, only unidirectional specimens

were investigated. The as-received plate consisted of eighteen 0° plies corresponding to a thickness of approximately 3.25 mm.

The following information regarding the manufacture of SiC/CAS is known (Stuart, 1992). An organic binder is used to impregnate SiC fiber tows (bundles of fibers) with a slurry of CAS matrix material, and then the fiber tows are laid out to dry as 12 x 36 inch sheets. Next, this sheet is cut into 6 inch square pieces which are stacked on top of each other in the desired orientation (in the present case, 18 plies are all aligned in one direction). The stacked plies are then heated to burn off the majority of the binder. The material is subsequently hot pressed, starting at around 2000 psi and 1400 °C. The pressure and temperature are gradually decreased until at approximately 850 °C the material is under atmospheric pressure only. Various known properties of the individual phases and the composite are shown in Table 2.1. It was shown that the glass-ceramic composite, SiC reinforcing Lithium AluminoSilicate (LAS), is actually a four phase material with an interface between the fibers and matrix composed of a layer of carbon and NbC layer (Bischoff *et al.*, 1989). During heat treatment part of carbon layer is replaced by SiO_2 and the Niobium oxidizes. Similarly, Meyer *et al.* (1993) report that SiC/CAS also is a four phase material. In addition to the fiber and the matrix, there is a carbon layer and a SiO_2 layer around the fiber. Although both of these interface layers are extremely thin, they are not well understood. According to Cooper (1994), it is possible that the carbon layer is porous, and it is probable that the fiber changes from amorphous to polycrystalline during the processing of the composite. The experiments described in this chapter were performed on two batches of material which differed in their fiber volume fractions. Values reported in Table 2.1 are for the first batch with a 41% volume fraction of fibers. Additional experiments were performed with 50% fiber volume fraction SiC/CAS composite. No attempts were made to compare results from the different batches.

Table 2.1: Material Properties of SiC/CAS-II

Material	Property	Value
Fibers (SiC)	Young's Modulus$^{\diamond}$ (E_f)	190 GPa
	Ultimate Strength$^{\diamond}$	1300 MPa
	Thermal Expansion Coef.† (α_f)	$3.1 \times 10^{-6}\,^{\circ}C^{-1}$
	Strain to Failure (ϵ_f^f)	0.87 %
Matrix (CAS II)	Young's Modulus† (E_m)	88 GPa
	Shear Modulus‡ (G_m)	42 GPa
	Thermal Expansion Coef.† (α_m)	$4.5 \times 10^{-6}\,^{\circ}C^{-1}$
	Poisson's Ratio‡ (ν_m)	0.26
	Strain to Failure† (ϵ_m^f)	0.15 %
	Glass Transition* (T_g)	850 °C
Composite (CAS II/SiC)	Density (ρ)	2.7 g/cm^3
	Young's Modulus (E_3)	130 GPa
	Transverse Modulus (E_1, E_2)	120 GPa
	Shear Modulus (G_{12})	49 GPa
	Major Poisson's Ratio (ν_{31})	0.29
	Minor Poisson's Ratio (ν_{21})	0.35
	Elastic Limit Stress (σ_{cr})	170 MPa
	Elastic Limit Strain (ϵ_{cr})	0.14%
	Ultimate Strength (σ_u)	420 MPa
	Ultimate Strain (ϵ_u)	0.78%
	Fiber Diameter (2a)	14.6 μm
	Fiber Vol. Fraction (c_f)	0.41

$^{\diamond}$ Simon and Bunsell (1984) † Harris *et al.*, 1992 ‡ Davies *et al.*, 1993
* Assumed based on hot-pressing data.

2.3 Experimental Procedure

All of the experiments with SiC/CAS were performed on an MTS (Material Test Systems Corporation, Minneapolis, Minnesota) tension-torsion machine with 15 kN axial capacity. The machine was controlled with an MTS 458.20 controller. Experiments were conducted in displacement control with a ramp function input by an external function generator. The "lower" strain rate experiments presented in this chapter were performed at crosshead displacement rates of 0.0075 mm/s. The "higher" rate experiments presented in Chapter 4 used crosshead displacement rates of 7.5 mm/s. Load and displacement was

output by the MTS controller and was recorded using 12 bit data acquisition. Details of the specimen and grip design are given in the next section. Then, in the subsequent sections, the use of various transducers is discussed.

2.3.1 Specimen Design/Grip Details

The importance of specimen and grip design when testing ceramic materials cannot be overstated. Due to the brittle nature of ceramics, poor specimen and/or grip design would lead to stress concentrations which would invalidate the experimental results. For the present work it was desired to design specimens and grips which were inexpensive, which did not require elaborate equipment, and which allowed for making various *in situ* measurements.

The first step required choosing a grip method. Various options were considered. A flexible grip system is one in which the grips do not transmit moments (*i.e.*, they are free to rotate). In such a system, the centers of rotation of the grips and the line of symmetry of the specimen must all lie on the same straight line throughout the deformation. Additionally, in order for the grips to align themselves under load, the grips must be a) stiff enough such that any rotation at one end of the specimen is equal to the rotation at the other and b) essentially friction free. Flexible grip systems are incapable of applying compressive forces. Rigid grip systems require that the axis of symmetry of the specimen be on a line parallel to the direction of motion of the grips. These grips are required to be sufficiently stiff such that the displacements are only in the axial direction. The commercially available self-aligning (flexible) grips generally work with a piston which is floating in hydraulic fluid. These grips are costly to either purchase directly or to develop in-house. In addition, the effectiveness of mechanical, self-aligning grips with bearings are limited by friction at even low loads. Such grips also have fixed centers of rotation which, as was previously mentioned, must both still lie on the axis of symmetry of the specimen. Therefore it was decided to proceed with a rigid grip system.

Rigid grip systems require manual concentric and angular alignment of one grip with respect to the other. Although adjustment fixtures are commercially available (*e.g.*, MTS Corporation, Minneapolis, Minnesota), it was found that for MTS servo-hydraulic machines, the position of the load cell can be adjusted concentrically. In addition, angular alignment can be achieved by using shims in conjunction with load cell positioning. Proper alignment is accomplished easily when the grip fixtures are cylinders. A tube (or box stock) whose inner diameter matches the outer diameter of the grip fixture is fitted over the cylindrical grip fixtures. The alignment is then performed so that the tube slides freely around both grips. Validation of this alignment technique will be discussed shortly.

Various options for specimen design were also considered. It was decided that pinned specimens would be too expensive to machine and would most likely fail due to the stress concentrations at the pins. More elaborately machined "dog-bone" specimens would also be prohibitively expensive to machine and would most likely sustain internal damage during the machining process. For these reasons, it was decided to proceed with tabbed strip specimens. Specimen machining consisted only of cutting specimens into strips with a diamond wafering blade. For all of the present experiments, three inch long and $^1/_4$ inch wide strips were cut from the $^1/_8$ inch thick plate.

To transfer load from the grip to the specimen, dovetail slots were machined in the cylindrical grip fixtures, and angularly matched tabs were glued to the specimens. A photograph of the side view of the cylindrical grip fixture and a ceramic composite specimen with its angled tabs is shown in Fig. 2.3.1a. A photograph of the grip and the specimen from the front is shown in Fig. 2.3.1b. In this front-view photograph, the wedges which keep the specimen centered within the grips are visible. The specimen tabs were angled by 10° in order to produce a normal force and thereby facilitate the transfer of load through the glue. Since the cylindrical grip fixtures are steel, for low stiction, brass was used for the angle-tabs. The tabs were glued with SpeedBonder 325 (Loctite Corp, Aurora, Illinois). Gluing the tabs on the specimens was done by hand. This led to asymmetries due to placement of the tabs

and varying glue layer thickness. Assuming the worst possible bending configuration, tab offsets of only 15μm would cause significant bending strains. Therefore, following gluing, a special tooling fixture was designed, and a 3 axis CNC milling machine was programmed to machine the specimen and its tabs to be perfectly symmetric.

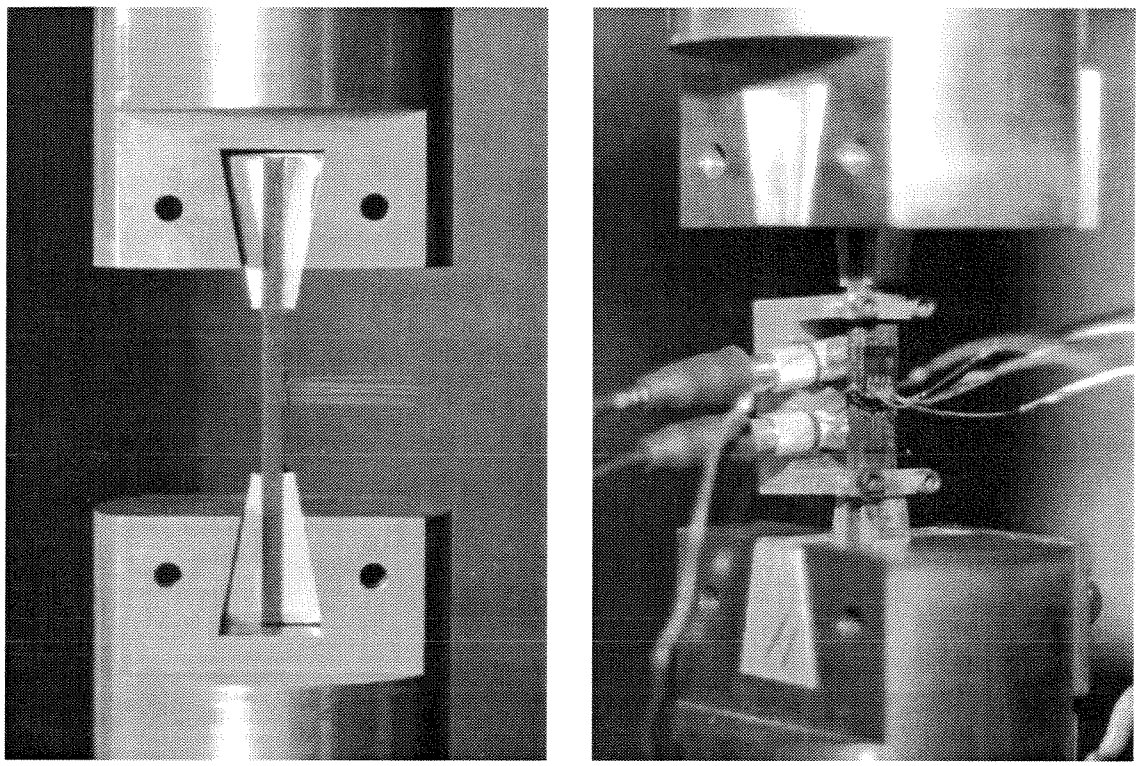

a) b)

FIG. 2.3.1 a) A photograph of the side-view of the quasi-static grip fixtures with a ceramic matrix composite specimen. b) A front-view photograph of the grip fixtures with a fully instrumented failed specimen and wedge spacers.

The alignment of the grip fixture was checked before each experiment. After the load cell was adjusted such that the alignment tube moved freely around it, the tube was removed and a brass dummy specimen was elastically deformed. This brass specimen was machined from a solid piece of brass with the same CNC program as that for the actual specimen. It was used because brass has a comparable modulus to the ceramic matrix composite. The brass specimen was instrumented with strain gauges on each of the 4 gauge section surfaces (see Section 2.3.2 for details regarding strain gauge sensing). The 4 strain gauge values

were checked with ASTM Standard E-1012 (1993) to verify that the normalized bending strain was less than 5%. This calculation is summarized in Appendix A. For the described setup, the worst normalized bending strains were calculated to be 1.3%.

As a further check of the alignment, Aluminum Nitride (AlN), a monolithic ceramic was tested. As with most monolithic ceramics, AlN fails at less than 0.1% strain, and misalignment during tension testing is revealed through grip-section failures. For the present experiments with AlN, failures were typically in the gauge section. From one such experiment, the stress-strain curve generated from two strain gauges on opposite sides of the specimen is shown in Fig. 2.3.2. These curves show that there is negligible bending from 0.005% strain to ultimate strain at 0.07%. As expected the curve is linear with a modulus of 350 GPa, and the ultimate strength is 250 MPa. The strain rate for this experiment was $10^{-6}s^{-1}$. The noise seen in the data is within the Wheatstone bridge circuitry. For all experimental results reported, macroscopic failure always occured within the gauge section (*vis-à-vis* Fig. 2.3.1b).

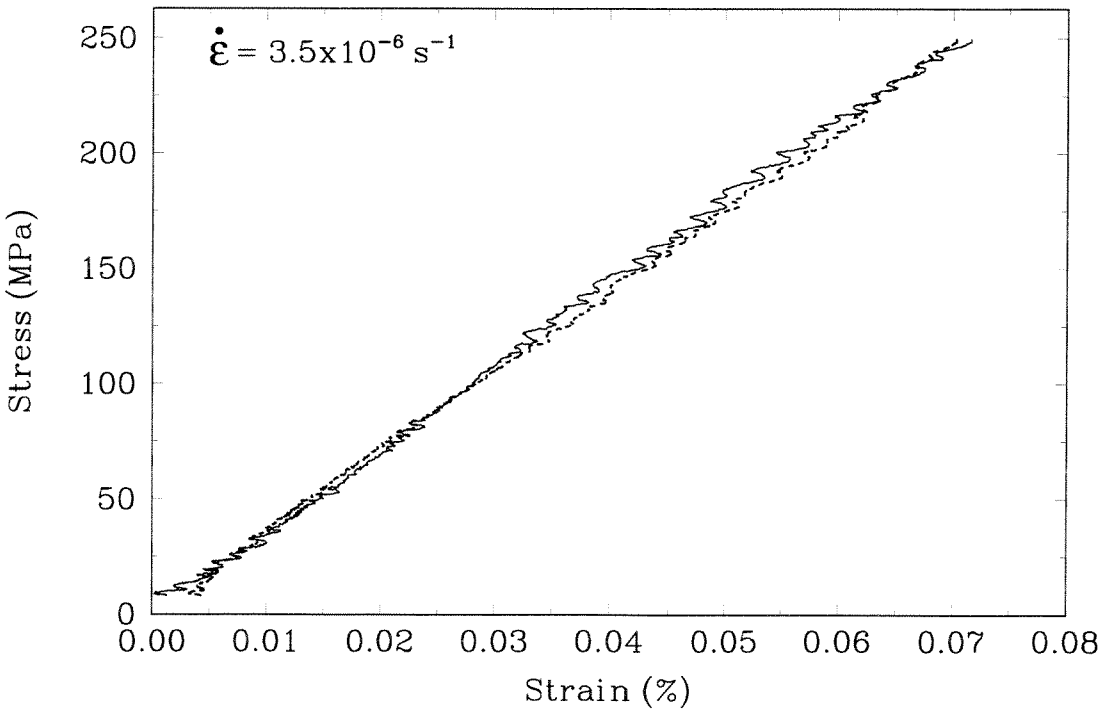

FIG. 2.3.2 The axial stress-strain curves for a monolithic Aluminum Nitride specimen with strain gauges on opposite sides of the specimen.

The primary advantage to this grip and specimen design and testing procedure is the ability to cost-effectively obtain valid experimental data for testing of ceramics and ceramic composites. By changing the thicknesses of the tabs and/or the spacer wedges is possible to accommodate different specimen geometries. It is also noteworthy that the specimens and grip fixtures are such that the gauge section surfaces are fully accessible for mounting various transducers. Experiments have been performed with multiple strain gauges and ultrasonic transducers or an acoustic emission (AE) transducer. The specimen shown in Fig. 2.3.1b has an ultrasonic shear wave and a normal wave transducer on the back face and a 0/90° strain gauge rosette on the front face of the specimen gauge section. The main disadvantages of this type of specimen are the reliance on the glue to transfer the force from the tab to the specimen and the limitations regarding testing in hostile environments.

2.3.2 Strain Sensing

Various different foil resistance strain gauges were used throughout the experiments. The different gauges were used either for convenience (*e.g.*, 0/90 strain gauge rosettes) or dimensional reasons. All gauges were from Measurements Group (Measurements Group, Inc., Raleigh, North Carolina), were 350 Ohms, and had a 1.5% maximum strain capability. Gauges with a grid size of 1 x 2 mm (031EC and 031DE) and gauges with 2 x 3 mm grid sizes (062AP and 062TT) were used primarily on the 3.25 mm sides and 6.5 mm faces of the specimens, respectively. To check for geometric effects, the smaller gauges were used on the 6.5 mm faces and the larger gauges were used on the 3.25 mm sides for two experiments. No differences were noted. All gauges were attached to specimens using Loctite Depend Adhesive and following the Measurements Group guidelines for gluing.

Measurement of the change in resistance with strain for the foil gauges was done using in-house constructed Wheatstone bridge circuitry. These bridges are standard equal-arm bridges and are documented in references such as Dally and Riley (1991). The Wheatstone bridges were powered with 10 Volts DC. This is approximately 3 times higher

than the recommended applied voltage for the gauges mentioned above. Nonetheless, it was observed that the high voltage did not produce thermal effects in the output, nor were the gauges degraded in any way. The advantage of the high bridge voltage is that the noise to signal ratio is much lower. The output signal from the Wheatstone bridges was recorded by 12 bit continuous data acquisition (Nicolet 440 or Nicolet 20x oscilloscopes, Nicolet Instrument Corporation, Madison, Wisconsin and Masscomp Model 5400, Masscomp, Westford, Massachusetts). For the Nicolet 20x and Masscomp systems, amplifiers/filters (8300 XWB Amplifier, Preston, Anaheim, California) were used to condition the signal.

2.3.3 Acoustic Emission

On some specimens acoustic emission (AE) was monitored. As explained by Eitzen and Wadley (1984), acoustic emission is the name given to transient mechanical waves which are spontaneously generated by abrupt, localized strain changes within a body. Dislocation motion and/or crack propagation are two mechanisms which can cause such localized strain changes. The acoustic emission causes surface motion of a body which can be measured by transducers. It is important to realize that different events within the material will cause different surface motion. One of the difficulties with acoustic emission is interpreting the data quantitatively. It is possible to detect and locate sources, however, it is not possible to determine event characteristics such as size and direction of propagation. For the current experiments, a $^1/_4$" diameter AE transducer (Micro-30, Physical Acoustics Corp., Princeton, New Jersey) was coupled to the 6.5 mm specimen face using a special holder and vacuum grease for the couplant. This transducer is tuned to resonate at approximately 150 kHZ.

Appendix B shows a schematic of the acoustic emission data acquisition setup. The main challenge with data acquisition was the need to sample at a high rate for the majority of the duration of a lower strain rate experiments (approximately 150s). The output from the acoustic emission transducer went first to a low noise pre-amplifier (Model SR560, Stanford

Research Systems, Sunnyvale, California) and then to an analog to digital (A-D) converter (DSP56ADC16, Motorola Semiconductor Products Sector, Austin, Texas) which was AC coupled and used in 8 bit mode. The A-D was part of a Motorola Digital Signal Processor (DSP560000ADS) which was directly connected to a 486-50 PC. The PC triggered the DSP to run a program which uniformly sampled the output of the A-D at 48 kHZ and wrote the data directly to the PC's expanded memory for 130s. The speed of sampling depended on the speed of the PC bus and the duration of the sampling depended on the amount of expanded memory in the PC. For timing purposes, when data acquisition began and ended, a signal was sent from the PC to an independent data acquisition channel. The impedance of the timing signal was lowered through an op-amp follower.

2.3.4 Ultrasonics

For several different experiments, *in situ* ultrasonics was performed. A 10 MHz ultrasonic longitudinal wave transducer and a 5 MHz ultrasonic shear wave transducer (#V-129, #V-157, Panametrics Inc., Waltham, Massachusetts) were coupled to either the 6.5 mm face or 3.25 mm side of the specimens. These piezoelectric transducers can produce and measure vibration at the transducer surface. The normal wave and shear wave transducer produce vibration perpendicular and parallel to the transducer surface, respectively. The shear wave transducer was oriented with polarization either perpendicular or parallel to the fiber direction. The ultrasonic transducers were used with a pulse-echo ultrasonic analyzer (Model 5052UA, Panametrics Inc., Waltham, Massachusetts). After being excited by a initial burst pulse, the transducer "listens" for echos which constitute reflections of the initial burst. As shown in Fig. 2.3.3, the analyzer output has both the initial burst pulse and subsequent echos. It is difficult to manually correlate the peaks in the burst pulse with the peaks in the reflections. However, as is seen in Fig. 2.3.3, the reflections are very self-similar, and hence the time between corresponding peaks is easily determined. Upon sustaining damage which is large with respect to the ultrasonic wave length and which is

"properly" oriented with respect to the ultrasonic wave particle motion directions, the wave speed decreases. Hence the drop in wave speed is related to the damage state of the material. In addition, since the wave speeds are related to the elastic constants of the material, the influence of the damage state on the elastic constants can also be determined.

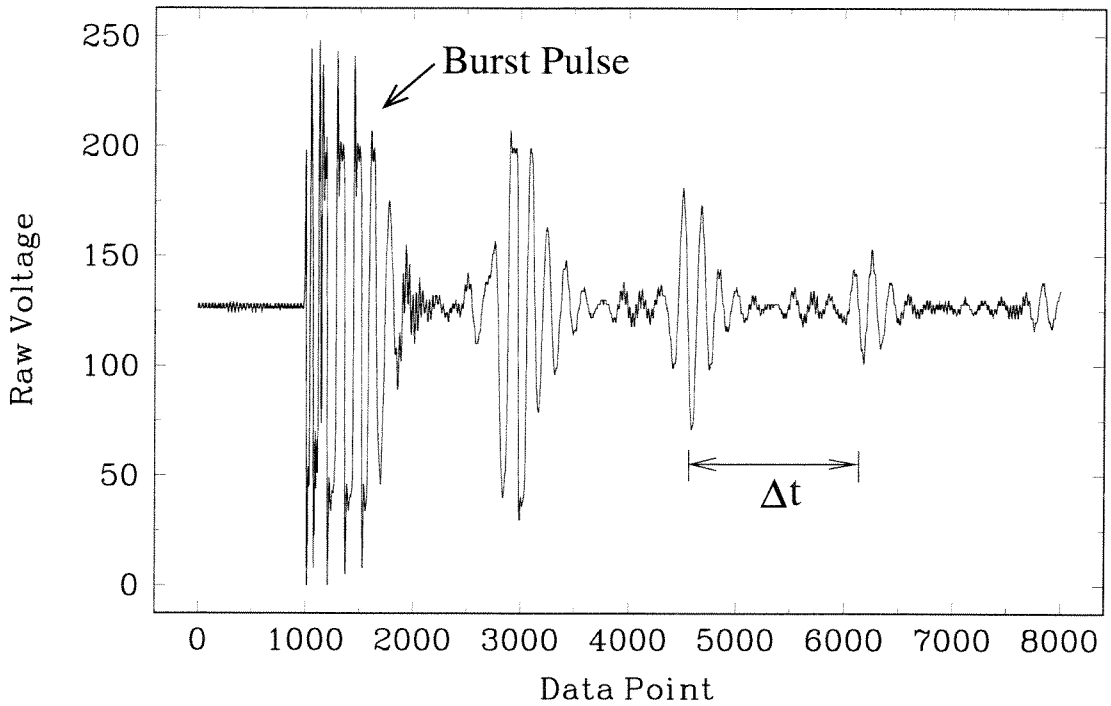

FIG. 2.3.3 The signal from the ultrasonic analyzer showing the initial burst pulse and three subsequent reflections of a shear wave.

In order to determine the wave speed at a given instant of time, it was necessary to capture the initial pulse and several echoes output by the ultrasonic analyzer. Since the normal wave speed and shear wave speeds for undamaged SiC/CAS (perpendicular to the fibers) are 7200 and 4200 m/s, respectively, and ultrasonic frequencies are in the megahertz regime, the signals needed to be sampled at a very high rate. Thus the signal from the analyzer was passed to an HP 54510A oscilloscope (Hewlett Packard, Palo Alto, California) sampling at 1 GHz. A schematic of the data acquisition setup is shown in Appendix C. The 486-50 PC was equipped with a GPIB board (Model NI-488.2, National Instruments, Austin, Texas) and was programmed to trigger the ultrasonic analyzer, to

acquire and store the data from the oscilloscope, to switch the relay, and then to repeat the process. Each digitized signal (waveform) consisted of 8000 eight bit data points. The time to acquire each waveform was limited by the oscilloscope buffering to approximately 1.5 seconds. After an experiment, there were a large number of files for which the time between wave bursts needed to be calculated. It was found that since the bursts remained self-similar, the time between bursts could be followed by using an autocorrelation program. The autocorrelation procedure is also able to identify time-of-travel using only the initial burst pulse and a single reflection. This is useful since for heavily damaged materials, attenuation of the waves can be quite severe, and it is possible that only one reflection will be clearly identifiable.

2.4 Experimental Results and Discussion

2.4.1 Stress-Strain Curves

Typical stress versus axial strain curves for lower strain rate ($\approx 10^{-4}s^{-1}$) experiments with SiC/CAS are shown in Fig. 2.4.1. The load was applied in the x_3 direction as defined in Fig. 2.4.1. The Young's modulus for this material is seen to be around 130 GPa. Following the initially linear behavior, there is a severe loss of stiffness which precedes another nearly linear region which has a very low slope. Next there is a stiffening of the material, and finally, a slight leveling off before ultimate failure. The tangent modulus of the stress versus axial strain curve showed that the curve is essentially tri-linear with two transition regions. Macroscopic failure was at an ultimate strength and strain of approximately 420 MPa and 0.8%, respectively. The curves presented in Fig. 2.4.1 are only typical. Other experimental curves often have slightly different shapes and ultimate strain values. For this reason it is assumed that the strain gauges are able to sense different degrees of damage and in particular matrix crack opening displacement.

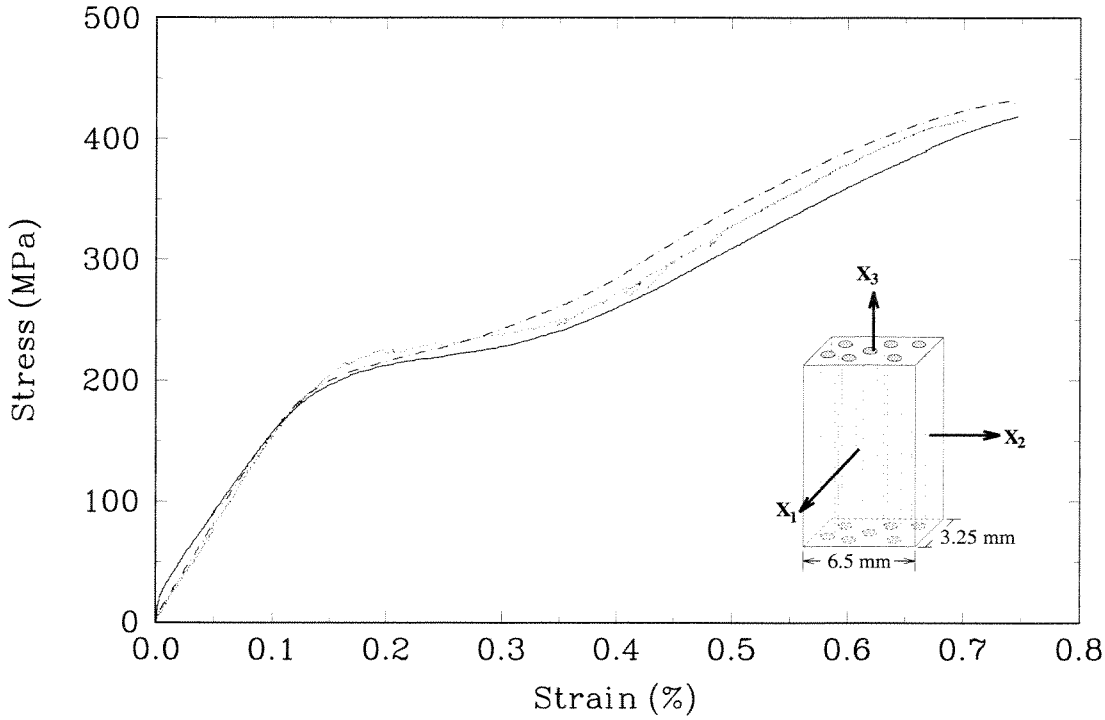

FIG. 2.4.1 Typical stress versus axial strain curves for SiC/CAS with load applied in the x_3 direction.

Several stress versus transverse strain curves for gauges on the 6.5 mm face and the 3.25 mm side are shown in Fig. 2.4.2. For the coordinate system shown, the transverse strain on the 3.25 mm face is ϵ_{11} and the transverse strain on the 6.5 mm face is ϵ_{22}. The transverse strains begin, as expected, by showing compressive deformation due to the Poisson effect. At a stress level of about 170 MPa, there is a reversal of deformation which represents expansion of the specimen in the transverse direction. Upon further loading, the transverse strains reverse again. If this material were perfectly transversely isotropic at all stages of deformation, ϵ_{11} and ϵ_{22} would be identical throughout the loading history. This is the first time that transverse strain measurements on the side of plates of SiC/CAS have been made. The differences between ϵ_{11} and ϵ_{22} are quite substantial and will be discussed in Section 2.4.5. Nevertheless, notice that the highest transverse strain was less than 0.25%, and for some measurements the maximum transverse strain was less than 0.05% strain. Post-test observations of the specimens showed that in all cases, the gauges remained fully

bonded to the specimens. In addition, neither the size of the gauge nor the dimension of the surface to which they were glued affected the strain measurements. As was the case with the axial strain measurements, the transverse strain measurements show that the strain gauges can sense different levels of damage. This is evident in the ϵ_{11}s presented in Fig. 2.4.2; for other experiments, ϵ_{22} showed significantly more variation, with, for some instances, the transverse expansion causing bulging beyond the original transverse dimension of the specimen.

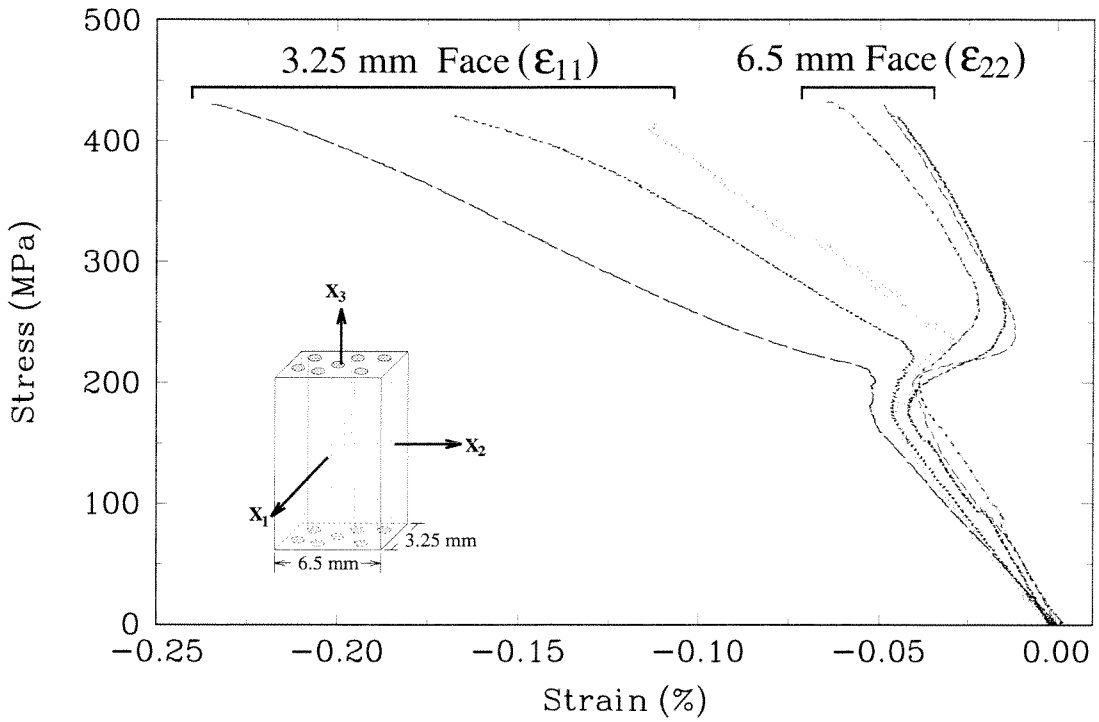

FIG. 2.4.2 Stress versus transverse strain curves for strain gauges on the 3.25 mm (ϵ_{11}) and 6.5 mm (ϵ_{22}) specimen faces.

Similar stress versus transverse strain curves have been presented by Harris *et al.* (1992), Nardone and Prewo (1988) and Sørensen (1993). However, for these authors, the second reversal in transverse strain consisted only of a transition to vertical (constant strain). This was not the case for the present experiments where, as is seen in Fig. 2.4.2, both ϵ_{11} and ϵ_{22} continue to measure further contraction after the second reversal. The main differences between the present experiments, and those of the above listed authors is

that the present experiments were performed at slightly lower crosshead displacement rates and the specimens were slightly smaller. It is unknown if specimen size effects transverse strain measurements. As will be shown in Chapter 4, higher strain rate experiments do have an incomplete second reversal of the transverse strain.

2.4.2 Micromechanisms of Deformation

Post test microscopy (optical and scanning electron) was performed on different specimen cross sections. The purpose of these investigations was to establish which deformation (damage) mechanisms had been active during the experiment.

The macroscopic fracture surface of the specimens was examined using a CamScan (Camscan USA, Mars, Pennsylvania) scanning electron microscope (SEM). Figure 2.4.3 is an SEM micrograph of a fracture surface taken at approximately 45° to the direction of loading (fiber direction). The surfaces of both the fibers and the matrix show brittle failure. Note that the macroscopic crack did not propagate straight, and that the fracture surface is quite wavy. Significant fiber pull-out is clearly visible in the form of both protruding fibers and empty holes. This implies that, at the very least, during the final stages of loading, fiber pull-out with frictional sliding was an important damage mechanism.

Figure 2.4.4, an optical micrograph of a specimen polished in the direction of the fibers, shows matrix cracks bridging the fibers. The average crack spacing is approximately 150 μm. Recall that the smallest strain gauge grid surface was 1 mm. This implies that there were approximately 6 cracks under each strain gauge. Results in Section 2.4.3 will suggest the stage during the test at which these matrix cracks were formed. Similar polishing of untested specimens showed no matrix cracking. However, the long, black voids were present in both the tested and the untested, polished specimens; these voids are presumably caused by the mechanical polishing process. Because of the damage introduced during polishing in this particular orientation, it is not possible to identify debonding of

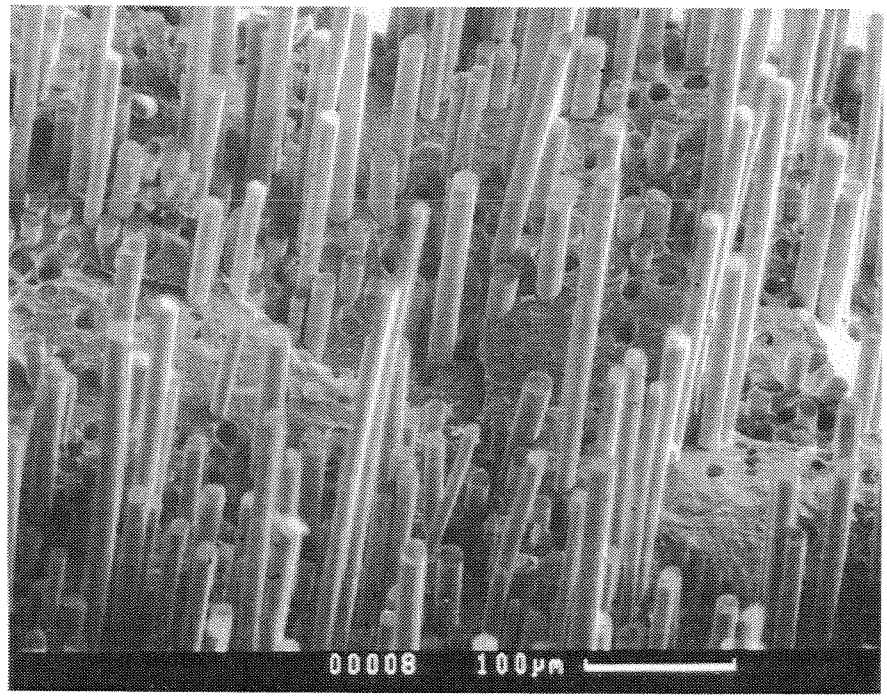

FIG. 2.4.3 An SEM micrograph of the macroscopic fracture surface ($\approx 45°$ to the direction of loading) showing fiber pull-out.

the fiber-matrix interface. However, in Section 2.4.4 ultrasonic results which identify the propagation of debonds *in situ* will be discussed.

Upon polishing untested specimen cross sections perpendicular to the fibers, it was observed that the SiC fiber polished at nearly the same rate as the CAS matrix and that the polished surface was completely smooth (see Fig. 2.4.5). However, for tested specimens, optical micrographs such as that shown in Fig. 2.4.6 had regions where the polished surface was not smooth. An SEM micrograph with one such region is shown in Fig. 2.4.7. It is seen that after testing, the composite is damaged in such a way that matrix material will break away when polishing perpendicular to the fibers. These sections are small relative to the whole polished section and they exist very nearly throughout the length of the specimen. Thus, the periodic cracks shown in Fig. 2.4.4 may be misleading in that there is possibly additional damage distributed between the periodic cracks. This indicates that the three dimensional nature of the damage may be important.

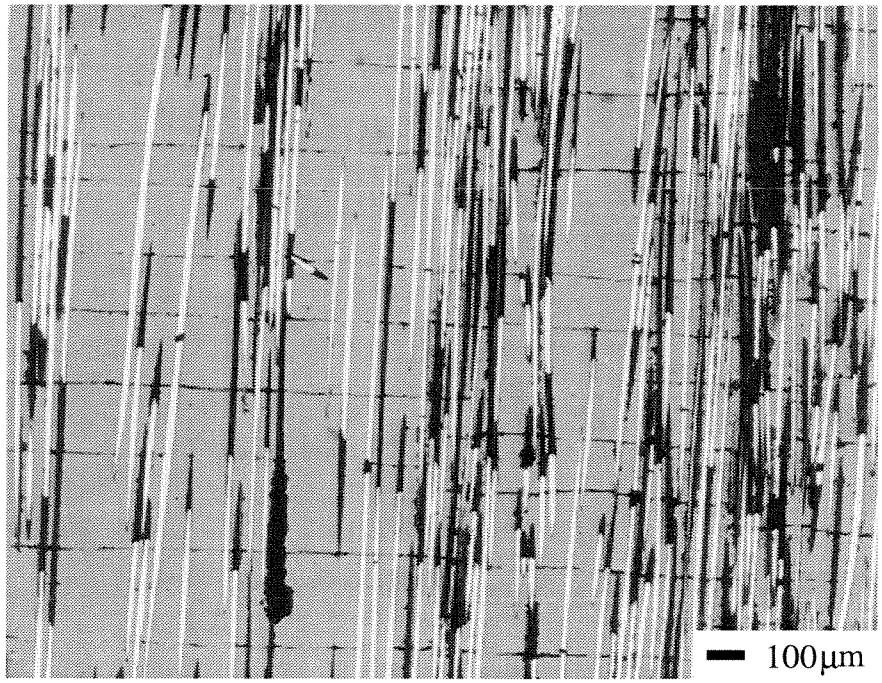

FIG. 2.4.4 An optical micrograph of fiber bridged matrix cracking as seen on an intact section of a specimen tested to failure.

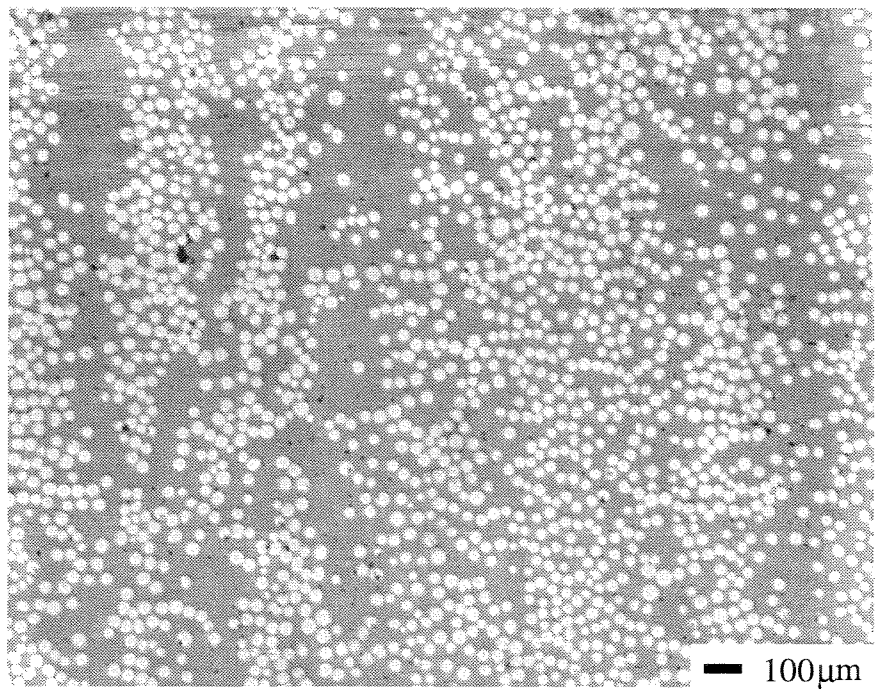

FIG. 2.4.5 An optical micrograph of an untested composites specimen polished perpendicular to the fibers and showing a smooth, polished surface.

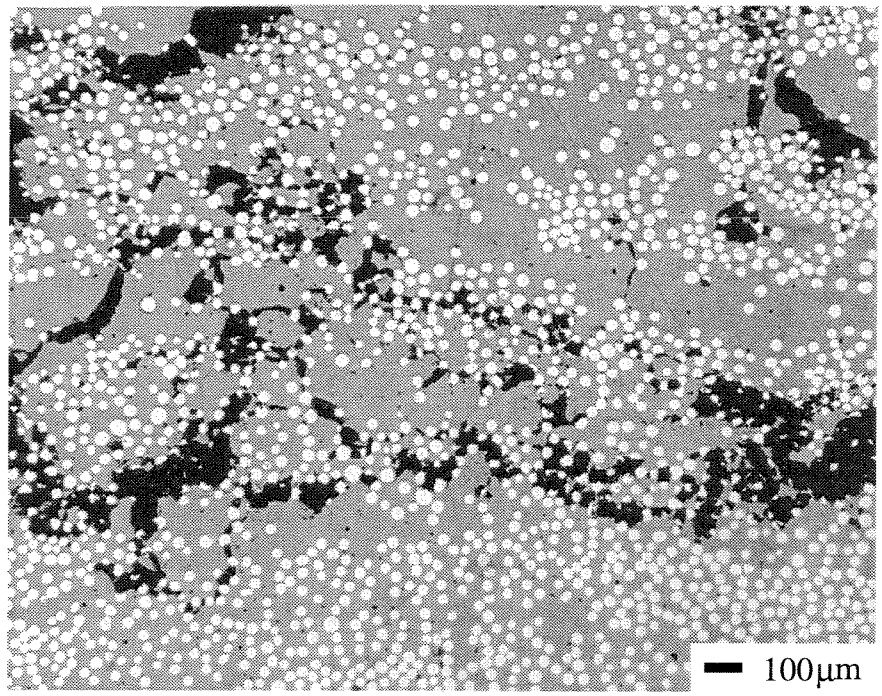

FIG. 2.4.6 An optical micrograph of a polished tested composite cross-section showing "canyons" where matrix material has broken away.

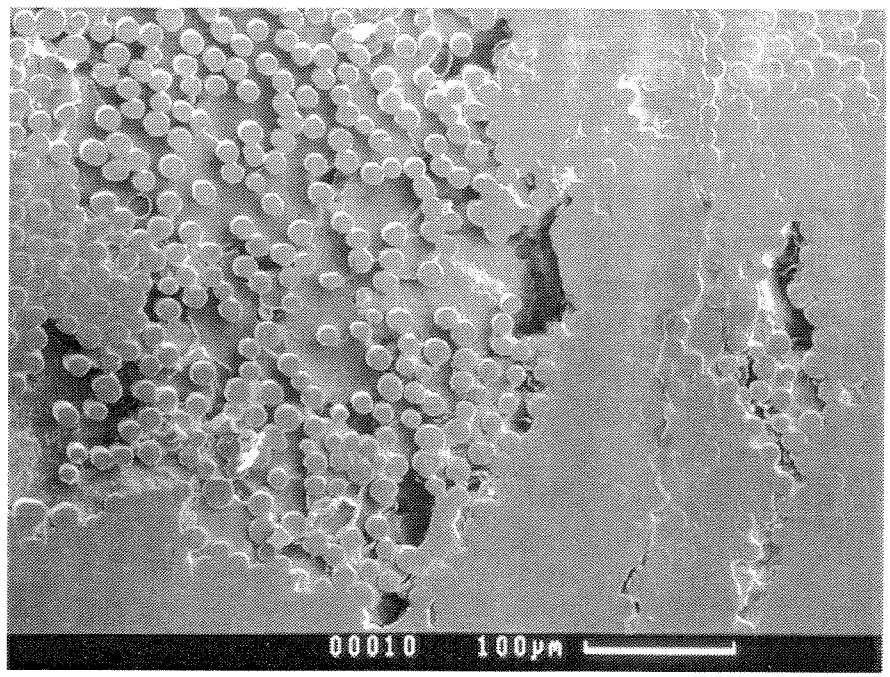

FIG. 2.4.7 An SEM micrograph of a polished, tested composite cross-section which shows more detail of a region where the matrix has broken away.

2.4.3 Acoustic Emission

The results for *in situ* acoustic emission (AE) measurements are shown in Fig. 2.4.8. Along with the axial stress versus strain curve, acoustic emission events (represented in terms of "counts") are plotted. For the current experiments, a "count" is defined as an event that is within a given frequency range and which exceeds an arbitrarily chosen threshold level. The reason for bandpassing only certain frequencies is to separate various sources of noise. In particular, it is essential that machine noise and vibration are removed from the signal. After digitally filtering and thresholding the data, the distribution of counts plotted in Fig. 2.4.8 was determined. The threshold value did not qualitatively effect the results. Other than a single peak the linear region is relatively quiet until about 100 MPa. The next region has a distribution of events over approximately 0.2% strain. This distribution has a nearly Gaussian shape centered around the narrow region in which the stress-strain curve becomes severely non-linear. The recorded AE events originated from matrix cracking; thus, these experimental results establish the zone in which the matrix cracking damage mechanism was active. Following this region of active acoustic emission, there is little activity until very near ultimate failure. It is likely that the events associated with macroscopic failure (fiber failure and macrocrack propagation) will cover a broad frequency spectrum and therefore will be recorded by the AE transducer.

2.4.4 Ultrasonics

The results for *in situ* ultrasonic wave speed measurements are shown in Fig. 2.4.9 along with an axial stress-strain curve. The ultrasonic results are presented as wave speeds normalized by the initial wave speeds (7200 and 4200 m/s for normal and shear velocities, respectively). It is seen that the wave speed is initially nearly constant and at approximately 0.2% strain, the speed drops quickly. At later stages in the test ($\approx$ 0.4%) the speed levels off slightly. For this particular experiment, a shear wave and normal wave transducer were coupled to the 6.5 mm specimen surface. The direction of wave propagation (k) and the

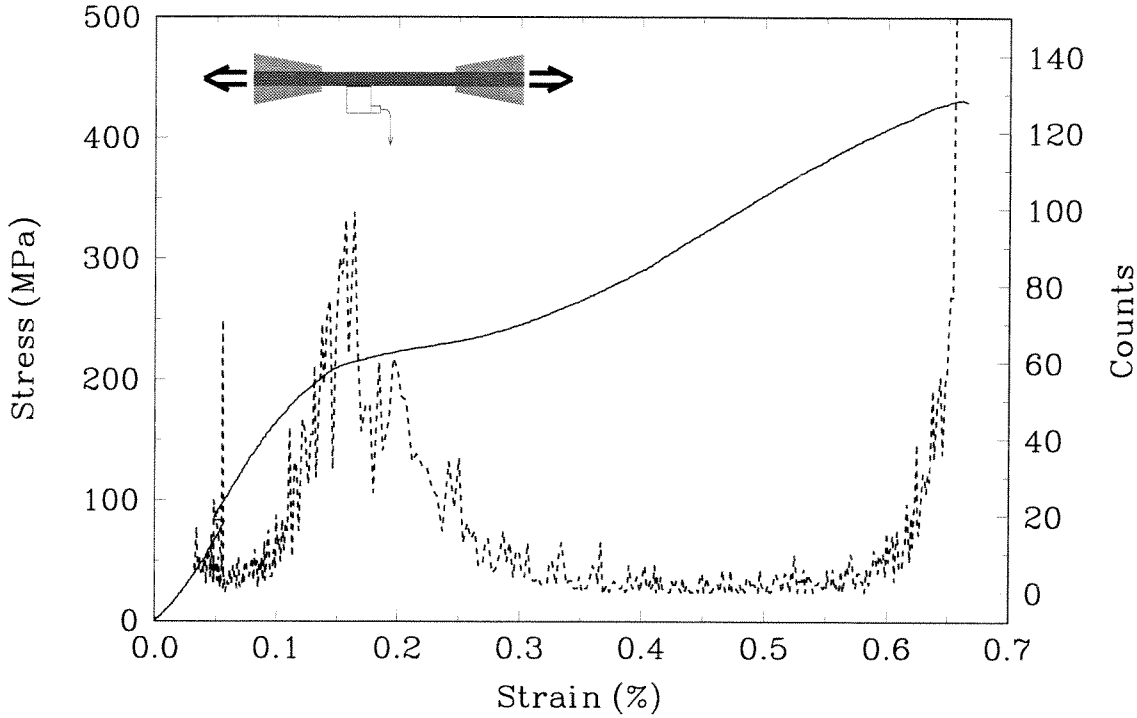

FIG. 2.4.8 Acoustic emission counts plotted along with the corresponding stress versus axial strain curve.

direction of particle motion (p) for each transducer is indicated schematically in Fig. 2.4.9. These schematics represent the 1-2 plane of the material where the fiber direction is parallel to the '3' direction. The decrease in wave speed is primarily due to the increase in transit time through damaged material. Depending on whether cracks are opening or sliding, the delay will be introduced in either the normal or shear waves, respectively. Based on the geometry of the cracking and the particle motion produced by the two ultrasonic transducers, it is realized that both longitudinal and shear wave speeds decrease primarily as a result of debonding of the fiber-matrix interface. This is also true when the shear wave transducer is polarized parallel to the fibers; however, for the two orientations of the shear wave transducer, the material symmetry and damage sensing differences will produce different results. These differences for polarizations normal to and parallel to the fibers are illustrated in Fig. 2.4.10. It was observed that after the specimen failed and the region under the ultrasonic transducers was unloaded, the wave speeds increased. Thus unloading

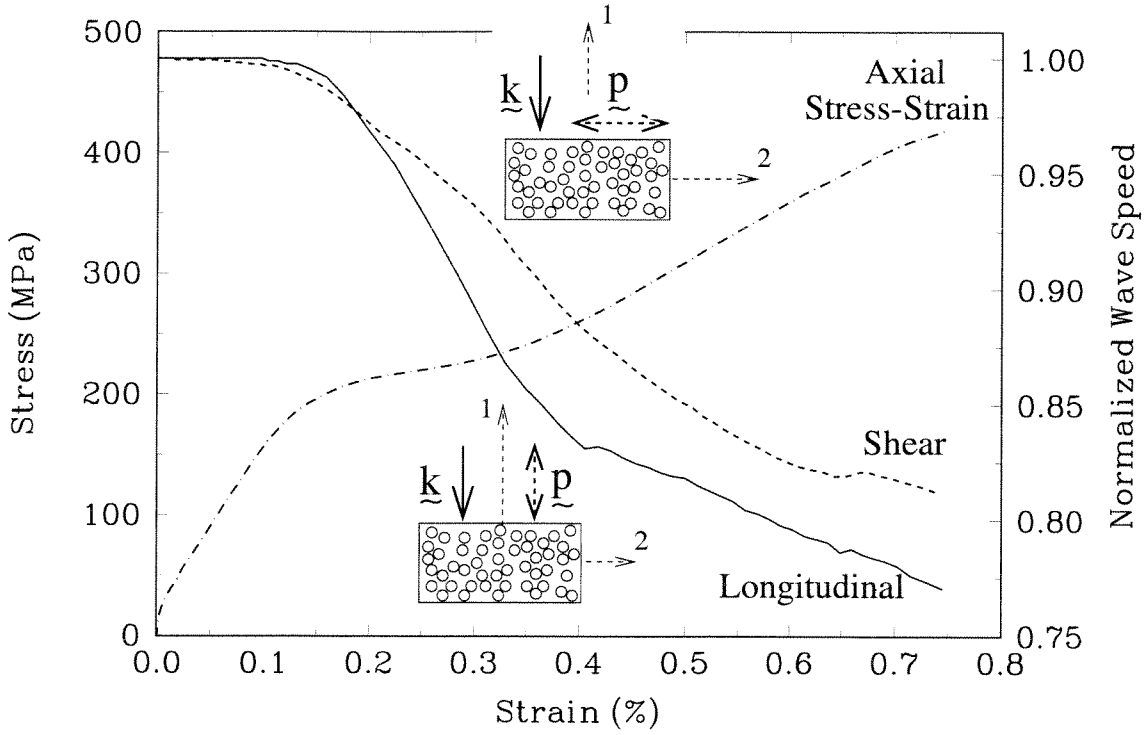

FIG. 2.4.9 The normalized ultrasonic longitudinal and shear wave (1-2 polarized) speeds versus stress.

has the effect of masking some of the internal damage. This has important implications for interpretation of post-test results.

The ultrasonic data can also be used to investigate the variation of the elastic constants for the given loading history. The relationship between the ultrasonic wave speed and the elastic constants are obtained through classical elastodynamics. It is important to realize that the constants are universal only in the elastic region. After the elastic region, they are not constant, but, rather, are functions of the given state of damage. If the same damage evolved for a given loading, then local perturbations at the proper stress level, would yield the same material constants. It is, however, likely that different loading configurations and histories (including strain rate) will induce different damage. Nevertheless, determination of the elastic "constants" is instructive in that it provides information on the current state of damage.

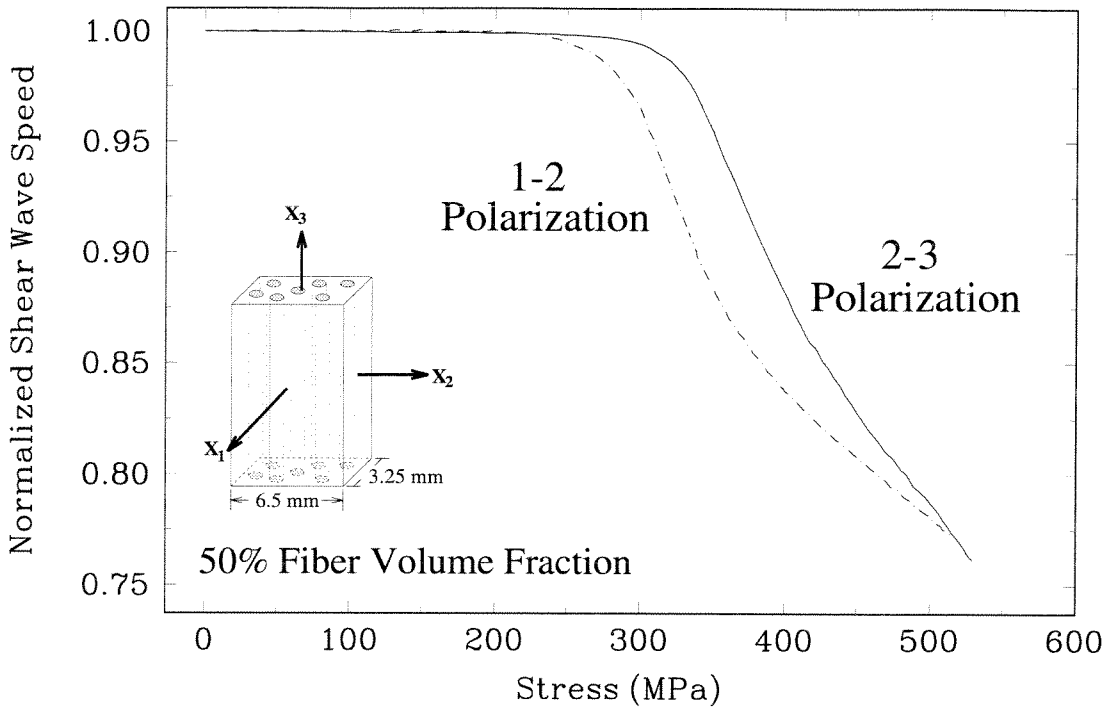

FIG. 2.4.10 Comparison of the change in normalized shear wave speed for wave polarized normal to (1-2) and parallel to (2-3) the fibers.

For the transducer orientations shown in Fig. 2.4.9, the longitudinal wave speed (c_l) and shear wave speed (c_s) are related to the material constants as follows:

$$c_l^2 = \frac{C_{11}}{\rho} \qquad \text{and} \qquad c_s^2 = \frac{C_{66}}{\rho}, \tag{2.4.1}$$

where ρ is the mass density of the material. For an isotropic, homogeneous, linearly elastic material, $C_{11} = \lambda + 2\mu$ and $C_{66} = \mu$, where λ and μ are the Lamé constants. If the ultrasonic waves were "bar" waves C_{11} would be assumed equal to E, the Young's modulus, and the wave speed would be $c_b = \sqrt{E/\rho}$. For an isotropic material with Poisson's ratio of 0.3, the one dimensional c_b is 74.3% of the three dimensional c_l. For anisotropic materials, the expressions for C_{ij} become quite complicated functions. For the current unidirectional composites, as is typical in the literature, it will be assumed that transverse isotropy holds. For the coordinate system defined in Fig. 2.4.1 with fibers in the x_3 direction, the 1-2 plane is the plane of isotropy. For the transducer orientation given in Fig. 2.4.9, and for transversely

isotropic material symmetries, the two relevant components of the moduli tensor are:

$$C_{11} = \frac{\left(-E_3 + \nu_{31}^2 E_1\right) E_1}{-E_3 + 2\,\nu_{31}^2 E_1 + \nu_{12}^2 E_3 + 2\,\nu_{12}\,\nu_{31}^2 E_1}$$

and (2.4.2)

$$C_{66} = \frac{1}{2}\frac{E_1}{(1+\nu_{12})}.$$

Solving Eq. 2.4.2 and Eq. 2.4.1 for the in-plane modulus (E_1) and the minor Poisson's ratio (ν_{12}) yields the following equations:

$$E_1 = \frac{4\,c_s^2 \rho E_3\,\left(c_l^2 - c_s^2\right)}{4\,\rho c_l^2 \nu_{31}^2 c_s^2 - 4\,\rho \nu_{31}^2 c_s^4 + c_l^2 E_3} \tag{2.4.3}$$

and

$$\nu_{12} = -\frac{4\,\rho c_l^2 {\nu_{31}}^2 c_s^2 - 4\,\rho \nu_{31}^2 c_s^4 - c_l^2 E_3 + 2\,E_3\,c_s^2}{4\,\rho c_l^2 \nu_{31}^2 c_s^2 - 4\,\rho \nu_{31}^2 c_s^4 + c_l^2 E_3}. \tag{2.4.4}$$

The variables ν_{31} and E_3 in the above equations still need to be determined. The major Poisson's ratio ($\nu_{31} = -\epsilon_{11}/\epsilon_{33}$) is known from the axial and transverse strain measurements. Note that since the major Poisson's ratio is calculated from strain gauge data, it is a function of the damage history; this is further discussed in Section 2.4.5. Determining the changing axial modulus (E_3) required another experiment. Under the same loading configuration, a SiC/CAS specimen was periodically unloaded and then reloaded every 33 MPa. The magnitude of each unloading was approximately 15 MPa. The axial stress-strain response of the material for this experiment is shown in Fig. 2.4.11. Least squares fitting of the slopes of both the unloading and reloading trajectories was performed and the resulting moduli are plotted versus stress in Fig. 2.4.12. This plot shows that both the unloading and reloading moduli are decreasing with increasing load, and that the reloading modulus is less than the unloading modulus. In addition, the data shows that the modulus is slowly decreasing until 170 MPa, and then it drops off rapidly. The fact that the reloading modulus is less than the unloading modulus is consistent with the opening and closing of matrix cracks. Despite the multiple unloading and reloadings, it is noted that the stress-strain curve for the unloading-reloading experiments were quantitatively similar to monotonically loaded specimens.

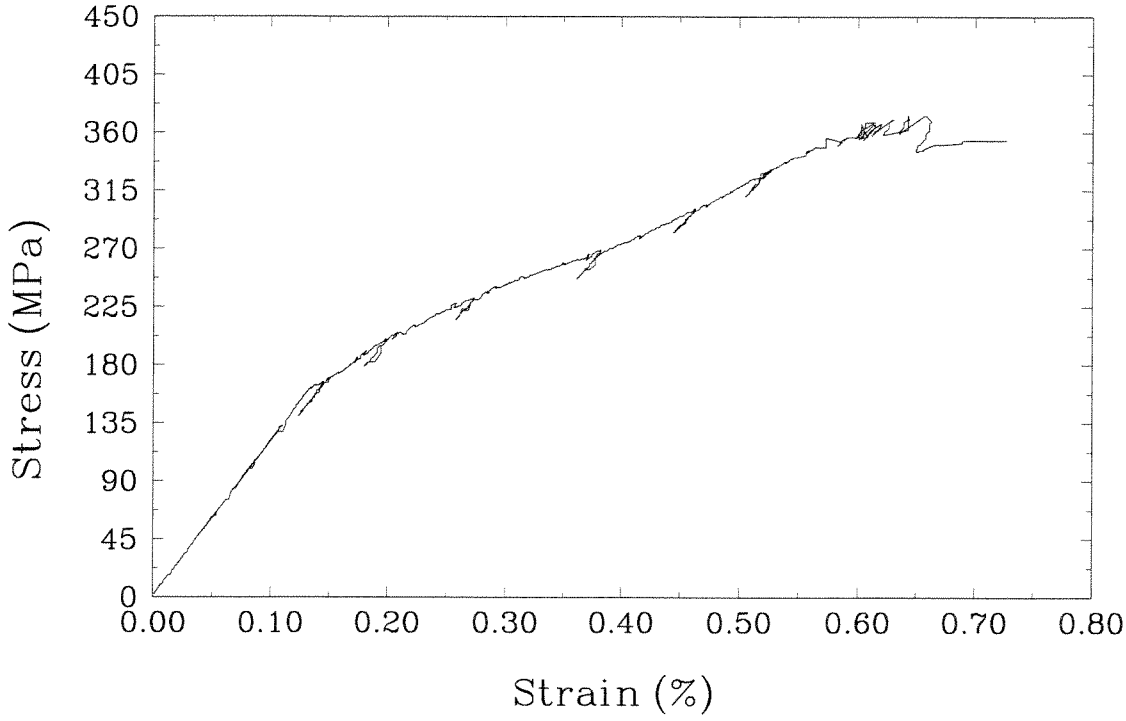

FIG. 2.4.11 The axial stress-strain response with periodic unloading and reloading of the specimen.

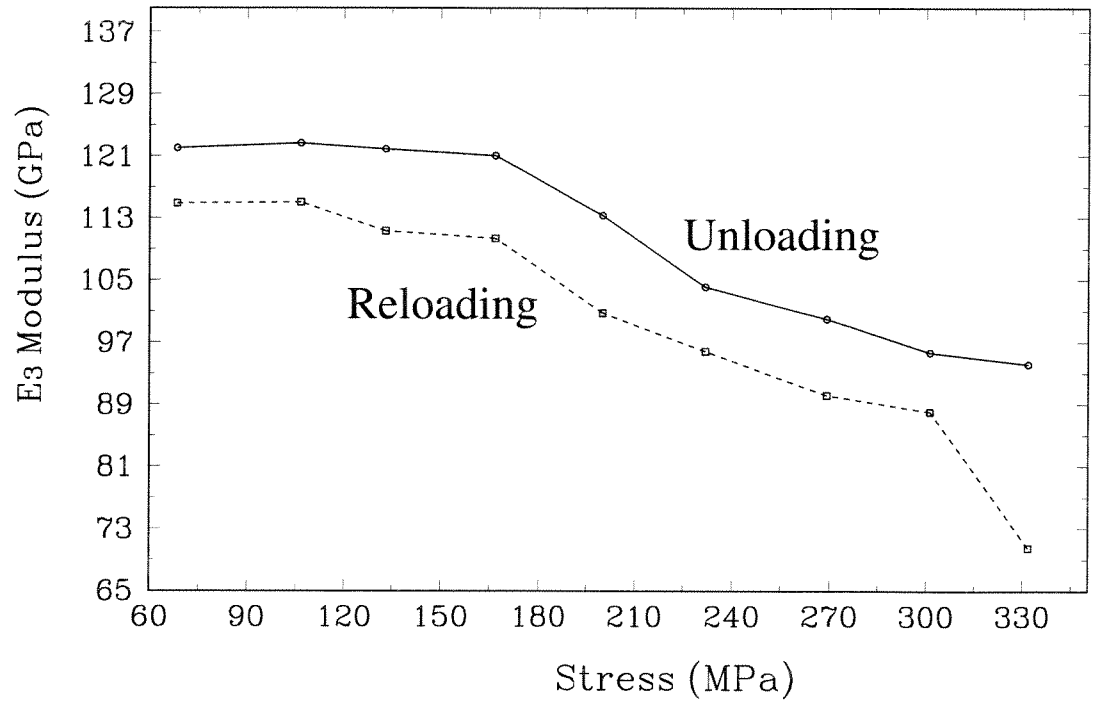

FIG. 2.4.12 The change in axial modulus computed from the results of a periodic unloading-reloading experiment.

The material constants resulting from the calculations discussed above are plotted versus stress in Fig. 2.4.13. Notice that the E_3 modulus begins to degrade before the E_1 modulus does. As will be discussed in Section 2.5.2, this has implications for the sequence of damage progression. It is also noted that the minor Poisson's ratio, ν_{12} is relatively constant throughout the loading history. The magnitude of this constant is also quite high. Note also, that the technique for calculating ν_{12} does not take into account the range of applicability of this constant. Since ν_{12} is the negative of the ratio of ϵ_{22} to ϵ_{11} for loading in the '1' direction (or *vice versa*, since transverse isotropy is assumed), the material will fail well before the *axial* ultimate strain is reached. At later stages in the loading history, when the material is heavily damaged, the calculation of ν_{12} becomes inaccurate because the strain gauges sense different levels of damage. Implications regarding damage induced anisotropy will be discussed in the next section.

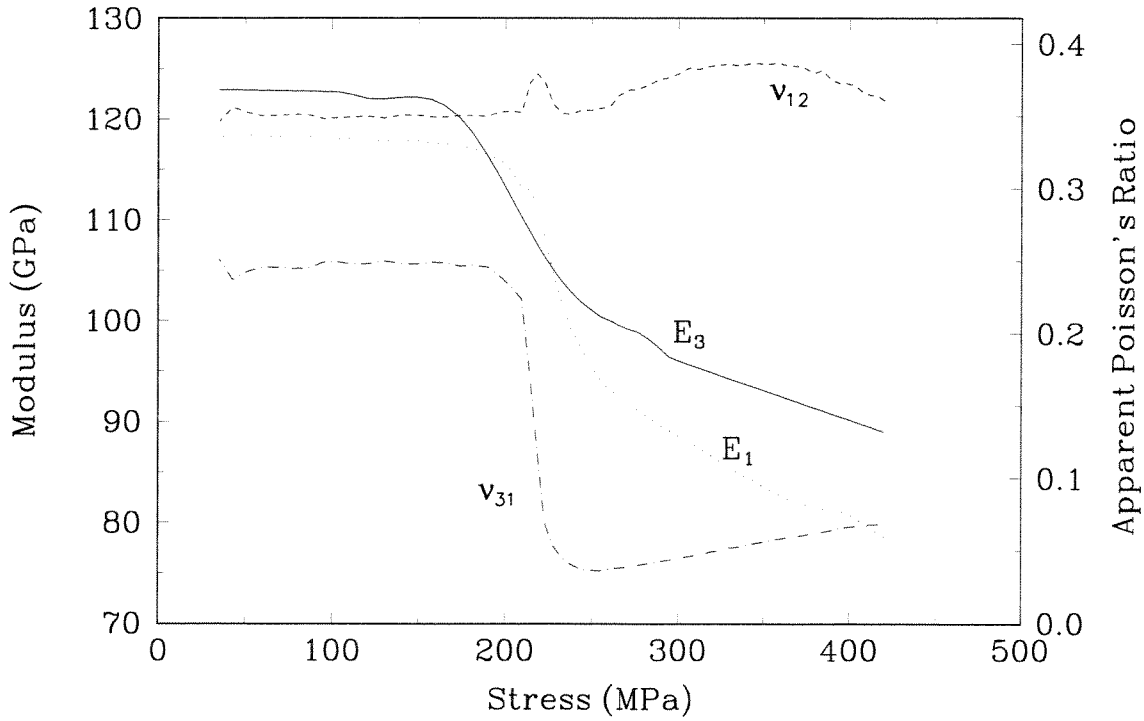

FIG. 2.4.13 Four material constants computed from strain gauge and ultrasonic wave speed data (defined according to the coordinate system in Fig. 2.4.1).

2.4.5 Damage Induced Anisotropy

Since unidirectional fibrous materials typically have two mutually orthogonal planes of symmetry and one plane of isotropy, they are called transversely isotropic and can be fully characterized by 5 elastic constants. The experimental data in Section 2.4.1 indicates that the unidirectional SiC/CAS composite is *not* transversely isotropic. In this section the source, implications and degree of the non-transverse isotropy are discussed.

It has been experimentally observed that the unidirectional SiC/CAS composite is slightly orthotropic. This has been realized through the ϵ_{11} and ϵ_{22} strains. It should be noted that since the measured strains are very small, small differences between ϵ_{11} and ϵ_{22} will appear to be quite significant. Since strain gauges were mounted on all four sides of specimens, it was verified that this orthotropicity is not an artifact of bending. Although there are small differences in the initial slope of the transverse stress-strain curve for the '1' and '2' directions, the more significant orthotropic character of the material appears primarily after the onset of damage (non-linearity in the stress-strain response). For this reason, it will be called "damaged induce anisotropy." In particular, since it is the transverse strain measurements which show directional dependence, it is the "transverse damage" which produces anisotropy. This is not surprising since there is no reason to expect that debonds would completely debond the fibers along their entire circumference. In addition, inspection of Figures 2.4.5 and 2.4.6 clearly shows a layered microstructure. If the whole specimen cross-section were shown, there would be 18 layers, corresponding to 18 rolled fiber tows. The microstructure most likely precludes the formation of randomly oriented debonds. The matrix damage seen in Fig. 2.4.6 shows that there is preference for damage to remain in the matrix-rich regions of the layers. A final possible reason for the observed transverse damage induced anisotropy is the fact that the material is hot-pressed perpendicular to the layers. This could lead to directional residual stress and/or preferential paths for crack propagation.

For material symmetry change from transverse isotropy to orthotropy, the number of material constants changes from 5 to 9. This has important implications for the computation of material constants from the ultrasonics results. In particular, the stiffness components, C_{11}, C_{22} and C_{33}, are complicated functions of the three Young's moduli and the three Poisson's ratios. In addition, unlike for transverse isotropy, the other diagonal stiffness components are only related to the shear moduli and not a combination of the other stiffness components. Thus from experiments using shear transducers on two different surfaces with polarization both parallel and perpendicular to the fibers, we can determine the shear moduli, μ_{12}, μ_{13}, and μ_{23}. The requirement that C_{ij} is symmetric implies that $\nu_{ij}/E_i = \nu_{ji}/E_j$, and therefore using strain gauges, ν_{13}, ν_{31}, ν_{23} and ν_{32} can all be determined. The change in E_3 is known from loading/unloading experiments. From ultrasonics experiments using the normal wave transducer on the '1' and '2' surfaces will give two relationships between C_{11} and C_{22} and the longitudinal wave speeds. Unfortunately, after this process we are left with two equations and three unknowns (E_1, E_2, and ν_{12}). Thus, the lose of transverse isotropy implies that it is necessary to independently calculate either one of the in-plane moduli or the minor Poisson's ratio. Experiments in the off-fiber-axis direction are one viable method of calculating these variables. However, this would limit the range of the constants, since for an off-fiber-axis configuration, the specimen would fail at very low stress and strain. Thus it would not be possible to comment on the evolution of the material constants throughout the loading history.

For the results presented with the assumption of transverse isotropy, valuable information was gained regarding the change of the material constants with damage. It is left to evaluate the degree to which the results are affected by the assumed material symmetry conditions. This was investigated by plotting the changing wave speeds for different wave propagation directions. In Fig. 2.4.14 and Fig. 2.4.15 the normalized wave speeds (in the '1' and '2' directions) are plotted versus stress for the shear and normal waves, respectively. Since these wave speeds are normalized, the information about initial anisotropy is lost on

the plots. However, the initial wave speeds were measured, and the difference in initial wave speeds was less than 1% and 7% for the normal and shear waves, respectively. The effect of damage on the change in wave speed is related to the shape of the curves in Fig. 2.4.14 and Fig. 2.4.15. Thus it is seen that as far as the ultrasonic results are concerned, since the shapes of these curves are self-similar, the dependence of damage evolution on direction is not significant.

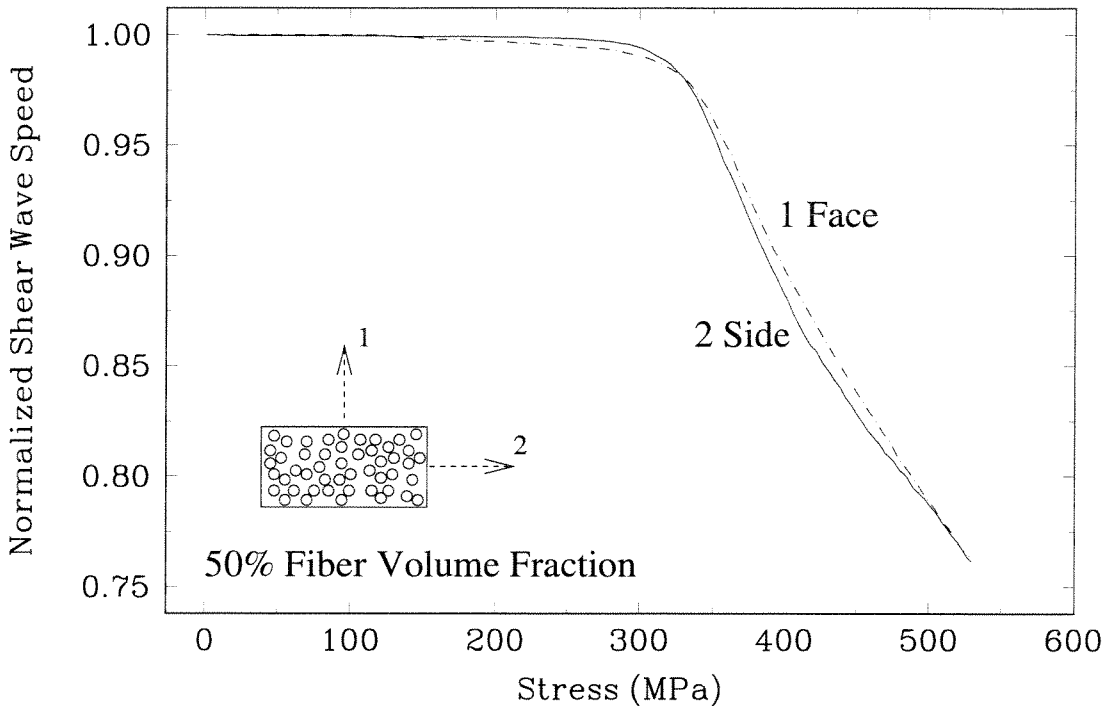

FIG. 2.4.14 Comparison of the change in normalized shear wave speed versus stress for wave propagation in the '1' and '2' directions.

2.5 "Zones" of Deformation

In Fig. 2.5.1 the scale of the transverse strain is changed and it is plotted along with the axial strain. By comparing the fundamental changes in slopes of these two curves, and by postulating that these changes are due to the onset of different deformation mechanisms, five zones of deformation are identified. The first zone (I) is a nearly linear region which lasts until approximately 170 MPa. The second zone (II) begins with the onset of severe

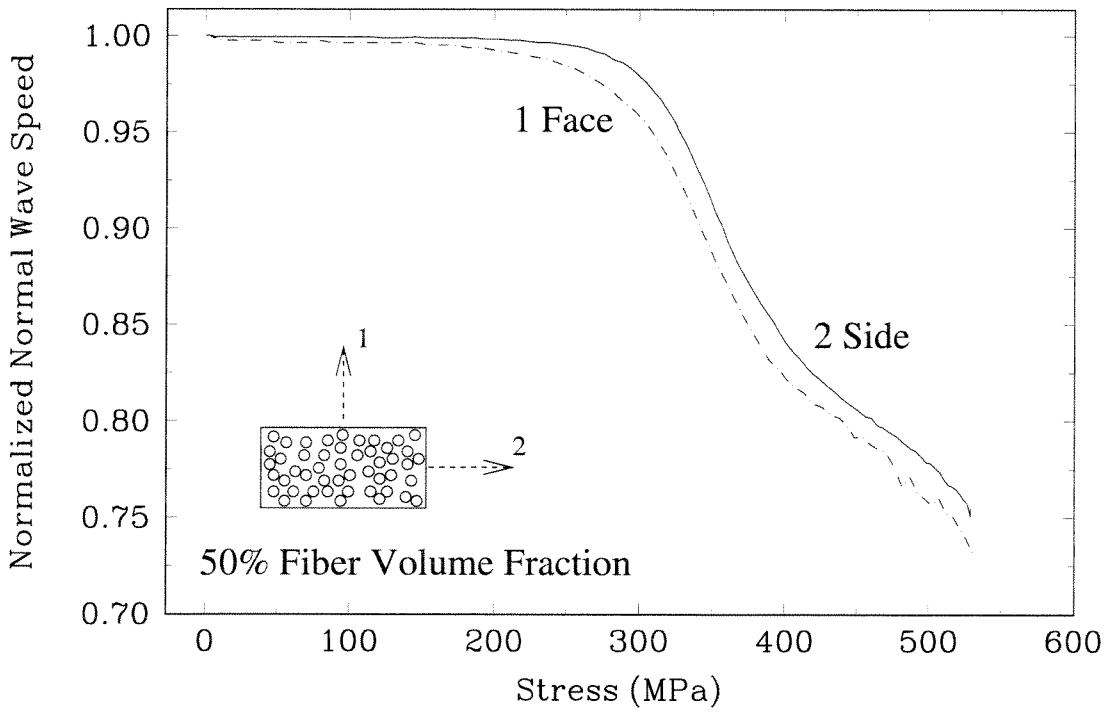

FIG. 2.4.15 Comparison of the change in normalized normal wave speed versus stress for wave propagation in the '1' and '2' directions.

non-linearity. A third zone (III) with a much lower slope begins at approximately 210 MPa. The fourth zone (IV) begins at 250 MPa and has a much greater slope than zone III. Finally, there is a fifth zone (V) from 350 MPa until the ultimate strength is reached.

2.5.1 Existence

The various experiments along with their respective measurements have been performed in order to both identify the important damage mechanisms and to establish the sequence and extent of their occurrence throughout a monotonic loading history. The post-test observations in the form of optical and scanning microscopy were done to complement these experiments. The post-test micrographs in Fig. 2.4.3 and Fig. 2.4.4 show the existence of the following damage mechanisms: matrix cracking, fiber bridging and fiber pull-out and sliding. During a loading history the extent to which any given damage mechanism contributes to the toughness varies. However, by concentrating on fundamental mechanics it is possible to postulate the qualitative sequence and extent of each mechanism. In

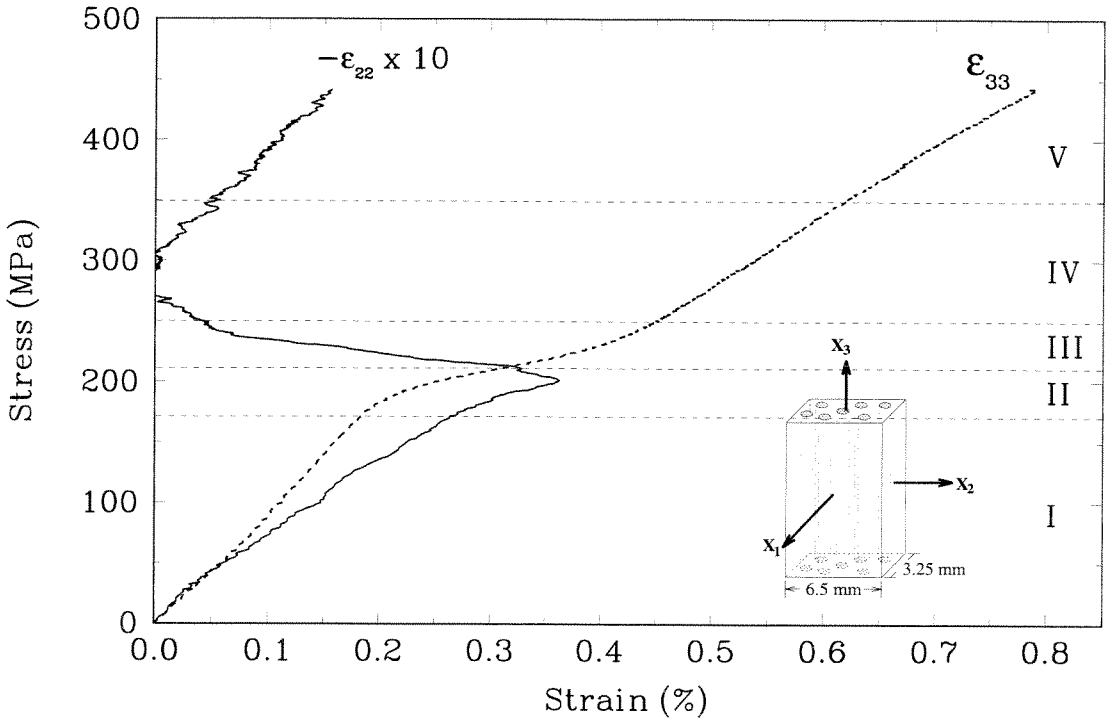

FIG. 2.5.1 Stress versus axial strain and transverse strain (with a 10× scale change) divided into five zones of deformation.

what follows, in each of five postulated "zones," the experimentally observed deformations (characterized by strain, acoustic emission and ultrasonics measurements) are explained based on load redistribution and the dominant damage mechanisms.

As can be seen from Fig. 2.5.1, the zones correspond to regions in which the stress-strain curves exhibit new trends. Although the zones appear to simply be the piecewise linear regions of the stress-strain curve, this is not to imply that the actuation of each damage mechanism yields a linear response. Rather, the zones are postulated based on comparison of the axial and transverse stress-strain curves. Despite the empiricism involved in defining the zones, the radical changes in strain direction of the transverse stress-strain curve indicate a fundamental change in damage mechanisms. Although in each zone several mechanism may be concurrently active, it will be shown in the following discussion that the deformation behavior can be described under the assumption that each zone is dominated by a single damage mechanism.

2.5.2 Sequence and Extent

The first zone (I) is classified as the "macro-elastic" zone. In this zone, the load is carried by both the fibers and the matrix. It is assumed that there is strain compatibility in the fiber (loading) direction. By definition, elastic deformation is that which is completely recovered during unloading. *Macroscopically*, this was observed in Zone I during the unloading-reloading experiment. The unloading and reloading slopes are represented by the first three points in Fig. 2.4.12. It is seen that the slopes in this stress range are nearly identical. Outside of a single isolated spike, the acoustic emission data in Fig. 2.4.8 is relatively free of cracking events. It is believed that the isolated spike is the result of grip noise which covered a range of frequencies and could not be filtered out. Other authors have found crack initiation for SiC/CAS at around 100 MPa (Beyerle *et al.*, 1992; Harris *et al.*, 1992; Kim and Pagano, 1991). From this information it is concluded that although cracks may form in Zone I, these cracks are too small to appreciably affect the *macroscopic* stress-strain behavior. In addition, the small cracks are stable and do not propagate to any significant degree. Pagano and co-workers at the Wright-Patterson AFB (Pagano, 1992) and Barsoum *et al.* (1991) have also shown that matrix crack initiation within Zone I is an isolated event.

At the onset of Zone II, the matrix and fibers are still equally strained. However, the matrix is very close to its failure strain of approximately 0.15%. Thus, at around 170 MPa, significant matrix cracking begins and the stress-strain curve exhibits severe non-linearity. Further evidence of matrix cracking is the unloading/reloading moduli of Fig. 2.4.12. The drop in moduli corresponds to the onset of Zone II, and the fact that the reloading moduli are less than the unloading moduli is consistent with the opening and closing of microcracks. In previous studies (Mah *et al.*, 1985; Marshall and Evans, 1985) of glass-ceramic composites (lithium aluminosilicate, LAS), matrix cracking was postulated to be a sudden event. In the present study, as well in other recent experiments with SiC/CAS (Kim and Pagano,

1991; Beyerle *et al.*, 1992), matrix cracking has been found to be a gradual process. The stress-strain curve throughout this process is smooth and monotonically increasing.

Based on experimental data, the gradual propagation of matrix cracks is postulated to proceed in the following manner. In-plane tensile stresses ahead of the matrix cracks may cause "local" debonding of the fibers. The existence of "local" debonding was visualized with the numerical simulations presented in Chapter 6. This debonding absorbs energy at the crack tip and has the effect of temporarily blunting further matrix crack growth, and it is consistent with the Cook-Gordon Mechanism of interface debonding (see Gordon, 1979). Upon further loading, the crack continues to propagate around the still intact fiber. Through the process of load redistribution (due to crack formation), the stored energy in the *matrix* temporarily decreases. Only with further loading do microcracks continue to propagate. However, since most of the matrix is near its failure strain, extensive initiation and growth of microcracks occurs over a relatively small stress range. The matrix cracking "saturates" at around the point when the tangent modulus of the axial stress-strain curve reaches a minimum. The acoustic emission data (Fig. 2.4.8) also indicate that most of the matrix cracking occurs over a narrow strain range (0.13–0.23%). Both ultrasonic transducers responded to matrix cracking, presumably because, as was proposed above, each microcrack also causes local debonding.

Zone III is dominated by what is referred to as "global" debonding. This is realized through the ultrasonic data in Fig. 2.4.9 where it is seen that both wave velocities decrease drastically throughout this zone. This is indicative of (out-of-plane) cracks running parallel to the fibers. The increasing tangent modulus in this region indicates that load is being transferred to the fibers. This load transfer creates a shearing action (mode II loading) which in turn would cause global debonding. It is observed that this is a very rapid process since small increases in load led to large drops in ultrasonic wave speed. In addition, in Zone III, despite a constant sampling rate, the stress-strain curves have relatively few data points in Zone III, as compared to the other zones. Upon debond initiation, high tensile

stresses at the crack tip decrease and high shear stresses arise as load is transferred to the fibers. With an analytical model, Dharani and Recker (1991) have shown, that for continued debonding, stresses normal to the fiber become *compressive* and the shear stress plateaus. In this way, the debond is temporarily blunted, requiring additional load transfer for further propagation. It is not known to what extent frictional sliding in the wake of matrix cracks contributes to the toughness in Zone III. In any case, it is not assumed to be significant; since the displacements are small, the energy dissipated by frictional sliding would also be small.

In Zone IV the load is completely transferred to the fibers. The stress-strain curve is nearly linear with a slope of around 68 GPa in this zone. Considering a 41% volume fraction of fibers gives a modulus (for the fibers) of 170 GPa. This is consistent with the data in Table 2.1. Since the slope is relatively constant and there is little acoustic emission activity in this region, it is believed that there are only isolated fiber failures in this zone. In addition, after etching the matrix away from a large piece of a tested specimen, it was found that the majority of the fibers were, still continuous.

In Zone V the global failure crack forms. This failure crack should not be confused with a matrix crack. Rather, the global failure crack is initiated in the vicinity of a bundle of weak fibers. As soon as one fiber fails, the others nearby must carry additional load. In such a process, a global failure crack propagates gradually with large scale frictional pull-out and sliding of the broken fibers. For this reason, the stress-strain curve tends to level off before ultimate failure. The values in Table 2.1 show that the ultimate strain of the composite compares well to the fiber ultimate strain. In addition, assuming that the load near failure is carried by the fiber bundle alone, then the stress in the fiber bundle is approximately 1 GPa at failure. This maximum stress in the fiber bundle is comparable to the ultimate strength of individual fibers as seen in Table 2.1.

The existence of different damage stages has been independently proposed by Sørensen *et al.* (1993) and Wooh and Daniel (1994). In both of these works, the zones were postulated

empirically for modeling purposes. Sørensen *et al.* (1993) suggest an elastic stage, a matrix cracking and debonding stage, a sliding stage, and fiber failure stage. Wooh and Daniel (1994) proposed the following four stages: an elastic stage, matrix cracking stage, interfacial debonding stage, and fiber failure stage.

2.5.3 Explanation of Macroscopic Transverse Behavior

The stress versus transverse strain can also be explained in terms of the five zones of deformation. It is important to realize that the transverse strains are extremely small in comparison to the axial strains. Referring to Fig. 2.4.2, initially, Poisson contraction results in the expected negative slope of the stress versus transverse strain curve. Slight differences in the initial slope for the '1' and '2' directions are believed to be the result of the layered fiber-tow microsctructure. When matrix cracking begins, the transverse strain reverses direction. Presumably, this is because the high tensile stresses at the crack tip generate local debonding, the accumulated strain due to Poisson contraction is released, and the compressive residual stresses in the fibers are relieved. Each of these individual transverse expansions are "integrated" over a finite area by the strain gauge, resulting in a reversal in macroscopic transverse strain.

In Zone III the specimen continues to expand laterally. This is consistent with the notion that Zone III is dominated by global debonding. As was mentioned in Section 2.5.2, the global debonding process is very rapid; this leads to an accumulation of positive transverse strain (expansion). As the load is completely transferred to the fibers, debonding stops. It is within this zone, that strain gauges on different gauge section surfaces and/or different locations on the same surface sensed different amounts of damage. This is indicative of damage induced anisotropy (*i.e.*, $\epsilon_{22} \neq \epsilon_{11}$) and strain gauge sensitivity to damage. In Zone III the side gauges consistently show much less transverse strain accumulation. In addition, some specimens were observed to expand beyond their original lateral dimensions in Zone III. Post-test observation showed that these specimens all had non-planar fracture

surfaces (implying partial shear failure). For one experiment, three transverse strain gauges were all mounted on the same 6.5 mm face. While two of these strains did have positive transverse strain, the other one did not.

As has already been mentioned, at the onset of Zone IV, all of the load has been transferred to the fibers and debonding has stopped. The loading of the fibers results in Poisson type contraction which negates the accumulated transverse strain. Hence, in this zone, the transverse strain undergoes a second reversal. For the transverse strains measured on the 3.25 mm faces of the specimens, since there is relatively little accumulated transverse strain (ϵ_{11}), the second reversal occurs over a small strain range. This is in contrast to the transverse strains (ϵ_{22}) measured on the 6.5 mm faces of the specimens. In Zone V, since it has been postulated that there is no further debonding, any further contraction in the lateral direction is due to a Poisson type effect. Assuming that fibers deform elastically until failure with a Poisson's ratio of 0.28 leads to a failure strain of 0.2% in the lateral direction. This is consistent with the transverse strains on the 3.25 mm face (ϵ_{11}) where there was relatively little accumulated transverse strain.

Several authors (Harris *et al.*, 1992; Sørensen *et al.*, 1992; Nardone and Prewo, 1988) have not encountered a complete second reversal in transverse strain. Instead, in these investigations, it was found that following the second reversal, the strain becomes at most constant and never more negative. Other than the fact that Nardone and Prewo (1988) performed their investigation with carbon fiber reinforced borosilicate glass, the only differences between these authors' experiments and the present experiments are that our specimens and strain gauges were smaller and that the loading rates were different. A smaller gauge will integrate over a smaller area and therefore be more sensitive to microfeatures such as fibers, cracks and debonding. However, as was mentioned above, for the present experiments, approximately 6 matrix cracks were present beneath even the smallest strain gauge. This should be sufficient to yield an average response, and indeed, the axial results for the above works are similar to those presented in this investigation. Due to

the similarities in the axial response, it is also unlikely that the specimen size influences the results. As will be discussed in Chapter 4, loading rate is one possible source of discrepancy in the transverse results. Nardone and Prewo (1988) have documented the "dual reversal" in their experiments with $\pm 10^\circ$ fiber orientation composites. This indicates that shear loading may also play an important role in the second transverse strain reversal.

2.5.4 Analysis of Energy Dissipation

For design of tough ceramic composites, it is desirable to know which damage mechanisms absorb the most energy. Having potentially established the existence and sequence of damage mechanisms throughout the loading history of unidirectional SiC/CAS, it is now left to determine which mechanisms (or zones) dissipate the majority of the unrecoverable strain energy. To accomplish this, it is necessary that the elastic portion of the energy is removed. For the present experiments, this is easily done by calculating the area under the axial stress-strain curve while taking into account the change in axial modulus (E_3). Integrating the area under the curve in this fashion yields the normalized energy dissipation curve shown in Fig. 2.5.2. The energy dissipated is normalized with respect to the total unrecoverable energy dissipated in the experiment.

From Fig. 2.5.2, by definition, the energy dissipated in the elastic zone is zero. Matrix cracking in Zone II dissipates approximately 10% of the energy, and the global debonding debonding in Zone III absorbs roughly 30%. Zone IV releases only 15%, while Zone V dissipates approximately 45%. The fact that the last zone absorbs a large percentage of the energy is consistent with the positive contributions of frictional pull-out and sliding. What should also be noted regarding this large dissipation in Zone V is that most likely a significant portion is due to fiber failures. In designing composites, since the fiber failure indicates that macroscopic failure is imminent, it is not necessarily wise to encourage energy dissipation in zone V. The other relatively large contribution from Zone III indicates that there should be more study of debonding mechanisms. This is especially true considering the lack of

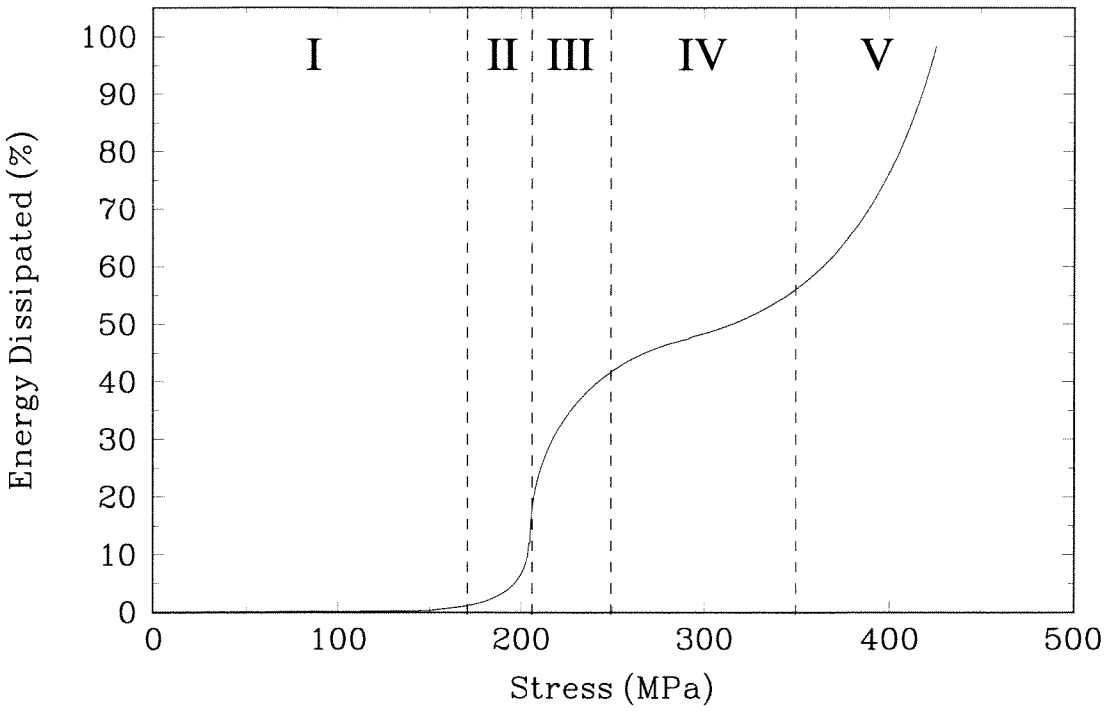

FIG. 2.5.2 A calculation of the energy dissipated by inelastic deformation for each of the five zones.

experimental visualization of the debonding process. It is believed that a significant portion of the toughening in ceramic matrix composites is the result of debonding mechanisms.

2.6 Summary

The experimental methods introduced in this chapter provide a cost effective way of obtaining valid quasi-static tensile data for brittle materials. In addition, methods for making *in situ* strain, acoustic emission and ultrasonic measurements were presented. With these experimental tools, the deformation and failure of a continuous fiber reinforced glass-ceramic composite (SiC/CAS) was studied. The damage mechanisms responsible for toughening of the composite were postulated based on experimental data and post-test scanning electron and optical microscopy. It was observed that upon initiation of damage, the material is no longer transversely isotropic (damage induced anisotropy). The micromechanisms of damage were used to explain the response of the composite at various stress levels. The dominant mechanisms associated with each stress level (zone) are shown

schematically in Fig. 2.6.1. The energy dissipated for each of these zones was calculated. It was found that the third and fifth zones dissipated approximately 75% of the unrecoverable energy. The active mechanisms in each zone are summarized as follows:

I: matrix flaws, possible propagation to fibers, but no further growth and no debonding;
II: matrix cracking, significant growth of matrix cracks with local debonding and fiber bridging;
III: load transfer to the fibers with very rapid global debonding and accumulated transverse strain;
IV: loading of the fibers with isolated fiber failure; and
V: large scale fiber pull-out, frictional sliding, fiber bundle failure, and macrocrack propagation.

The results presented in this chapter indicate which damage mechanisms are active for the complete loading history. Establishing the sequence and extent of the damage mechanisms is necessary for determining the optimal constituents and processing methods for ceramic matrix composites and for developing models of their material response. Since ceramic matrix composites have been proposed for high temperature applications, it is also necessary to determine if the damage mechanisms and/or the sequence of damage mechanisms change as a function of testing temperature. As was the case with structural metallic materials, significant understanding and modeling effort is required before ceramic matrix composites can be reliably incorporated into engineering designs.

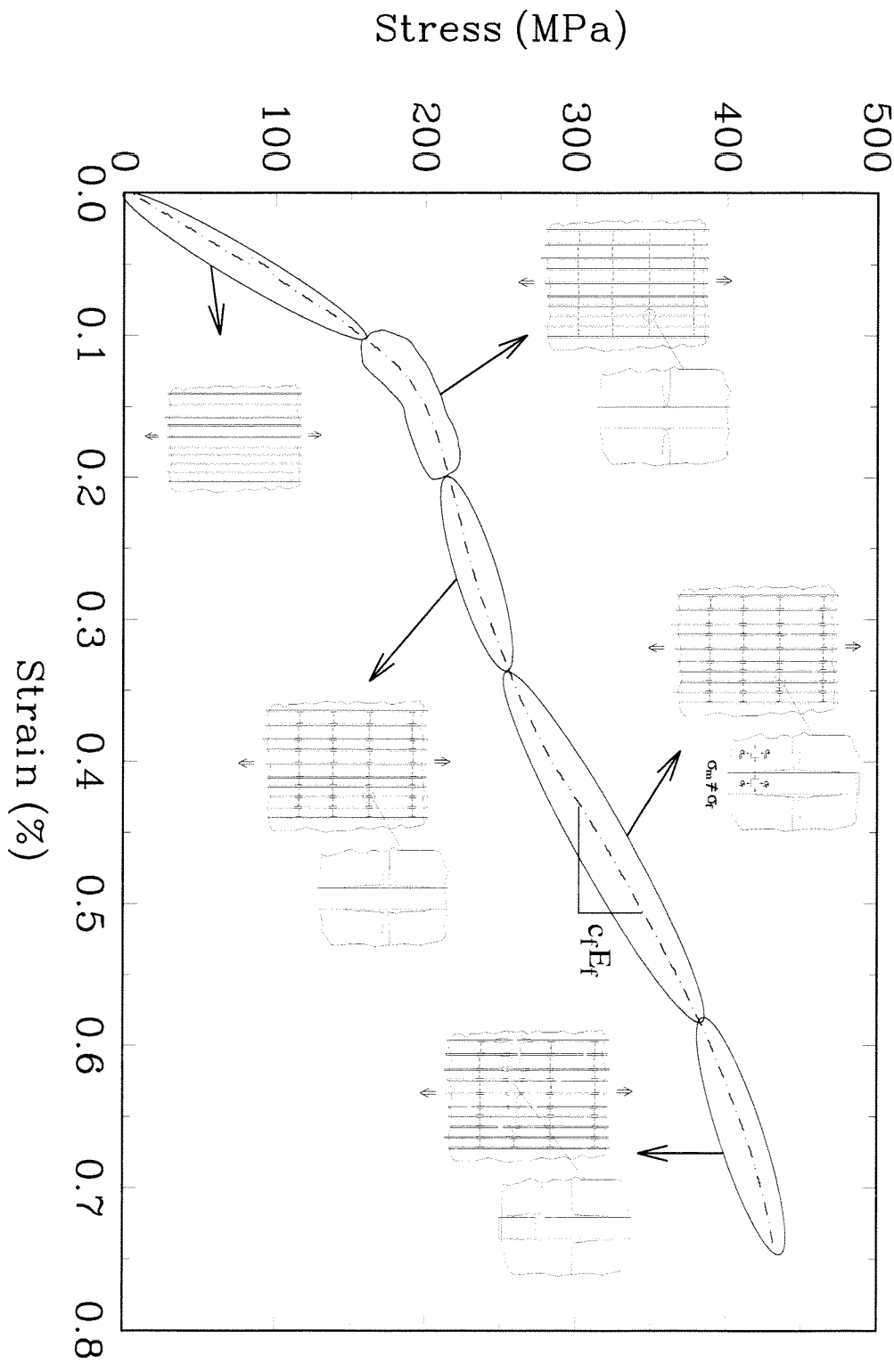

FIG. 2.6.1 Schematics of the dominant mechanisms for each of the five zones indicated on the stress-strain curve.

CHAPTER 3

Modeling of Ceramic Matrix Composites

3.1 Introduction

Before advanced materials can be used in engineering applications, it is necessary that models of their mechanical behavior are developed. These models are the tools which designers use for deciding how much of which material is required for safe and reliable use of the end product over a given period of time. Metals have been studied extensively and there are many models of their post-elastic, fracture and fatigue behavior. Similar studies need to be done for ceramic matrix composites. Thus far, for ceramic matrix composites, it has been generally assumed that the onset of matrix cracking determines the useful strength of the material (Kim and Pagano, 1991). For this reason, there have been many studies to predict the critical stress for matrix cracking.

The shear-lag concept (which assumes that matrix cracks are initiated by shear failure of the interface) was proposed to explain observed periodic matrix cracks in epoxy matrix composites. In 1971, Aveston, Cooper and Kelly (ACK, 1971) performed a complete mechanics analysis of the shear-lag model. The main assumption in this model was that the matrix did not carry any load due to its relatively low stiffness as compared to the fibers. This work has become *classical* and is often referenced in present day shear-lag modeling. Despite the questionable portability of the ACK shear-lag model to ceramic based composites (ceramic matrices are typically at least 75% as stiff as the reinforcement), it has been used and referenced extensively. Aveston and Kelly (1973) and Budiansky, Hutchinson and Evans (BHE, 1986) have modified the original shear-lag model to allow for

a fully bonded fiber-matrix interface or a frictionally sliding interface. The BHE model also accounts for residual stresses, which, as will be shown below, may be quite extensive in the case of ceramic matrix composites. These models all require a long bridged starter crack; other modifications of the ACK model have addressed this requirement. Marshall *et al.* (1985) and McCartney (1992) have re-analyzed the problem with a short starter-crack. The short start-crack caused the critical stress (for matrix cracking) to depend on crack length. Marshall *et al.* (1985) determined the minimum crack size for which the critical stress did not depend on crack length. In addition, this work determined that the minimum crack length was on the order of flaw sizes due to processing. More recently, investigators are realizing that there are no detectable flaws in the material prior to testing. At the very least, it is logical to begin with short starter cracks, however, this also adds another unknown empirical factor to the analysis.

Several research groups are questioning the applicability of steady-state cracking to ceramic matrix composites. Beyerle *et al.* (1992) are currently using the notion of steady-state cracking only as a lower bound for the matrix cracking stress. More recently, Wang *et al.* (1992) have completely removed the required starter crack, instead theorizing that matrix cracking is initiated at randomly distributed microflaws. Kim and Pagano (1991) have found that the critical stress as calculated by using the BHE model overestimates their experimentally determined critical stress. In Chapter 1 several modified shear-lag models and non-shear-lag models were referenced.

To develop a unified model of the deformation of advanced materials an approach which studies the formation, propagation and interaction of damage must be undertaken. This forms the relatively new field of (continuum) damage mechanics (Krajcinovic, 1989). Damage mechanics can be generally divided into the following two categories: phenomenological and micromechanical. The phenomenological approach uses continuous field variables (damage parameters or internal variables). These variables (and their evolution) are usually determined empirically. Talreja (1991) used this approach to determine the uniaxial

response of a ceramic matrix composite. The deformation was divided into different stages and damage parameters selected for each stage. On the other hand, the micromechanical approach analyzes damage on the microscale and then places the results in a homogenizing/averaging scheme. This method has been used primarily to determine effective moduli of materials (Hashin, 1983; Nemat-Nasser and Hori, 1993). Deng and Nemat-Nasser (1992) determined effective moduli of cracking in simulated composites by analyzing (2-dimensional) parallel crack arrays in isotropic or orthotropic elastic solids. More recently, Weitsman and Zhu (1993) used the micromechanical approach with an energy criterion to effectively average an analytical unit cell mechanics solution for matrix cracks in fiber composites. This work was extended to add dissipation from fiber breaks (Zhu and Weitsman, 1994) and thereby model the whole composite response.

In this chapter application of the BHE shear-lag model will be demonstrated and discussed. Comparison will be made to the works of several other authors who have applied this model to their experimental results. Next, micromechanical continuum damage mechanics calculations will be performed for penny shaped cracks in a transversely isotropic material. The acoustic emission results presented in Section 2.4.3 will be used as an estimate of the history of crack density. Phenomenological damage mechanics then yields the evolution of the axial modulus (with damage). Although these results are qualitative, they present an interesting link between acoustic emission data and actual matrix cracking events.

3.2 Models

3.2.1 Existing Shear-Lag Models

In this section, application of the BHE shear-lag model is compared to the experimental results presented in Chapter 2. Following presentation of the results, comparison with other applications of the BHE model are made, and the problems in using this model are discussed.

The BHE shear-lag model considers the following three cases: non-slipping, non-debonding fibers; initially bonded, debonding fibers; and unbonded, frictionally constrained slipping fibers. All of these cases assume steady state cracking (cracking at constant stress) and that there is a long starter crack. For brittle matrix fibrous composites, it is generally assumed that the interface is quite weak and that situation resembles the case of unbonded, frictionally constrained slipping fibers. The critical stress, σ_1, can be written as follows:

$$\frac{\sigma_1}{E} = \left[\frac{6c_f^2 E_f \tau}{c_m E_m E}\right]^{\frac{1}{3}} \left[\frac{\mathcal{G}_m}{aE_m}\right]^{\frac{1}{3}} \tag{3.2.1}$$

where a is the fiber radius, E, E_m, E_f are the moduli of the composite, matrix and fiber, respectively, c_f and c_m are the fiber and matrix volume fractions, respectively, $\mathcal{G}_m$ is the critical mode-I matrix energy release rate and τ is the interfacial shear stress. Other versions of Eq. 3.2.1 have a factor of 2 in the brackets. In such versions, γ_m, representing the fracture *surface* energy of the matrix, replaces $\mathcal{G}_m$. When taking the residual stresses into account the critical stress, σ_{cr}, is written:

$$\frac{\sigma_{cr}}{E} + \frac{\sigma_z^I}{E_m} = \frac{\sigma_1}{E}, \tag{3.2.2}$$

where σ_z^I is the axial residual stress in the matrix.

As was discussed in Section 2.2, the residual stresses in ceramic matrix composites are not well known. Residual stresses will arise because there are thermal expansion coefficient mismatches and because the processing of the composite requires hot pressing and subsequent heat treatment. Since there are possible changes in thermal expansion coefficients during processing and since the role of the fiber-matrix interface is not known, detailed quantitative understanding of the residual stresses is lacking. For illustrative purposes, the residual stresses are calculated based on constant thermal expansion coefficients and no fiber-matrix interface effects. Therefore, with the material properties given in Table 2.1 on page 2.4 and with hot pressing temperatures around 1400°C, significant residual stresses are calculated. The following expressions for the fiber-matrix interface pressure, σ_r^I, and

the residual axial matrix stress, σ_z^I, are derived using a shear-lag model (BHE, 1986):

$$\begin{aligned} \frac{\sigma_r^I}{E_m} &= \frac{1}{2\lambda_1}\left[\frac{c_m}{1-\nu_m}\right]\Omega \\ \frac{\sigma_z^I}{E_m} &= \frac{\lambda_2}{\lambda_1}\left[\frac{E_f}{E}\right]\left[\frac{c_f}{1-\nu_m}\right]\Omega \end{aligned} \tag{3.2.3}$$

where ν_m is the Poisson's ratio of the matrix, Ω is the strain mismatch, and

$$\begin{aligned} \lambda_1 &= 1 - \frac{1}{2}\left(\frac{1-2\nu}{1-\nu}\right)\left(1-\frac{E}{E_f}\right) \\ \lambda_2 &= 1 - \frac{1}{2}\left(1-\frac{E}{E_f}\right) \end{aligned} \tag{3.2.4}$$

where it is assumed that $\nu_m = \nu_f = \nu$. Assuming that the strain mismatch is due only to thermal strains during fabrication, $\Omega = -(\alpha_f - \alpha_m)\Delta T$ where α_f and α_m are the thermal expansion coefficients acting over the temperature range ΔT. Using the material properties in Table 2.1 on page 2.4, one finds that $\sigma_r^I = -54.5$ MPa and $\sigma_z^I = 84.4$ MPa. These stresses are very significant considering that several investigators (*e.g.*, Harris *et al.*, 1992; Daniel *et al.*, 1993) have documented the failure strength of the matrix to be approximately 100 MPa.

By using the indentation technique (Evans and Charles, 1976), the critical stress intensity factor $\mathrm{K_{IC}^m}$ for the matrix material (CAS II) is determined to be $1.6\ \mathrm{MPa}\sqrt{\mathrm{m}}$ ($\mathcal{G}_m = 26\ \mathrm{J/m^2}$). The interfacial shear stress, τ, is calculated by writing the force balance for the shear-lag model (ACK) as follows:

$$\tau = \frac{\sigma_m c_m}{2\pi a N x}, \tag{3.2.5}$$

where a is the fiber radius, $N = c_f/\pi a^2$ is the number of fibers per unit area and σ_m is the critical cracking stress of the matrix. The term $x = \frac{S}{1.364}$ is the effective crack spacing (Aveston *et al.*, 1974), with S being the measured crack spacing. Using a crack spacing of 200μm from the present experimental results, one finds that $\tau = 6.1$ MPa. Together with the values in Table 2.1 on page 2.4, the value for σ_1 is determined to be 225 MPa. Applying Eq. 3.2.2 with a residual stress of 84.4 MPa, one finds that the critical cracking stress, σ_{cr}, is 115 MPa.

Table 3.1 is a summary of five independent applications of the BHE model. Included in this table are the values of τ, $\mathcal{G}_m$ (or $2\gamma_m$) and the residual stress for each application. As can be seen from this table, the results vary widely. Like any model, the BHE model is limited by the simplifying assumptions. For this particular application, it is not known how accurate the assumption of unbonded, frictionally constrained fibers is. In addition, as was shown in Fig. 2.4.5, the microstructure is non-uniform with an overall layered structure and with many fibers close to or touching each other. However, the main problem with the application of this model is its dependence on several poorly determined parameters. In particular, the matrix fracture energy is not well known, and may very well vary greatly between specimen lots. Glass-ceramics typically have matrix fracture energies between 15–30 $\mathrm{J/m^2}$. This also presents another problem related to using properties of the individual constituents. It is unknown to what degree properties of the individual constituents change during processing of the composite. For instance, there may be significant porosity in the neat matrix and leftover binder may affect the matrix properties in the composite. Also difficult to determine is τ. Many researchers use fiber push-out tests (*e.g.*, Marshall and Oliver, 1987; Parthasarathy *et al.*, 1991; Laracurzio and Ferber, 1994) to determine a value for τ. However, fiber push-out tests present new problems for interpreting τ, since curve fitting of experimental results is required and the cutting of small push-out samples most likely significantly alters the stress state. Finally, as was discussed earlier, the residual stresses are not well understood. Within the BHE formulation, high residual stresses lead to a substantially lower critical matrix cracking stress. With the addition of a soft but thin carbon interface layer, one would expect σ_r^I to be similar to that calculated above but that σ_z^I would be much less. This has important implications for the calculation of the critical matrix cracking stress using Eq. 3.2.2.

Although the ACK model was originally derived as a lower bound to matrix cracking. Kim and Pagano's (1991) experience with the model has prompted them to call it an upper bound to their experimentally determined critical stress for matrix cracking. Along these

Table 3.1: Comparison of Various Applications of BHE

Authors	σ_{cr} (MPa)	$\mathcal{G}_m$ (J/m^2)	τ (MPa)	σ_z^I (MPa)
Present Work	115	26	6.1	84.4
Beyerle *et al.* (1992)	150	25	10	89
Kim and Pagano (1992)	233*	2x40	7	—
Harris *et al.* (1992)	135	2x40	5	140
Pryce and Smith (1992)	95*	6	10	—

* no residual stress correction

lines, a more fundamental concern regarding the applicability of BHE or ACK arises. That is, although all specimens tested to stresses above the matrix crack saturation stress have cracks running throughout the width of the specimen, as has been previously discussed, these cracks are not necessarily steady-state cracks. By incrementally loading specimens Pagano and co-workers (Pagano, 1992) have found that the initial cracks (forming in the 100 MPa range) are not steady-state cracks. It is possible, however, that at later loading stages, the cracks do behave as steady-state cracks. However, even if they were steady-state cracks, as was pointed out in the introduction (see Section 3.1), the shear-lag concept was developed for materials in which the matrix is only a small fraction of the stiffness of the reinforcement. Certainly, this is not the case for brittle matrix composites. For application of the shear-lag concept to brittle matrix composites, modifications should be made.

3.2.2 Micromechanical Model

Micromechanical continuum damage mechanics is based on relating deformation of the microstructure to that of the overall material. When a material is cracked, its compliance increases; it is desired to construct a model to calculate this increase in compliance. Following the notation of Mauge and Kachanov (1994), the overall strain for a solid with N cracks can be written for the 2-D case as follows:

$$\begin{aligned} \epsilon = S : \sigma &= S^o : \sigma + \frac{1}{A}\sum_{k=1}^{N}(n\langle b\rangle + \langle b\rangle n)^{(k)} l^k \\ &\equiv (S^o + \Delta S) : \sigma \,. \end{aligned} \tag{3.2.6}$$

where S is the effective compliance, S^o is the compliance without cracks, ΔS is the compliance due to cracks, $n^{(k)}$, $2l^{(k)}$ and $\langle b \rangle^{(k)}$ are the unit normal vector, length and average crack opening displacement (COD) of the kth crack, respectively, and A is the representative area. Note that the ':' represents contraction over two tensorial indices. In what follows, the 3-D case with penny shaped cracks will be analyzed. For this situation the representative area becomes a representative volume and the crack lengths become crack areas.

Having determined the strain in terms of stress, crack density and COD, the complementary energy density can be written as follows:

$$f(\sigma) = \frac{1}{2}\sigma : \epsilon(\sigma) = \frac{1}{2}\sigma : S^o : \sigma + \frac{1}{A}\sum_{k=1}^{N}(n \cdot \sigma \cdot \langle b \rangle)^{(k)} l^k = f^o(\sigma) + \Delta f\,, \qquad (3.2.7)$$

where f^o is the energy without cracks and Δf is the change in energy due to cracks. The change in elastic material constants can be recovered from the complementary energy density through the relation:

$$\Delta S_{ijkl} = \frac{\partial^2 \Delta f}{\partial \sigma_{ij} \partial \sigma_{kl}}. \qquad (3.2.8)$$

Thus determining the effective compliance of a microcracked solid (for non-interacting cracks) reduces to specifying the crack lengths (or density) and determining the CODs.

There are several authors who have derived expressions for the CODs of penny shaped cracks in transversely isotropic solids (*e.g.*, Laws, 1985). For one crack parallel to the plane of isotropy (the '1-2' plane) and for constant far-field applied stress (σ) in the '3' direction, the average normal COD can be written as follows (Laws, 1985):

$$\langle b_n \rangle = \frac{\sigma 4 l^2 \gamma_1 \gamma_2 (\gamma_1 + \gamma_2)}{\pi}\left(\frac{1}{E_1} - \frac{\nu_{12}^2}{E_1}\right), \qquad (3.2.9)$$

where γ_1 and γ_2 are the roots of the following equation:

$$\left(\frac{1}{E_1^2} - \frac{\nu_{12}^2}{E_1^2}\right)\gamma^4 - \left(\frac{1}{E_1 G_{23}} - \frac{2\,\nu_{13}}{E_1}\left(\frac{1}{E_1} + \frac{\nu_{12}}{E_1}\right)\right)\gamma^2 + \frac{1}{E_1 E_3} - \frac{\nu_{13}^2}{E_1^2} = 0\,. \qquad (3.2.10)$$

By defining the crack density, ρ, as

$$\rho = \frac{1}{V}\sum_{k=1}^{N} \pi \left(l^{(k)}\right)^2$$

and using Eq. 3.2.8, the expression for the modulus E_3 can be written as

$$\frac{1}{E_3} = \frac{1}{E_3^o} + 8\gamma_1\gamma_2(\gamma_1+\gamma_2)\left(\frac{1}{E_1} - \frac{\nu_{12}^2}{E_1}\right)\rho\,, \tag{3.2.11}$$

where E_3^o is the modulus of the material with no cracks. Using the average shear COD, one can similarly derive an expression for the change in the shear modulus G_{12}.

In the above, the framework for calculating the evolution of material constants in a transversely isotropic material with non-interacting penny shaped cracks parallel to the plane of isotropy was presented. It is desired to use this formulation to estimate the change in axial modulus of the unidirectional SiC/CAS ceramic matrix composite investigated in Chapter 2. The experiments were performed with uniaxial loading in the fiber direction only. The first step, therefore, is to assume that the matrix cracks which initially form normal to the loading (fiber) direction and which bridge the fibers can be approximated as penny shaped cracks in a transversely isotropic material. Clearly, there are large inaccuracies associated with this assumption. In particular crack closing forces associated with the bridged fibers are neglected and the fact that the cracks are not exactly penny shaped is ignored.

It is now left to calculate the evolution of crack density. Although acoustic emission was used in a qualitative way in Chapter 2, it was anticipated that acoustic emission events might also be quantitatively related to the crack density. A measure of density was extracted from the acoustic emission data by simply integrating the thresholded signal. Within reason, changing the threshold always yielded qualitatively similar results. Thus, since the threshold is arbitrary, it was necessary to scale the resulting integration of the experimental data. As seen in Fig. 3.2.1, after such scaling the experimental density (effective density) compared favorably to results by Beyerle *et al.* (1992). The results presented by Beyerle *et al.* were obtained by counting cracks which were visualized using a surface replication technique.

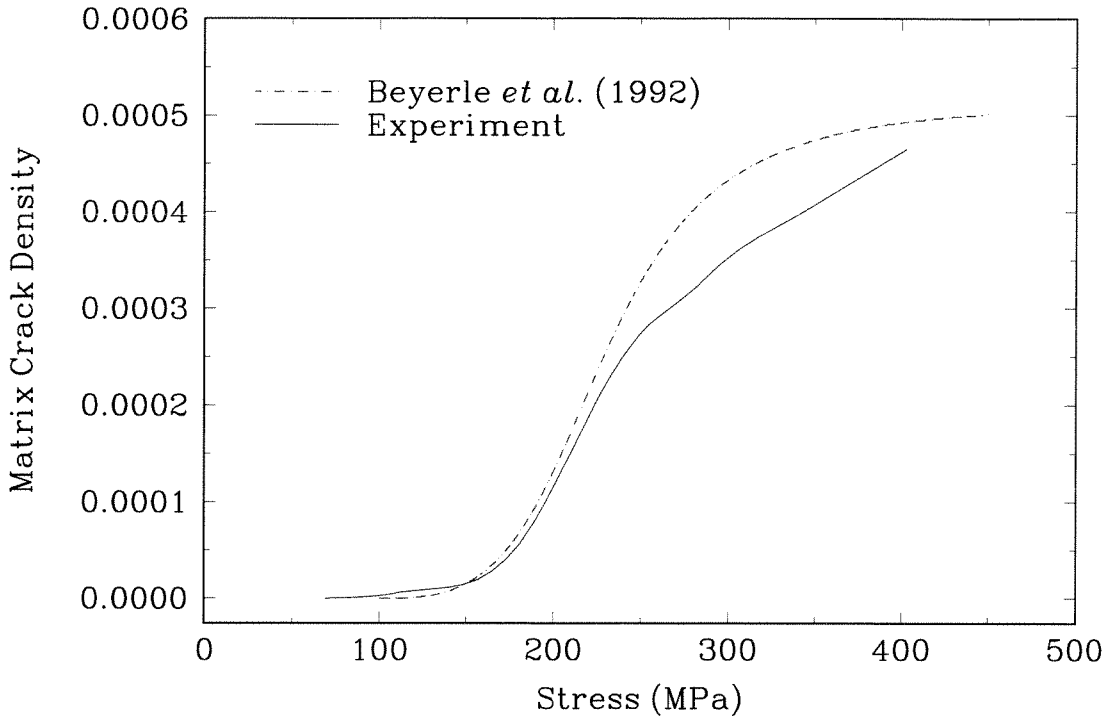

FIG. 3.2.1 Effective density from the acoustic emission data compared to a curve fit of results from Beyerle *et al.* (1992)

Using the effective density and several of the elastic material properties in Table 2.1 on page 2.4, the change in axial modulus of SiC/CAS for uniaxial tension in the fiber direction can be calculated using Eq. 3.2.11. In Section 2.4.4 an experiment for which the specimen was periodically unloaded and then reloaded was described. This simple experiment also provided a measure of how the axial modulus changed (see Fig. 2.4.12). The results from the experiment and from the micromechanical continuum damage model are plotted versus strain and compared in Fig. 3.2.2.

As seen in Fig. 3.2.2, the experimental results and the predictions from the micromechanical model are quite similar. Because of the arbitrary scaling of the experimentally determined effective density, it is not known to to what degree matrix cracks can be regarded as penny shaped cracks. It is possible that the density scaling is also scaling the COD of the matrix cracks, thereby canceling the effect of crack closing forces by the bridging fibers. It is also likely the acoustic emission signal is related to penny shaped cracks in

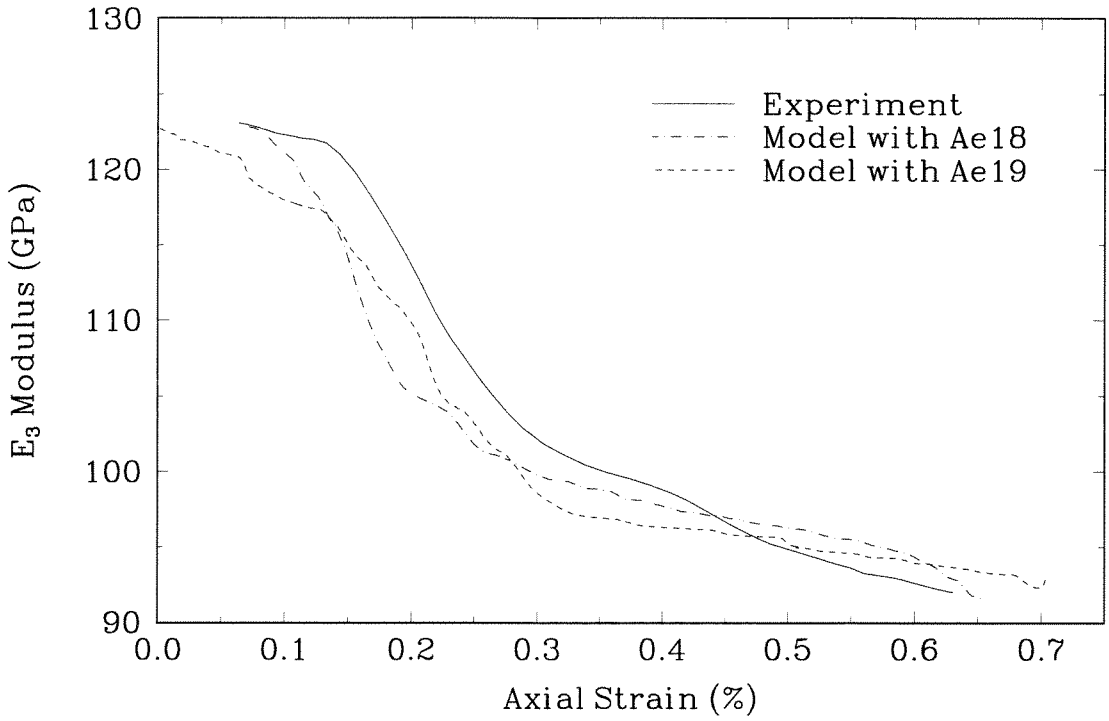

FIG. 3.2.2 Comparison of the E_3 modulus determined directly from an experiment and that calculated using acoustic emission data and damage mechanics.

an averaged sense. Since Eq. 3.2.11 is for average COD and obtaining elastic constants from the complementary energy is essentially a volume averaging procedure, the analytical results are smoothed out and compare favorably to the experimental results. It would be perhaps better to think of this modeling procedure as a combination of micromechanical and phenomenological models with the effective density as an empirically determined damage parameter.

3.3 Summary

Two models for the mechanical response of a unidirectional ceramic matrix composite have been presented. The first model used existing shear-lag theories to calculate the theoretical onset of matrix cracking. Although the results were reasonable, it was shown that this model is dependent on several poorly defined experimental parameters. In the literature, results which use this model vary widely. For the second model, the use of

micromechanics was demonstrated. In this situation, an assumption that matrix cracks can be represented as penny shaped cracks in a transversely isotropic matrix was made. In addition, acoustic emission results were scaled to yield an effective density parameter. It was thus possible to determine the change in axial modulus of a unidirectional ceramic matrix composite for uniaxial tension in the fiber direction. Despite the assumptions it is believed that the results are reasonable in an averaged sense. Comparison of the model results and the experimentally determined change in axial modulus were favorable.

The results presented in Fig. 3.2.2 provide an interesting way of interpreting the acoustic emission data. It would be worthwhile to see if similar results can be obtained for different material systems. Future work in this area requires removing the empiricism of determining the crack density. This, unfortunately requires visualizing the evolution of cracks in three dimensions. By sectioning specimens from experiments which were stopped at various stages of the loading history, it might be possible to visualize the formation of cracks. This is a tedious procedure which is made more difficult by the fact that matrix cracking occurs over a relatively small strain range.

CHAPTER 4

Strain Rate Effects in Ceramic Matrix Composites

4.1 Introduction

Considering that engineering composites are relatively new, it is not surprising that there are few investigations into strain rate aspects of their mechanical behavior. However, many engineering materials are either designed for higher strain rates or will accidentally experience high rates of loading. Since composites have been proposed for numerous applications in the transportation sector, it is very important that strain rate effects are investigated.

Some of the previous studies of composites at different strain rates have been for polymer matrix composites reinforced with discontinuous fibers. Experimental aspects of this work has been carried out by Kander and Siegmann (1992), and using acoustic emission, they found a transition in damage mechanisms at different quasi-static strain rates. Although at higher strain rates the maximum load carrying capability increased, there was also a change from ductile to brittle behavior. The modeling phase of this work by Termonia (1992) showed that for increasing strain rate, the strength of the interface did not affect the mechanical behavior. This may be an important result since interface design in composites is believed to be of paramount importance for tough composite materials (Kerans *et al.*, 1989). It is observed that it was not necessary to go to dynamic strain rates in order to notice these differences in the mechanical behavior.

For brittle matrix composites, Vaidya and Chawla (1994) studied ceramic fibers reinforcing a glass (borosilicate) matrix. Composites were manufactured with both coated and uncoated fibers and experiments were performed at rates within the quasi-static strain rate regime. It was found that at the higher strain rates, both the coated and uncoated fiber composites failed catastrophically with minimal fiber pull-out. The difference was more pronounced for the coated fiber composites. Lankford *et al.* (1992) investigated the SiC (Nicalon) reinforced LAS (Lithium AluminoSilicate) composite system. Experiments were performed at both quasi-static and dynamic strain rates. The results showed that the strain to failure *increased* for dynamically tested specimens. In addition, the results showed a very strong strain rate dependence for matrix crack spacing and fiber pull-out. Multiple strain rates within the quasi-static strain rate regime were not presented by Lankford *et al.* Zhu and Weitsman (1994) did present axial stress-strain curves for two different quasi-static strain rates (0.0013 and 0.0025 mm/min.); however, not only are these minor differences in strain rates, but the results were plotted separately, and no differences for the two loading rates were observed.

In the present investigation we are interested in the effect of strain rate on unidirectional SiC/CAS composites. In order to make comparisons with the previously performed experiments discussed in Chapter 2, the higher rate experiments are also for tension applied in the fiber direction. Experiments were conducted at two strain rates within the quasi-static strain rate regime ($10^{-5}s^{-1}$ and $10^{-2}s^{-1}$). After a very brief discussion of the experimental measurements, acoustic emission, stress-strain and post-test microscopy results are presented and then discussed. The origin of the strain rate dependence is postulated, and experiments which would verify the hypothesis are proposed.

4.2 Experimental Details

The SiC/CAS specimens and the gripping procedure for the higher strain rate experiments was identical to that described in Chapter 2. In order to use a crosshead displacement

rate of 7.5 mm/s, the feedback loop for the MTS described in Section 2.3 was optimized. Strain gauge instrumentation also followed the procedure described in Section 2.3. Acoustic emission detection was performed using both the tuned Micro-30 AE transducer (Physical Acoustics Corp., Princeton, New Jersey) and the broadband #V-129 (normal wave) and #V-157 (shear wave) ultrasonic transducers (Panametrics Inc., Waltham, Massachusetts). Each of these transducers was used only as a receiver, and they were directly connected (AC-Coupled) to the (high-impedance) inputs of a Nicolet 440 Oscilloscope (Nicolet Instrument Corporation, Madison, Wisconsin). All channels were sampled at 200 KHz. Test durations were approximately 0.25 seconds. Due to these short test times, it was not possible to make pulse-echo ultrasonics measurements.

4.3 Experimental Results

4.3.1 Stress-Strain Results

The axial stress versus strain results for higher and lower strain rate tests are shown in Fig. 4.3.1. Results for several different experiments at both the lower ($10^{-5}s^{-1}$) and higher ($10^{-2}s^{-1}$) strain rate experiments are presented. The mechanical response at the two different strain rates is quite different. The higher rate experiments have a much larger initial linear region, with the onset of nonlinearity delayed by nearly twice the stress. After non-linearity, for the higher rate experiments, the strain increases at nearly constant stress. Further loading leads to a rapid stiffening response and then subsequently, macroscopic failure. Ultimate failure appears to be at nearly the same strain level and at slightly higher stress levels.

The axial stress versus transverse strain response for the two different rates of loading is shown in Fig. 4.3.2. Again, the differences are quite significant. For the higher rate experiments, the larger linear region in the axial response is manifested in the transverse data by a larger zone of Poisson contraction. The subsequent reversal in strain is quite

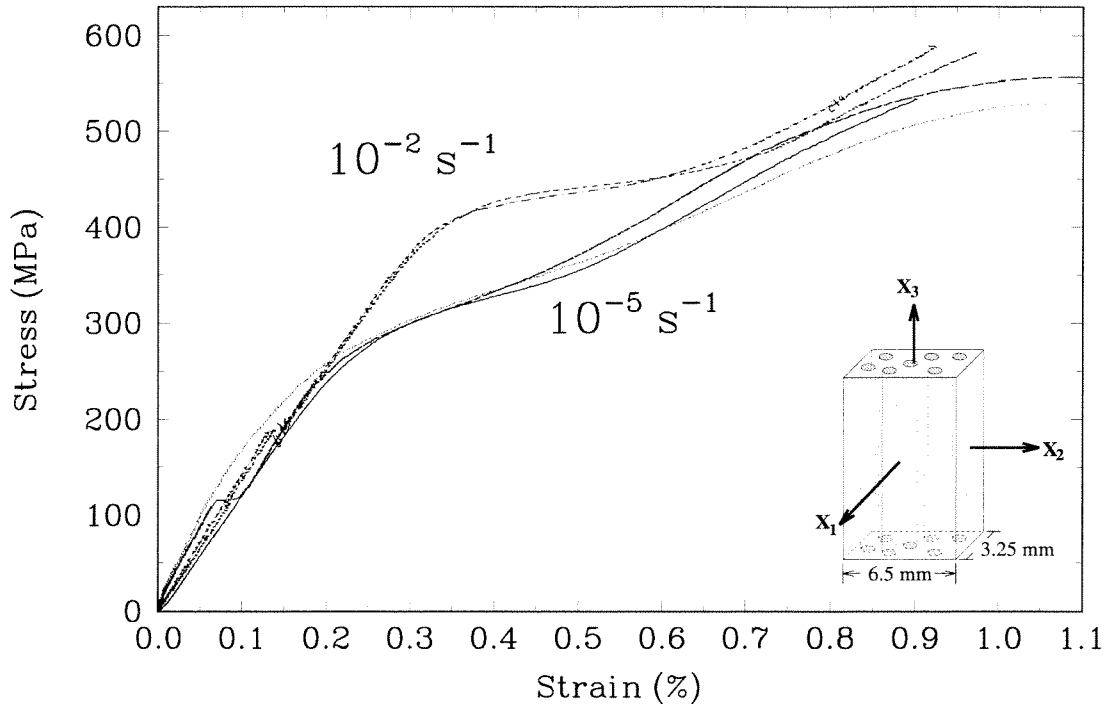

FIG. 4.3.1 The axial (x_3) stress versus axial strain for unidirectional SiC/CAS specimens at two different strain rates.

sharp, and the lateral expansion is much greater than for the lower rate experiments. For both of the higher rate experiments shown, the specimen has expanded beyond its original dimension. The second complete reversal seen at lower loading rates is not present for the higher rate experiments. Instead, at higher rates, the specimens continue to expand until ultimate failure is reached.

4.3.2 Acoustic Emission Results

In Fig. 4.3.3, an axial stress versus strain curve is presented along with results from acoustic emission (AE). The AE data was obtained using the broadband ultrasonic shear wave transducer. As discussed in Section 2.3.3, the acoustic emission results are obtained by digitally filtering the raw AE signal and then thresholding the filtered signal. The resulting counts show three large, but isolated spikes, followed by a nearly Gaussian shaped distribution of counts, a relatively quite region, and then an increase in activity just before ultimate failure. The three initial spikes are believed to be grip noises which cover a range

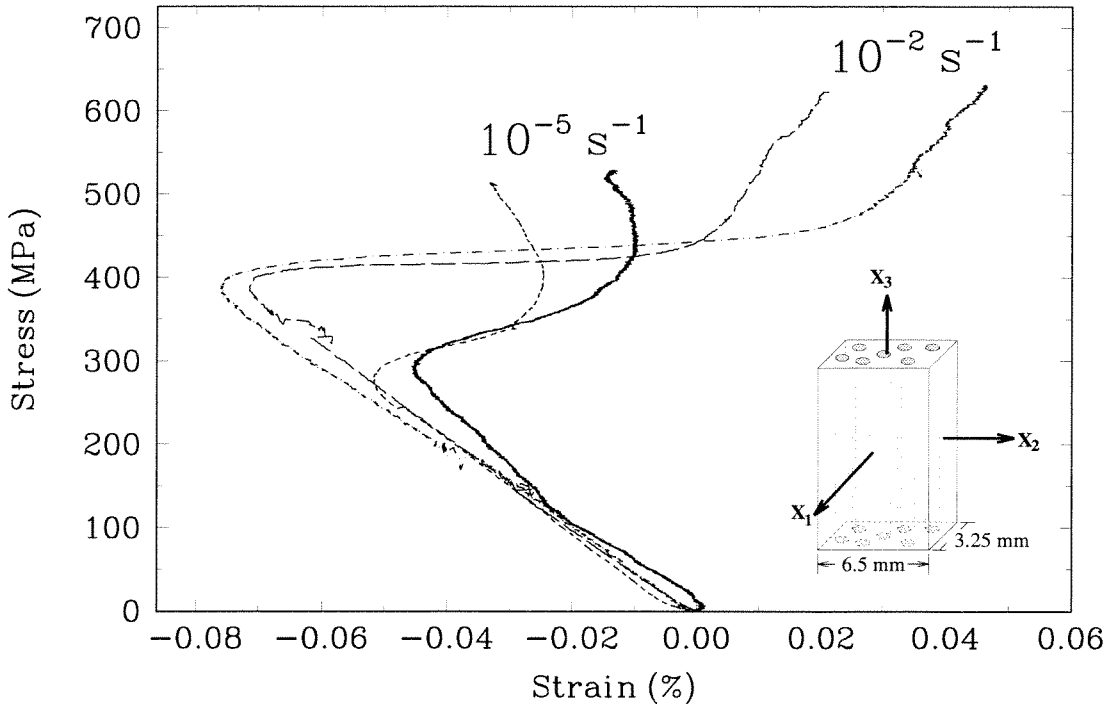

FIG. 4.3.2 The axial (x_3) stress versus transverse (x_2) strain for unidirectional SiC/CAS specimens at two different strain rates.

of frequencies and thus could not be filtered out. The number of these isolated spikes varied from one experiment to the next. The Gaussian region is understood to be the result of matrix cracking, and the gradual buildup near ultimate failure most likely results from isolated fiber failures. When comparing to the AE results for lower rate experiments (presented in Fig. 2.4.8), it is seen that the matrix cracking region is delayed both in absolute strain and with respect to the non-linear portion of the stress strain curve.

4.3.3 Micromechanisms of Deformation

Post-test microscopy on specimen sections polished parallel to the fibers was performed. The results are shown in Fig. 4.3.4 and Fig. 4.3.5 for lower and higher rate experiments, respectively. It is seen that the bridging mechanisms are not as efficient for the specimens tested at higher rates; several of the fiber bridging cracks appear to stop in the middle of the polished sections. This is not the case for the specimens tested at lower rates; all of the cracks can be traced completely across the field of view. In addition, on

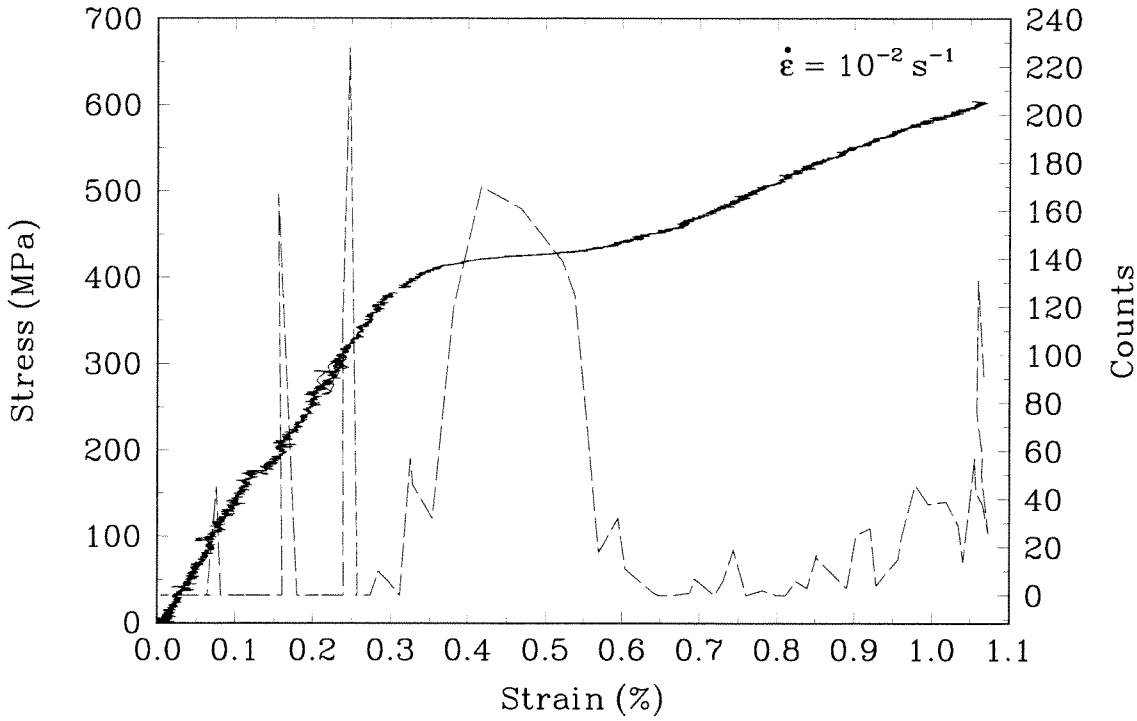

FIG. 4.3.3 Acoustic emission results plotted along with the axial stress-strain curve for the higher strain rate.

average, the crack spacing for the high rate experiments is less than that for the lower rate experiments. Observations of macroscopic fracture surfaces (Fig. 4.3.6 and Fig. 4.3.7) show significant differences; it is apparent that the pull-out lengths for the higher rate experiments are much less. In addition, it is seen that for the higher rates tested specimens, the crack plane is much more discontinuous (stair-stepped) than for the lower rate tested specimens. The macroscopic crack followed a tortuous path with many out of plane jumps.

4.4 Discussion

The experiments with unidirectional SiC/CAS have indicated that there are changes in the deformation (damage) mechanisms for different loading rates within the quasi-static strain rate regime.

The first obvious change in the mechanical response is that the onset of non-linearity occurs at a load that is nearly double that for the lower strain rate experiments. In Section 2.5.2 it was proposed that for the lower rate experiments, the onset of non-linearity

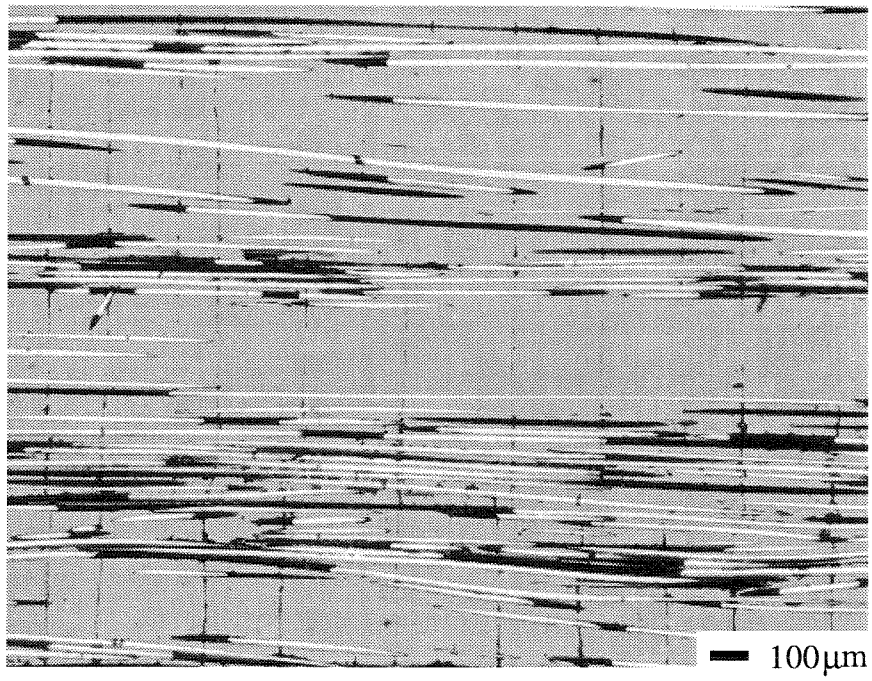

FIG. 4.3.4 A post-test optical micrograph of periodic cracking for a lower rate experiment.

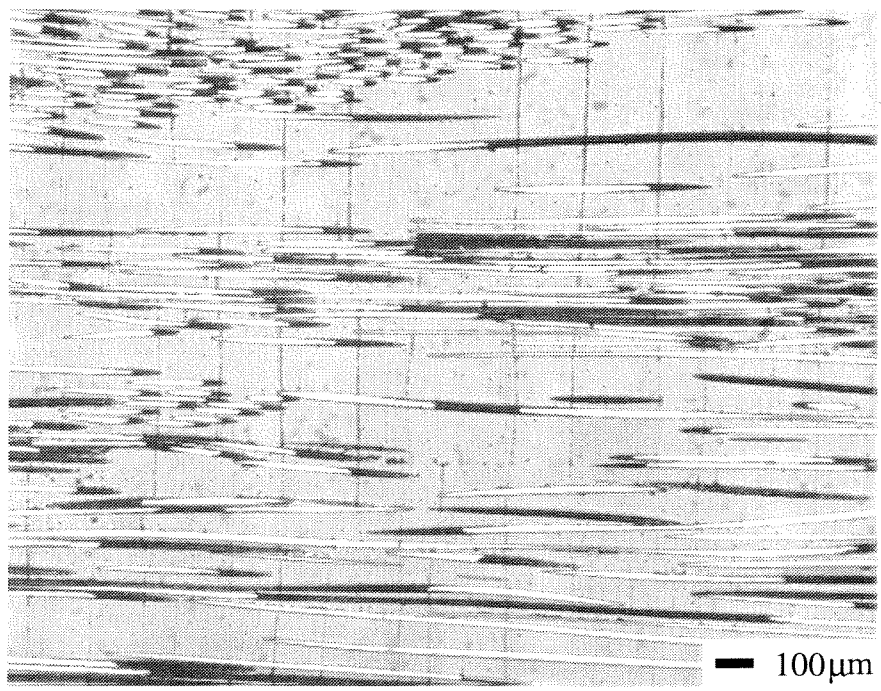

FIG. 4.3.5 A post-test optical micrograph of periodic cracking for a higher rate experiment.

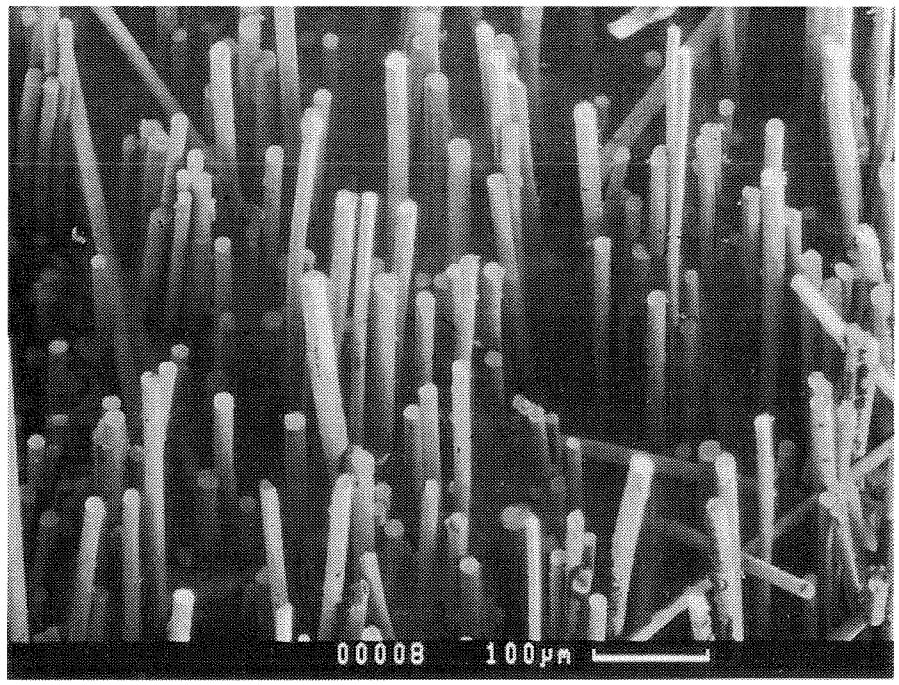

FIG. 4.3.6 An SEM micrograph of the macroscopic fracture surface of a specimen tested at a lower strain rate.

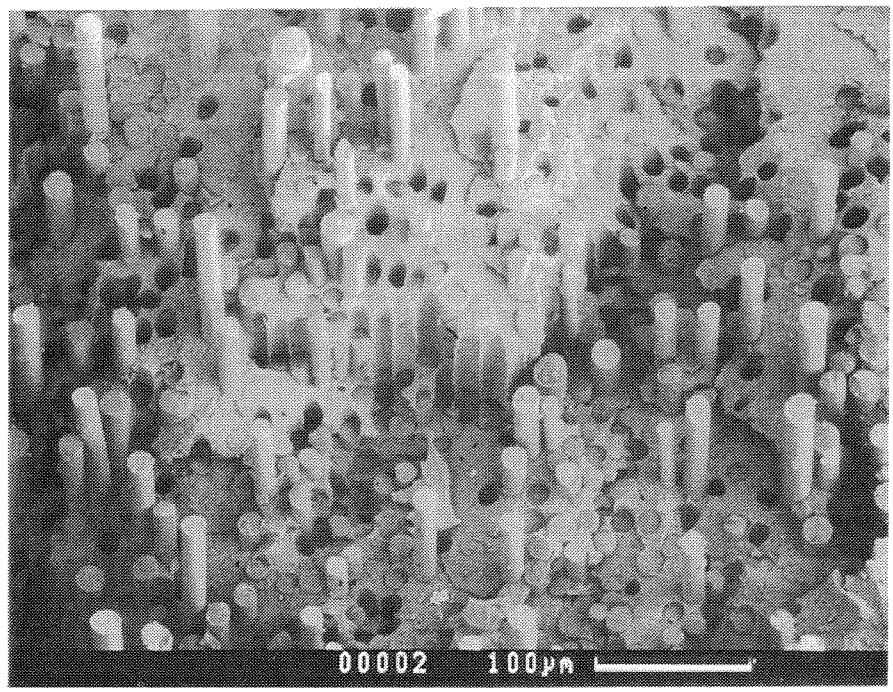

FIG. 4.3.7 An SEM micrograph of the macroscopic fracture surface of a specimen tested at a higher strain rate.

is associated with matrix cracking. There is no reason why that would not be the case for the present, higher rate experiments. However, for the present experiments, it was observed that, in terms of overall macroscopic strain, the matrix cracking was significantly delayed. In other words, the matrix does not reach its critical failure strain until the system is under higher loads. The reason for the delay is unknown. It is possible that there are rate sensitivities associated with the matrix and/or the load transfer mechanisms.

Once the matrix is at its critical failure strain, it appears that the matrix cracking also continues over a larger strain range. This was experimentally realized with acoustic emission results. In terms of the zones of deformation presented in Section 2.5.2, the implication is that for the higher strain rate experiments, Zones II and III have blended together with each matrix crack incurring significant load transfer and global debonding. In Chapter 5 experiments with a model brittle matrix composite material are described. For lower to higher strain rate experiments with the model material, there was a clear transition from periodic cracking of the matrix to a single matrix crack with reinforcement debonding. This is analogous to the present results, for which it believed that debonding plays a more significant role at higher strain rates. A consequence of more debonding is the increased transverse expansion shown in Fig. 4.3.2. The cause of the increase in debonding is also unknown. As was the case with the delayed onset of matrix cracking, rate sensitivities of the different constituents (including the interface) could be playing a role. Presumably the sequence of load transfer between the different constituents was also altered by the different loading rates; it is not known if this is the *result* or the *cause* of the change in damage modes. An additional reason for the change in damage modes could be the result of local inertial effects. It is believed that matrix cracks propagate dynamically, and, considering the different length scales within the problem (fiber diameter and spacing, cracking spacing, interface thickness, *etc.*), it is possible that inertial effects influence the kinetics of damage formation and propagation.

As indicated by the post-test optical microscopy in Figures 4.3.4 and 4.3.5, the matrix cracking at higher loading rates is more isolated (some matrix cracks terminated within the matrix) and not as periodic. This is consistent with the acoustic emission data which shows that matrix cracking occurs over a larger strain range. Also, as seen in Figures 4.3.6 and 4.3.7, in addition to there being significantly less pull-out at higher loading rates, the macroscopic crack plane is also quite wavy. The decreased pull-out length is consistent with a delayed matrix cracking and an increase in debonding. The delayed stiffening response of the higher rate experiments indicates that the fiber bundle does not begin to carry significant load until higher macroscopic strain is reached. Since this processes is also seen to be more rapid, presumably there is less time for isolated fiber failures. This would allow the fiber bundle to carry more load and lead to a slightly higher ultimate stress. In addition, this delayed loading of the fiber bundle along with increased debonding could cause the incomplete second reversal in the transverse strain. Unlike for the lower rate experiments, for the higher rates of loading, there is no time for debonds to close and for Poisson contraction of the fibers to be sensed by the transverse strain gauges.

The present experimental results differ from those of Vaidya and Chawla (1994) in that it was found that the increased strain rate did not lead to a more brittle material response. Most likely this disparity is a result of the different material systems. One similarity between the present results and those of Vaidya and Chawla is that increased strain rates did significantly reduce fiber pull-out lengths.

Although the SiC/LAS system used by Lankford *et al.* (1992) is very similar to the present specimen material, it is difficult to make comparisons because the quasi-static stress-strain curve presented by Lankford *et al.* is quite different from that in the present experiments. In addition, it is possible that there is a transition to increased "flow" and increased fiber pull-out under *dynamic* rates of loading. For the present experiments, as has already been mentioned, there was a decrease in pull-out length and the failure

strain remained approximately constant for the higher (but still quasi-static) strain rate experiments.

A number of simple tests could be performed to elucidate some of the details of the rate sensitivity of the unidirectional SiC/CAS composites. These tests would involve both stopping tests and/or jumping to different strain rates at selected points during the deformation history. In this way, it would be possible to determine the state of damage at various stages. In addition, the jump tests would determine if there are rate sensitivities inherent in the material. This latter possibility exists since the *in situ* properties (including the rate sensitivity) of the matrix, the fiber-matrix interface and the fibers are not well known (Cooper, 1994).

4.5 Summary

This study has shown that even within the quasi-static strain rate regime, the rate of loading is an important variable for SiC/CAS composites. For the first time, significant differences between lower strain rate and higher strain rate mechanical behavior were presented. The experimental measurements led to the conclusion that the kinetics of damage formation and propagation were altered by different rates of loading. In addition, the extent of damage was also changed. Various reasons for the change in damage mode were postulated. Since damage in composite materials is the method by which these materials are made tougher, this work has important implications for composite materials design.

Experiments for which the specimen is unloaded and/or the strain rates are changed at specific points in the deformation history would provide more detailed information on the origin of the strain rate dependence. It is also desirable to see if there are more significant differences in the macroscopic failure for *dynamic* rates of loading. Before ceramic matrix composites can be used in applications such as high speed aircraft engines, their mechanical behavior needs to be understood for loading rates ranging from quasi-static to dynamic.

CHAPTER 5

Model Composite Experiments

5.1 Introduction

As has been seen in Chapter 2, the multi phase nature of composite materials has considerable effect on the material response. These changes are beneficial in that they introduce nonlinearity (toughening) to materials which would otherwise fail in a brittle fashion. For the ceramic composite investigated in Chapter 2, the material response was divided into 5 zones of deformation (see Section 2.5). Within each zone a different damage mechanism is presumed to dominate. Thus, it is the damage mechanisms (matrix cracking, debonding, fiber sliding and pull-out) which provide for a nonlinear material response. Various methods have been used to investigate individual damage mechanisms in an averaged sense. These methods include acoustic emission and ultrasonics. For more detailed analysis, it is necessary to isolate individual damage mechanisms in a controlled, easily analyzed environment. Experiments which effectively isolate different aspects of the material response of more complicated materials are referred to as "model experiments."

There have been relatively few experimental investigations of model materials which mimic fiber reinforced composites or the damage therein. Under fatigue loading Botsis and Shafiq (1992) studied the effect of fiber spacing on crack bridging for a line of glass fibers in an epoxy matrix. Using the same material system, crack initiation and propagation was studied as a function of crack spacing (Botsis and Beldica, 1994). In both of these studies, since the matrix and fibers were transparent, damage could be observed in real time. In the present investigation the model material resembles a fiber composite only in that it is

composed of a brittle material symmetrically reinforced by a strong material. When viewed on a smaller scale, the problem looks like that of a crack in a weak material propagating perpendicular to an strong material. Much of the previous work with cracks and interfaces is related to cracks along the interface (*e.g.*, He and Hutchinson, 1989b; Lambros and Rosakis, 1995; Geubelle and Knauss, 1994). The near-tip analysis of a crack impinging (perpendicularly) on a debondable interface has been theoretically investigated by Dollar and Steif (1992). In this study stress concentrations from the cracks were determined for various load levels and debond states. In an earlier study, Dollar and Steif (1989) found crack tip stresses to be highly dependent on the coefficient of friction. He and Hutchinson (1989) have studied the branching of cracks approaching an interface. There are no known studies of rate effects for cracks propagating perpendicularly to a strong material.

In this chapter, experiments which isolate the propagation of cracks in a brittle material are described. In addition, the interface between the brittle material and strong reinforcement is observed to debond under certain conditions. The materials for the model experiments were chosen to simulate a brittle matrix reinforced by strong fibers. Loading was applied parallel to the reinforcement to mimic the experiments described in Chapter 2, and experiments were performed at two different strain rates within the quasi-static strain rate regime. The model material response has several similarities to that of the ceramic composites. In particular, a transverse strain reversal was observed, and strain rate was found to have an important effect. The method of Coherent Gradient Sensing was used to qualitatively understand nature of the stress fields in the vicinity of the "damage" and for different strain rates. Throughout this chapter, "matrix cracking" will be used to refer to the propagation of cracks within the brittle (matrix) material. The term, "debonding," will refer to the propagation of cracks along the reinforcement-matrix interface.

5.2 Experiments

To analyze what happens when a crack in a brittle material encounters a tough reinforcement, the specimen shown in Fig. 5.2.1 was designed. The epoxy resin, Homalite 100 (The Homalite Corporation, Delaware), was cut and milled from $^3/_{16}$" plate stock into $^5/_8$"$\times$6" strips. Homalite was chosen as the "matrix" because it is optically transparent and very brittle. Aluminum was used for "fibers" because it is both tough and has a relatively low modulus. Since Homalite 100 has a Young's modulus of approximately 4 GPa, the low modulus of aluminum (approximately 70 GPa) was desired in order to keep the modulus mismatch low. The resulting modulus mismatch for the above described "composite" is greater than that of the SiC/CAS ceramic composite described in Section 2.2. However, this mismatch is more typical of brittle matrix composites than of other composite systems (*i.e.*, polymer matrix composites). As shown in Fig. 5.2.1, the aluminum strips were machined into half dog-bone shapes (gauge section area: $^5/_{64}$"$\times$ $^3/_{16}$") to insure deformation in the gauge section. The aluminum strips were first grit blasted and then glued to the as-machined (milled) Homalite using Loctite Depend Adhesive (Loctite Corporation, Aurora, Illinois). The composite specimen was clamped together during the gluing procedure; this yielded a thin interface layer of glue which was consistent from one specimen to the next. The resulting interface can be thought of as analogous to the carbon interface present in most brittle matrix composites. Another detail of the specimen preparation is the introduction of an initial stress concentration. A $^3/_{64}$" hole was drilled in the center of the Homalite strips. A jewelers saw was used to cut wing cracks on the hole, and a razor blade was used to further sharpen the wings. This ensured that the initial "matrix" crack would start perpendicular to the reinforcement and that it would be within the field of view of the Coherent Gradient Sensing optical technique. Finally, the aluminum and the Homalite were ground flat in the grip section to guarantee that both the materials were uniformly loaded in the far field.

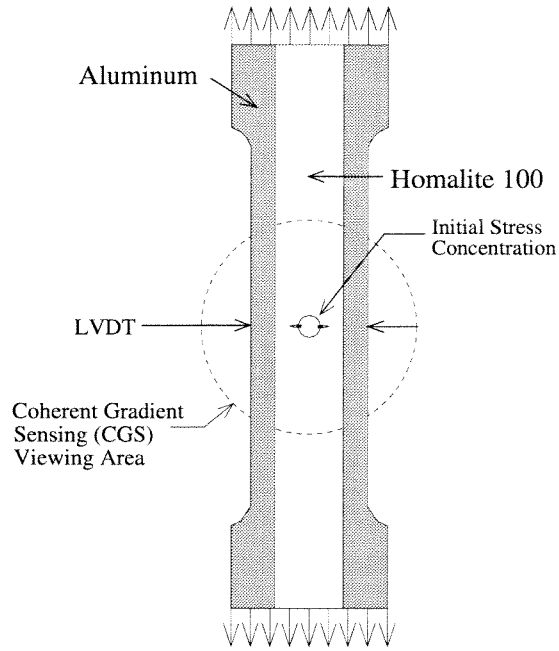

FIG. 5.2.1 A schematic of the specimen for the model experiments.

5.2.1 Load Frame Details

The specimen described above was loaded using an MTS Tension/Torsion (MTS Corporation, Minneapolis, Minnesota) load frame. The specimen was gripped with Instron (Instron Corp., Massachusetts) wedge grips. The experiments were run in displacement control, and load and displacement were output directly from the MTS controller to a Nicolet 440 oscilloscope. A Lucas Schaevitz (Lucas Control Systems Products, Hampton, VA) Model 025-MHR Linear Variable Differential Transducer (LVDT) was used to measure the transverse displacement of the specimen. This LVDT was chosen because it is small, lightweight, and has a very high sensitivity (7.8 mV/V per 0.001"). The LVDT and its non-ferrous core were mounted on aluminum pieces which were glued to the specimen using Loctite Multi-Bond Adhesive 312. As indicated schematically in Fig. 5.2.1, the LVDT was mounted directly across the initial stress concentration.

For high accuracy, it is best to drive LVDTs with AC signals, and therefore it is also necessary to demodulate the resulting LVDT signal into DC. Driver electronics from Sangamo (Solatron Tranducers, West Sussex, England) were used for both the driving and

demodulating. A schematic of the LVDT electronics is shown in Appendix D. The oscillator produces an oscillating voltage (sine-wave) for the LVDT and a reference voltage and clock signal for the demodulators. As indicated in the schematic, the 10 kHz frequency and 3V rms amplitude options were set on the oscillator. Using the amplitude and phase shift of the LVDT output along with the reference voltage and clock signal from the oscillator, the demodulator outputs the DC signal which is directly related to the position of the core within the LVDT (displacement). Additional options on the demodulator give the user means to zero the transducer output and to increase the gain of the output signal using trimpots. To remove high frequency noise associated with the LVDT and its electronics, the output from the demodulator is low pass filtered using a Preston (Preston, California) 8300 XWB Amplifier. The output from the Preston Filter/Amplifier is recorded using a Nicolet 440 oscilloscope.

5.2.2 Coherent Gradient Sensing (CGS)

The optical method of CGS for use in mechanics was first proposed by Tippur *et al.* (1991). A schematic of the setup for the present experiments is shown in Fig. 5.2.2. A 50 mm coherent, monochromatic collimated laser beam is transmitted through the deforming specimen. For reasons which will be explained below, during deformation of the specimen the laser beam acquires an optical path difference which is a function of the in-plane coordinates (x_1, x_2). The now non-collimated laser beam passes through two line diffraction gratings, G_1 and G_2 of pitch (inverse line spacing) p. The gratings are positioned at a distance Δ apart. The output from the two gratings is transmitted though a filtering lens L. This results in diffraction spots on the filtering plane. Blocking all diffraction orders except a first order diffraction spot (± 1) allows the interference pattern to be imaged and stored by the CCD camera.

The CGS interferometer is a lateral shearing interferometer which has been rigorously analyzed with Fourier optics by Tippur (1992) and Lee *et al.* (1995). However, based on the

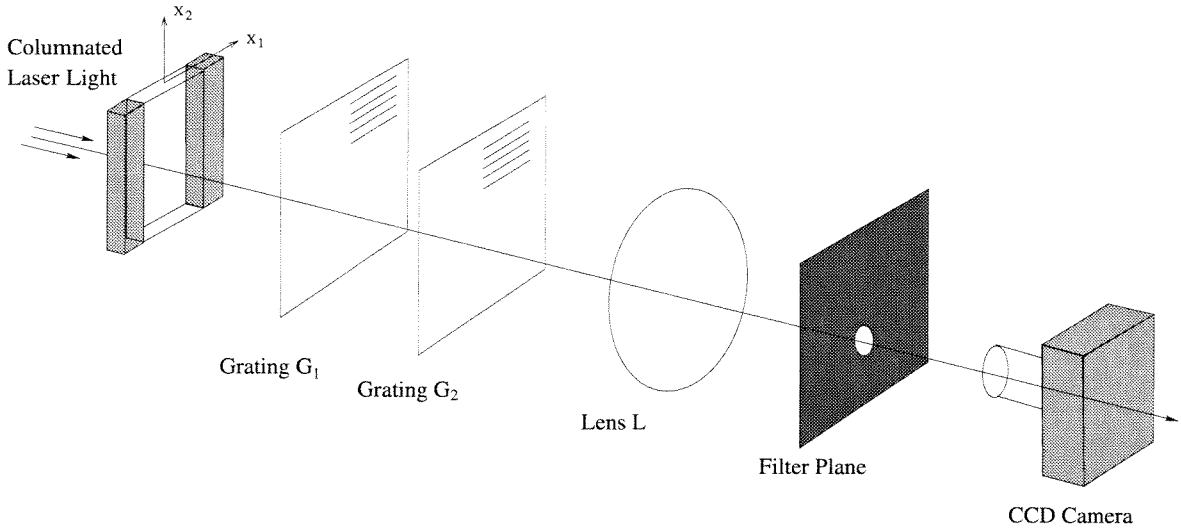

FIG. 5.2.2 A schematic of the CGS setup for the model experiments.

diffracted wave fronts shown in Fig. 5.2.3 and following the work of Murty (1964), a simple explanation of the CGS interferometer is presented. Without loss of generality, the line gratings are assumed to have a sinusoidal transmittance. Thus, a plane wave propagating along the optical axis will be diffracted into three wavefronts (E_0 and $E_{\pm 1}$) by the first grating (G_1). The angle of the propagation directions for E_0 and $E_{\pm 1}$ is given by the diffraction equation

$$\theta = \sin^{-1}\left(\frac{\lambda}{p}\right) \approx \left(\frac{\lambda}{p}\right) , \tag{5.2.1}$$

where λ is the wavelength of light and p is the grating pitch. For the helium-neon laser and gratings used in the present experiments ($\lambda = 632$ nm and $p = 0.025$ mm/line), $\theta = 1.4°$. The second grating (G_2) will diffract each of the three wavefronts incident on it into three additional wavefronts. Thus, as can be seen in Fig. 5.2.3, nine wavefronts will emerge from G_2. The wavefront pairs ($E_{0,-1}$,$E_{-1,0}$) and ($E_{1,0}$,$E_{0,1}$) are parallel and are therefore filtered to the same spot on the filtering plane. In addition, these wavefront pairs are copies of the original deformed wavefront emerging from the specimen and are sheared by a distance ω which is given by

$$\omega = \Delta \tan\theta \approx \Delta\theta \tag{5.2.2}$$

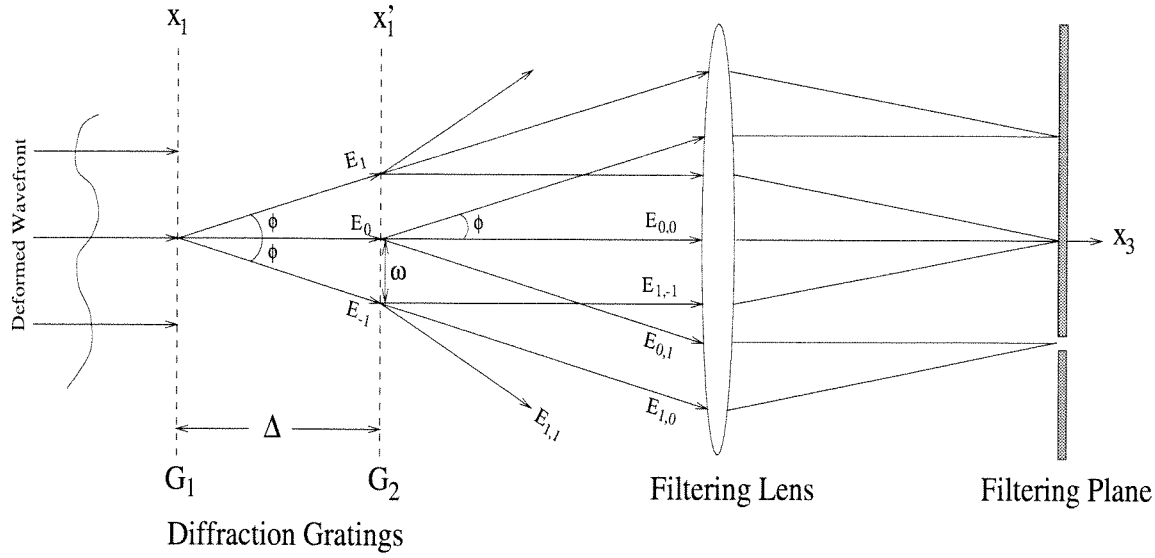

FIG. 5.2.3 Diffracted wavefronts within the CGS interferometer.

for small shearing (*i.e.*, small θ).

The deformed wavefront emerging from the deforming specimen can be mathematically represented as having a phase (optical path) of $S(x_1, x_2)$. For shearing in the x_1 direction, the condition for constructive interference on the image plane of the camera is

$$S(x_1 + \omega, x_2) - S(x_1, x_2) = m\lambda \ , \tag{5.2.3}$$

where $m = 0, \pm 1, \pm 2, \ldots$. Upon dividing both sides of Eq. 5.2.3 by ω and using the relations in Eq. 5.2.1 and Eq. 5.2.2, the following equation results:

$$\frac{S(x_1 + \omega, x_2) - S(x_1, x_2)}{\omega} = \frac{mp}{\Delta} \ . \tag{5.2.4}$$

If the two diffraction gratings are moved together (*i.e.*, $\Delta \to 0$) or the grating pitch is increased (*i.e.*, $p \to 0$) then $\omega \to 0$. From Eq. 5.2.4, the condition for interference then becomes

$$\frac{\partial S(x_1, x_2)}{\partial x_1} = \frac{mp}{\Delta} \qquad m = 0, \pm 1, \pm 2, \ldots \ . \tag{5.2.5}$$

Similarly, if the grating lines are parallel to the x_1 direction, the condition for interference becomes

$$\frac{\partial S(x_1, x_2)}{\partial x_2} = \frac{np}{\Delta} \qquad n = 0, \pm 1, \pm 2, \ldots . \tag{5.2.6}$$

Now that the condition for interference has been related to the change in optical path length, for solid mechanics applications, it is necessary to relate the change in optical path length to the deformation of the specimen. As shown in Fig. 5.2.2, we assume that a planar wavefront is normally incident on the specimen which lies in the $x_1 - x_2$ plane. The transparent material is assumed to be optically and mechanically isotropic with a uniform thickness of h and a refractive index of n. The equation for the transmitted wavefront becomes $x_3 + S(x_1, x_2) =$ constant, where $S(x_1, x_2)$ is the optical path length change acquired during refraction. As discussed in detail by Rosakis(1993), $S(x_1, x_2)$ can be related to the deformation state by

$$S(x_1, x_2) = 2h(n-1) \int_0^{\frac{1}{2}} \epsilon_{33} \mathrm{d}\left(\frac{x_3}{h}\right) + 2h \int_0^{\frac{1}{2}} \delta n \mathrm{d}\left(\frac{x_3}{h}\right) . \tag{5.2.7}$$

The first term in equation Eq. 5.2.7 represents the net optical path length change due to the plate thickness change caused by the strain component ϵ_{33}. The second term is the net optical path length change due to the stress induced change in refractive index. The change in refractive index with stress is given by the stress optic relation (Maxwell relation),

$$\delta n = D_1(\sigma_{11} + \sigma_{22} + \sigma_{22}) , \tag{5.2.8}$$

where D_1 is the stress optic coefficient and σ_{ii} $(i = 1, 2, 3)$ are the Cartesian components of the stress tensor. Given the isotropy assumptions, the strain component, ϵ_{33} can be related to the stress components, and Eq. 5.2.7 becomes

$$S(x_1, x_2) = 2hc_\sigma \int_0^{\frac{1}{2}} \left\{ (\sigma_{11} + \sigma_{22}) \left[1 - D_2 \left(\frac{\sigma_3 3}{\nu(\sigma_{11} + \sigma_{22})} \right) \right] \right\} d\left(\frac{x_3}{h}\right) , \tag{5.2.9}$$

where

$$c_\sigma = \left[D_1 - \frac{\nu}{E}(n-1) \right] \qquad \text{and} \qquad D_2 = -\left[\frac{\nu D_1 + \frac{\nu(n-1)}{E}}{\frac{D_1 \nu (n-1)}{E}} \right] .$$

In the above, E and ν are the Young's modulus and Poisson's ratio of the material, respectively.

It is clear from Eq. 5.2.9 that $S(x_1, x_2)$ depends on the three dimensional stress state. In particular, the stress state will be three dimensional in the vicinity of crack tips. A summary of the relevant numerical analysis of the three dimensionality of homogeneous and interfacial cracks in plates is given by Rosakis (1993). These numerical simulations have shown that for homogeneous cracks in plates, plane stress conditions exist in regions that are at distances greater than half the specimen thickness from the crack. For bimaterials there is a large three dimensional zone ahead of the crack; behind the crack, plane stress conditions exist beyond approximately one half the specimen thickness from the interface. For the current specimen geometry the 3-D stress fields have not been analyzed. However, it is expected that there are large regions of the specimen in which plane stress conditions exist. For such conditions, σ_{33} is zero, and Eq. 5.2.9 simplifies to

$$S(x_1, x_2) = 2hc_\sigma[\hat{\sigma}_{11}(x_1, x_2) + \hat{\sigma}_{22}(x_1, x_2)] \,, \tag{5.2.10}$$

where $\hat{\sigma}_{11}$ and $\hat{\sigma}_{22}$ are the thickness averages of the in-plane stress components in the plate. Now the conditions for optical interference are related to the thickness averaged in-plane pressure $(\hat{\sigma}_{11}(x_1, x_2) + \hat{\sigma}_{22}(x_1, x_2))$ as follows:

$$\begin{aligned} c_\sigma h \frac{\partial(\hat{\sigma}_{11}(x_1, x_2) + \hat{\sigma}_{22}(x_1, x_2))}{\partial x_1} &= \frac{mp}{\Delta} \,, \qquad m = 0 \pm 1, \pm 2, \ldots \\ c_\sigma h \frac{\partial(\hat{\sigma}_{11}(x_1, x_2) + \hat{\sigma}_{22}(x_1, x_2))}{\partial x_2} &= \frac{np}{\Delta} \,, \qquad n = 0 \pm 1, \pm 2, \ldots \,. \end{aligned} \tag{5.2.11}$$

Figure 5.2.4 is a photograph taken by Tippur and Rosakis (1991). The photograph contains CGS interference fringes caused by quasi-static three point bend loading of an interfacial crack between PMMA (PolyMethyl Methacralate) and aluminum. The gratings were oriented parallel to the x_1 axis, and thus the shearing is in the x_2 direction. As explained in the discussion above, the fringes are contours of constant gradient (with respect to the x_2 direction) of the thickness averaged in-plane pressure $(\hat{\sigma}_{11}(x_1, x_2) + \hat{\sigma}_{22}(x_1, x_2))$. A

characteristic of these interfacial cracks is the presence of two lobes of fringes. One lobe is ahead of the crack tip and one behind. The point at which the fringes in the two lobes converge is the crack tip. The CGS fringes outside the 3-D zone can be used to determine the 2-D stress intensity factor. Since the adhesive used in bonding the Homalite and aluminum is of finite thickness (albeit small), the model composite is actually a trimaterial. The work of Gu (1993) has indicated that there were only small differences in phase angle for the macroscopic bimaterial K-field and the trimaterial local near tip K-field.

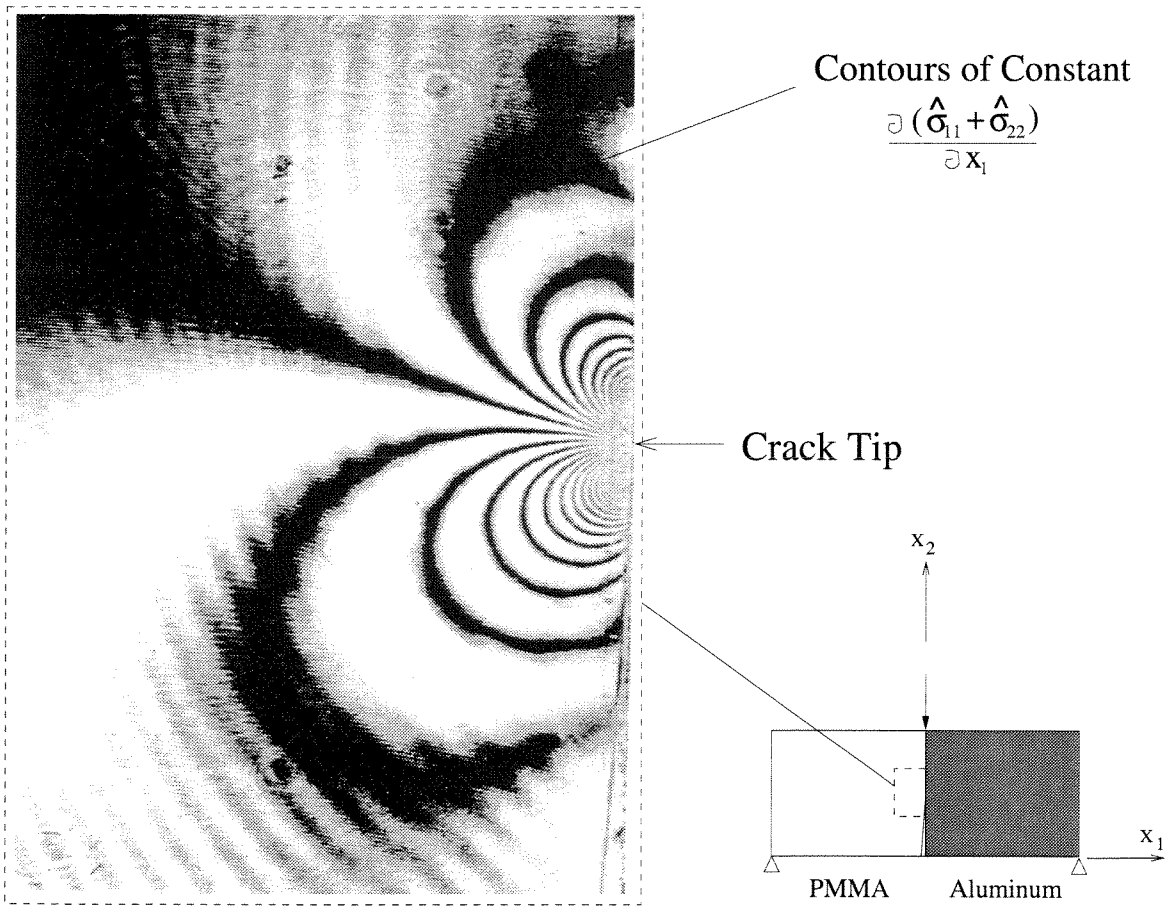

FIG. 5.2.4 CGS fringes from a crack along the interface of PMMA/Aluminum under three point bend loading.

Several limitations with the experimental technique exist. These limitations are characteristic of many different optical techniques used in fracture mechanics. Since the fringes get quite dense near the crack tip (due to high deformations/stresses), it becomes difficult

to locate the crack tip exactly. Additional difficulties result from the formation of shadow spots. The formation of this spot is illustrated by Fig. 5.2.5. Because of the large deformations near the crack tip, the originally collimated laser beam obtains large angular deviation during refraction. Since the optics (gratings and lenses) are of finite dimension, some of these rays are not collected at the image plane and a shadow spot results. A similar effect can be caused by poor focusing of the optics. The shadow spot, usually called a "caustic," is actually used to gather information for the optical method of caustics. However, in the present study it is undesirable.

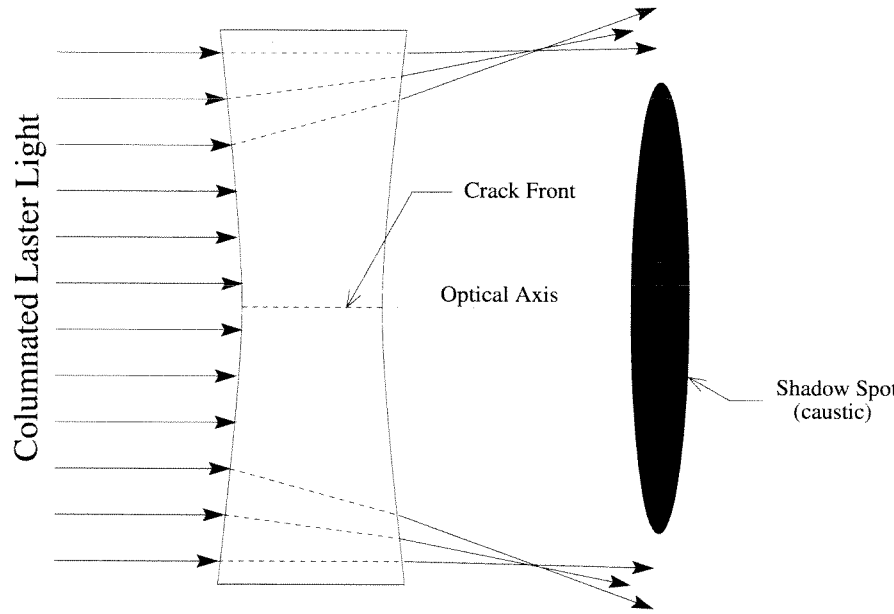

FIG. 5.2.5 A schematic of the profile of rays transmitted through a highly deformed (cracked) specimen.

5.3 Results

The axial response of the model composite for two different strain rates is shown in Figures 5.3.1 and 5.3.2. The stress was calculated from load and original cross sectional area, and the strain was determined from crosshead displacement and original gauge section

length. The strain was calculated over the whole gauge length to avoid ambiguities with the formation of cracks in the Homalite. Unfortunately, by relying on crosshead displacement, compliances in the grip-train were present. The grip-train compliances (particularly those associated with the wedge-gripping) presumably result in the bi-linear response seen in both Figures 5.3.1 and 5.3.2. After the bi-linear portion, the model composite response is nearly perfectly plastic. Since the CGS fringes were video taped during the experiments, it was possible to determine the points at which matrix cracking and debonding began. These points are indicated in the figures. For the higher rate experiment shown in Fig. 5.3.1, the center crack dynamically propagated at a relatively low stress. At the higher rate, neither the center crack propagation nor the debond propagation effected the axial response. Only at much later loading stages did cracks in the Homalite influence the axial response. The lower rate axial response in Fig. 5.3.2 is effected by the (dynamic) center crack propagation. The propagation of Homalite cracks causes a sharp drop in load carrying capability followed by a gradual recovery.

The aluminum "reinforcement" was tested independently and found to have a nearly elastic-perfectly plastic response. The same nonlinearities in the elastic regions of Figures 5.3.1 and 5.3.2 were present in the monolithic aluminum experiments and, as was mentioned above, are most likely related to specimen gripping. The axial response of the composite was dominated by the aluminum. This is not unexpected since the Homalite has a relatively low modulus and low strength. Experiments with only Homalite strips were also performed. Within a range of crosshead displacement rates (0.12–0.005 mm/s) the Homalite was found to be mildly strain rate sensitive with a slight increase in Young's modulus under higher rates of loading. It is not known how strength is effected by strain rate since for the brittle Homalite, the ultimate failure strength is most likely statistical in nature. Additional experiments were performed with monolithic Homalite strips in which the initial hole and wing-tip cracks were present. Since the initial flaw is again of a statistical nature, no conclusions regarding the effect of strain rate on crack propagation in Homalite

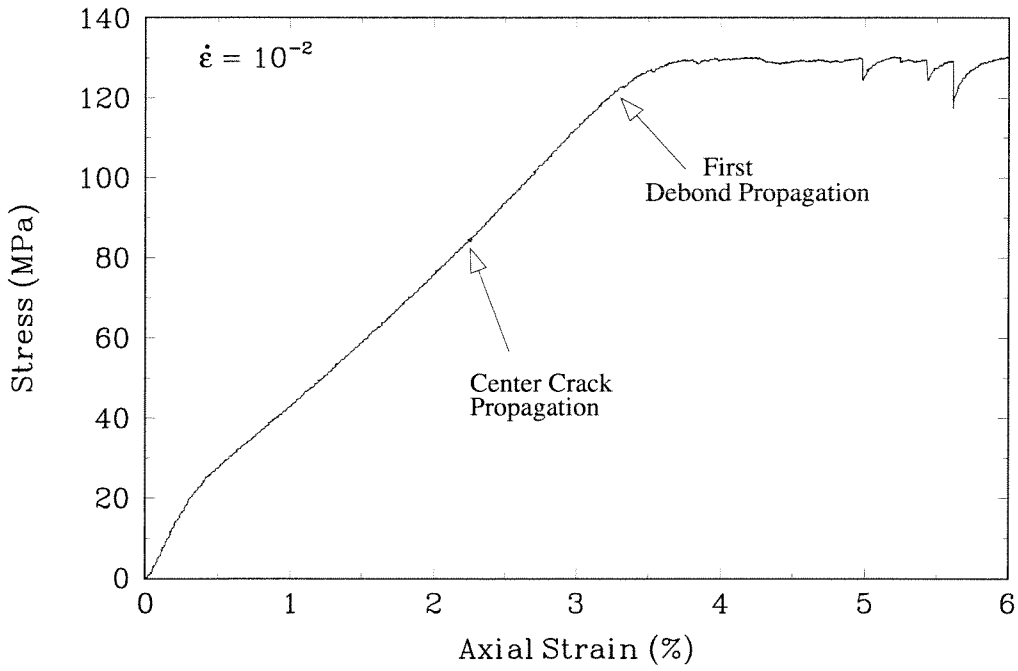

FIG. 5.3.1 The axial stress versus strain for a model composite during higher strain rate loading.

could be drawn. During experiments with the model composites, the propagation of the initial flaw did not correlate with strain rate or stress.

In Fig. 5.3.3 the transverse strain which was determined from the LVDT signal is plotted versus the axial load for the higher strain rate experiment shown in Fig. 5.3.1. Again, the cracking events are indicated on the figure. Although the aluminum appears to dominated the response, it is seen that the cracking events (in particular, the debonds) influence the transverse strain. The stepped response in the transverse strain is a result of the delayed cracks in the Homalite.

For each of a higher and lower strain rate experiment, four video frames of the CGS fringes were digitized. The frames were selected to illustrate the stress fields just before or after a cracking event (matrix cracking or debonding).

The results for a lower rate experiment are shown in Fig. 5.3.4. The digitized frames ranged in time (actual experiment time) between 7:55 and 10:15 minutes. The shearing for this experiment is in the horizontal direction (*i.e.*, the grating lines are parallel to the

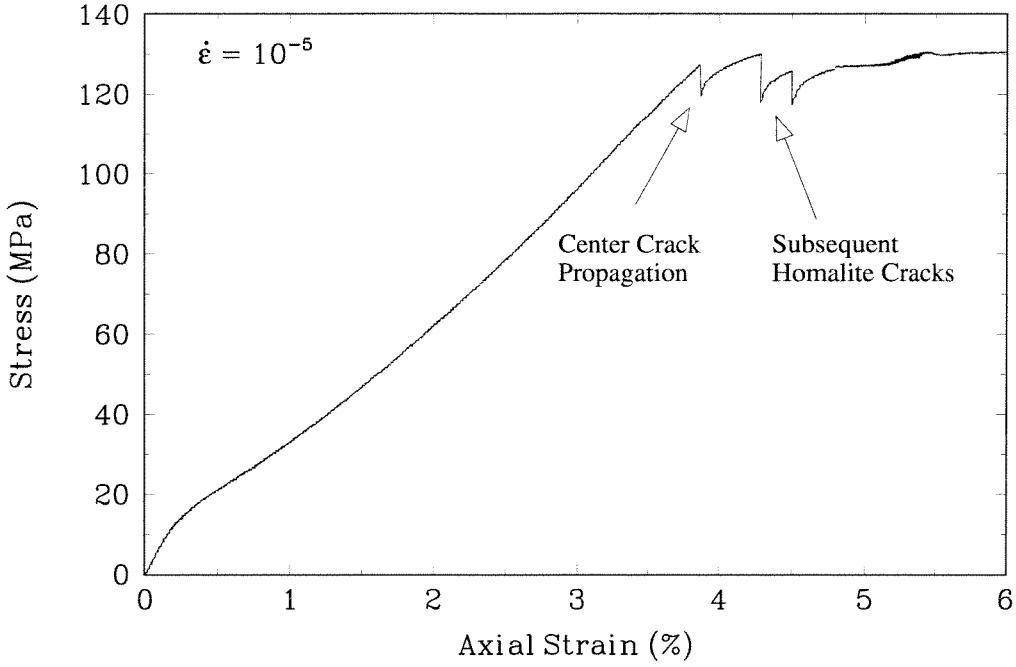

FIG. 5.3.2 The axial stress versus strain for a model composite during lower strain rate loading.

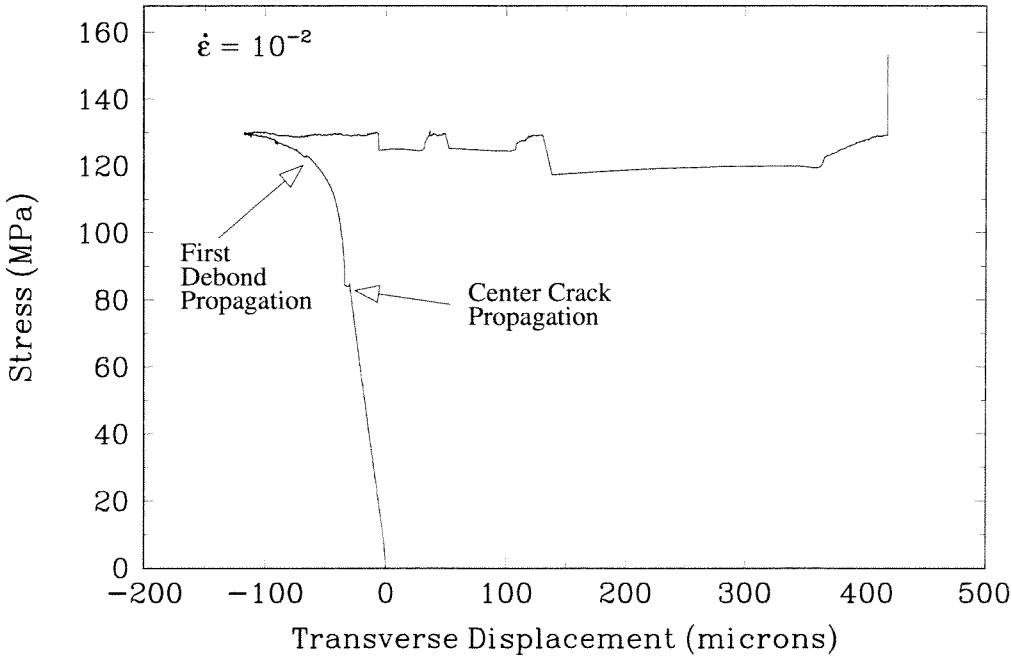

FIG. 5.3.3 The axial stress versus transverse strain for a model composite during higher strain rate loading.

aluminum reinforcement). The first frame, digitized at time t=7:55, shows the fringe pattern for a hole in a homogeneous material. Both the wing cracks and the reinforcements have little influence on the stress field at this stage of the loading. The dark line across the center of the image is the shadow from the LVDT probe. The "double" image of the aluminum is due to the fact that the shearing is in the horizontal direction. The second frame (t=8:05) is just after the center crack has propagated. There were no video frames which captured the crack during propagation, and therefore the crack propagates dynamically in less than $^1/_{30}$ of a second (the time between video frames). The fringe pattern is symmetric showing that the crack propagation was also symmetric. The fringe pattern reflects the fact that the center crack is now stress free. The Homalite away from the central crack is loaded by stress transfer from the aluminum reinforcements. This loading is enough to cause further matrix cracks. In the lower portion of the third frame (t=8:50), a crack has propagated through the Homalite. This crack propagated dynamically, between frames and also bifurcated. No crack propagation along the interface (debonding) was observed between frames 2 and 3. Although the Homalite is now cracked in the center and the bottom of the image, there are still CGS fringes throughout these regions. This is because there are still gradients of stress (recall that the CGS technique forms fringes for constant stress *gradients*). Notice that the pattern in the upper half of the image is quite similar to the image in frame 2. The fourth frame (t=10:15) was digitized just after another matrix crack propagated dynamically (near the top of the image). As was the case for the other frames, up until this point, no debonding was observed. At much later stages of the test (>15:00), small debonds were observed to propagate short distances from the matrix cracks. In summary, for the lower strain rate experiments, it was observed that the model composites tended to form matrix cracks perpendicular to the aluminum reinforcement with minimal debonding of the Homalite-aluminum interface only in the very late stages of loading.

Four frames of a higher strain rate experiment are shown in Fig. 5.3.5. These frames range in time between 0:16 and 0:25 minutes. For this experiment the shearing is in the

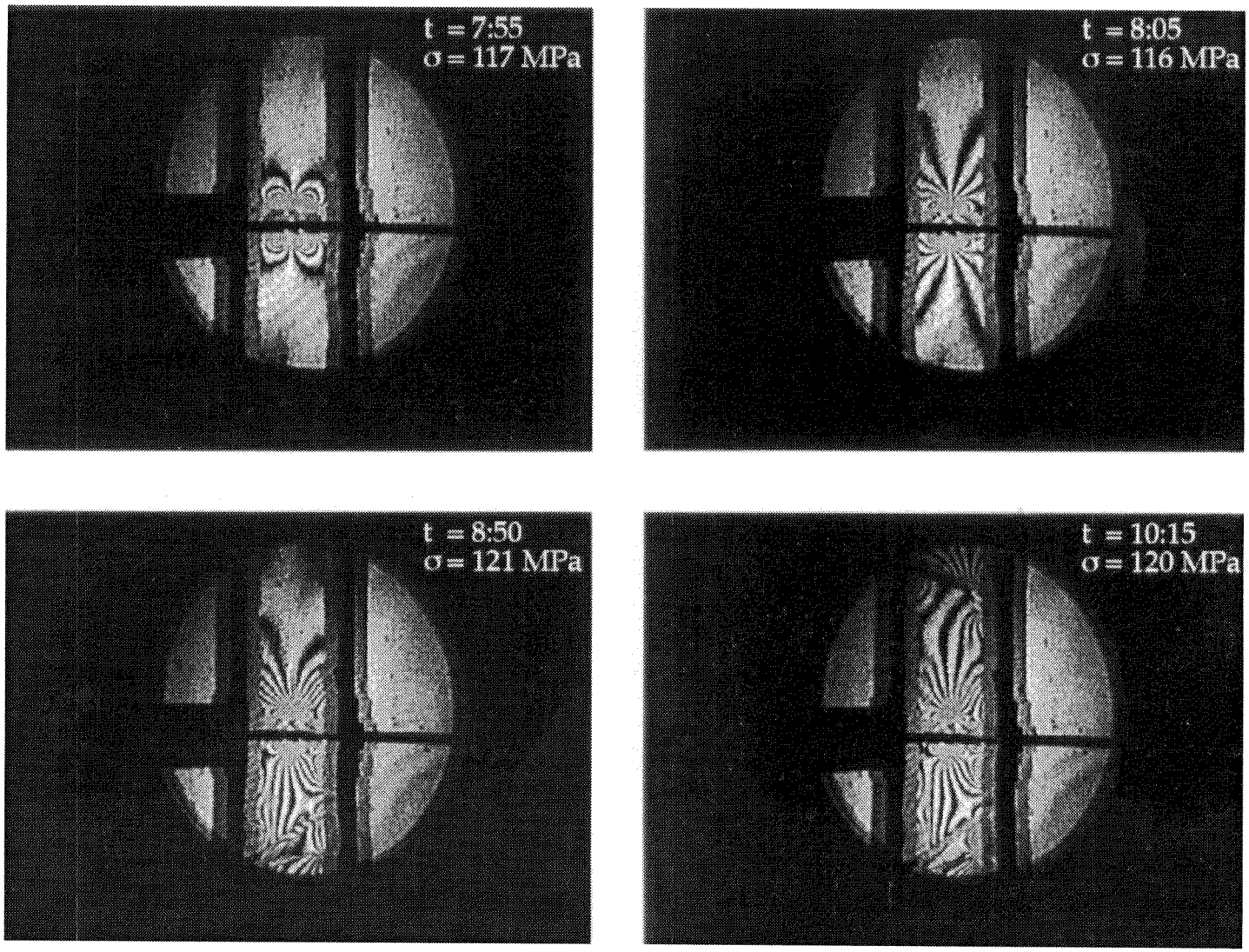

FIG. 5.3.4 Four frames from the video taped CGS fringes formed during a lower (10^{-5} s^{-1}) strain rate model composite experiment.

vertical direction. Therefore, in contrast to Fig. 5.3.4, there are two shadows (or one sheared shadow) of the LVDT probe. Also as a consequence of the different shear direction, the fringes seen in frame 1 (t=0:16) are quite different from those in Fig. 5.3.4; nonetheless, they are representative of a hole in a homogeneous specimen. The advantage to vertical shearing is that the interface is now distinct and debond cracks are more easily visualized. In frame 2 (t=0:17) the center crack has dynamically propagated. On the left side of the crack there are additional fringes which show that the interface on this side of the specimen may be partially debonded in the vicinity of the center crack. The third frame (t=0:23.5) shows the model composite in the process of debonding. A debond crack is just passing out of the field of view in the first quadrant of the image. Also in this frame, another debond is approximately in the center of the second quadrant of the image. This latter debond is seen to be qualitatively similar to the bimaterial interface crack shown in Fig. 5.2.4. In frame 4 there is a debond crack in the middle of the third quadrant; the debond in the fourth quadrant has moved out of the field of view. All of the debonding events were relatively slow, with each debond taking approximately 1 second to propagate from the center crack to beyond the field of view of the interferometer. For these model experiments, the debonds tended to travel all the way to the grip section of the specimens. Additional matrix cracks occurred in the Homalite at much later loading stages and out of the CGS field of view.

5.4 Discussion of the Rate Dependence

The model experiments described above show strain rate dependence within the quasi-static strain rate regime. This dependence manifests itself in the form of the activation and propagation of different damage mechanisms. For lower loading rates, the Homalite matrix material develops multiple cracks perpendicular to the aluminum reinforcement. These cracks all propagate dynamically. Debonding follows only much later in the experiment. For higher loading rates, propagation of the center (starter) crack occurs and the debonds propagate relatively slowly along the entire gauge section of the specimen. At much later

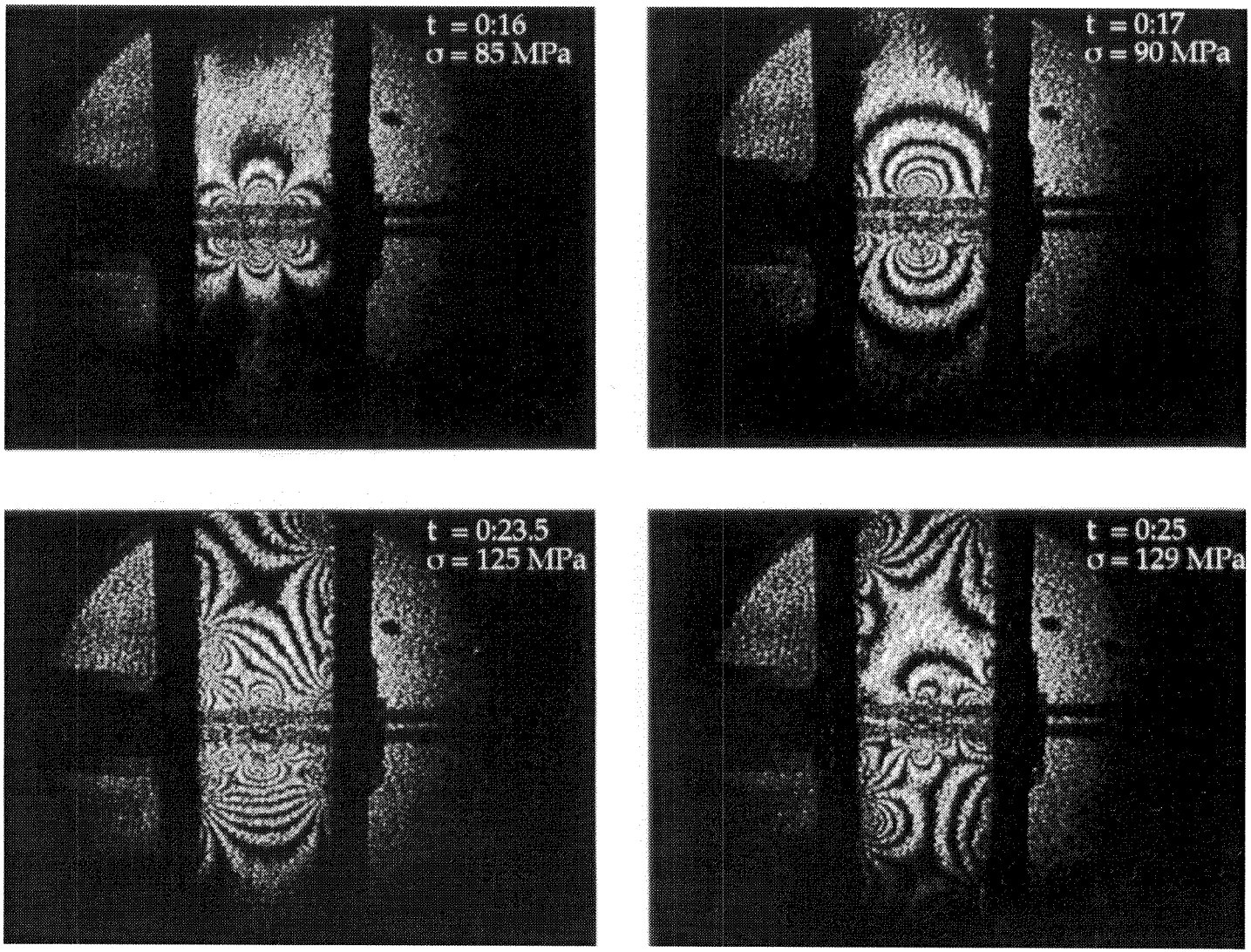

FIG. 5.3.5 Four frames from the video taped CGS fringes formed during a higher (10^{-3} s^{-1}) strain rate model composite experiment.

loading stages, additional cracks develop in the Homalite. Therefore it is seen that the final macroscopic deformation state can be achieved through different damage paths. The damage path appears to be highly dependent on strain rate.

Within the strain rate regime investigated in this work (10^{-5}–10^{-3} s^{-1}) the aluminum is not strain rate dependent. As discussed above, due to the statistical nature of flaws in brittle materials, it is not known to what degree the Homalite is strain rate dependent. It was noticed that, although propagation of the initial center crack did not correlate with the loading rate, there was still correlation between the loading rate and the damage path. Thus it is concluded, that the bulk Homalite properties do not play a dominant role. One could argue that since the interface (primarily Loctite Depend epoxy adhesive) is a viscoelastic material, it may be responsible for the strain rate dependence. In particular, the epoxy interface, like many viscoelastic materials, may become more brittle at higher strain rates. However, given the clamping procedure involved in making the specimens, the interface layer is extremely thin.

The experimental results indicated that it is energetically favorable for debonding of the interface at higher loading rates and for cracking of the Homalite matrix at lower rates. To understand this phenomenon, it may be appropriate to consider the material as a system or a structure in which load is shifted back and forth between the different constituents. The change in macroscopic loading rate may have important ramifications for the rate and sequence of load shedding between the different constituents. Along the same lines, as was discussed in Section 4.4, the dynamics of matrix crack propagation together with the macroscopic loading rate may also effect the activation of different damage mechanisms. In the model experiments there are different length scales associated with the "reinforcement" and "matrix" phases, the interface, and flaws. Inertial effects and wave propagation along with the increased macroscopic loading rate (not allowing equilibration along certain length scales) may play a role in changing the damage mode.

The rate effects observed in the model composite can be compared to the rate effects for the unidirectional SiC/CAS composite presented in Chapter 4. In the model composite, at lower strain rates, periodic matrix cracks developed. A similar response was noted for the SiC/CAS system. It was observed that the SiC/CAS composite modulus degrades more quickly and matrix cracking saturates sooner at lower strain rates. In addition, debonding was not observed in the model composite at lower rates. The analogous effect of reduced debonding at lower loading rates with the SiC/CAS composite is evidenced by the relatively small transverse strain reversal. For higher strain rates, the lack of periodic cracking in the model composite parallels the delayed matrix cracking effect observed in the SiC/CAS composite. Similarly, at higher loading rates, the enhanced debonding observed in the model composite parallels the large transverse strain reversal in the SiC/CAS composite. In the model composite results, the response is dominated by the aluminum reinforcement. Although there is slight variation in the ultimate stress in the SiC/CAS composite for different strain rates, as is the case with the model composite, it appears that the ultimate strength is dominated by the reinforcement phase.

5.5 Summary

In this chapter, the results for experiments with a model composite material were presented. The model material consisted of a Homalite "matrix" and aluminum "reinforcement." This composite specimen was designed to simulate a brittle matrix composite with unidirectional fiber reinforcement. An initial stress concentration in the Homalite was used to control the location and propagation direction of the initial flaw. The optical technique of Coherent Gradient Sensing (CGS) was used to obtain qualitative information regarding the stress fields and to visualize the propagation of cracks (damage). Since the Homalite has a relatively low strain to failure, it was expected that periodic cracks would develop in the Homalite as load was transfered (in shear) from the aluminum. This was found to be true only for low loading rates. For higher rates (but still within the quasi-static strain rate

regime), it was found that the initial starter crack tended to debond the interface and further "matrix" cracks would develop only much later. Possible reasons for this rate dependence (change in damage path with strain rate) were postulated; further work is required for more definitive answers. It was observed that behavior of the model material under different rates of loading is qualitatively similar to response of the SiC/CAS composite under different loading rates. Thus, detailed analysis of the model system may provide insight into the behavior of much more complicated composite systems.

5.6 Future Work with the Model Material

Comparison of the results for the model composite material and the actual ceramic matrix composites provides justification for further experiments and analysis. Ideally, it would be best to develop a material system for which the modulus mismatch between the "matrix" and the "reinforcement" was less. In addition, it would be advantageous if both constituents were optically transparent. The following studies would be worth pursuing:

- Varying the interface strength.
- Varying the initial flaw location and size (including placing the initial flaw along the interface).
- Analysis of the stress fields as given by the CGS fringes.
- "Jump Tests" (see Section 4.4) to determine the source of the rate dependence.

CHAPTER 6

Computational Model

6.1 Introduction

One of the advantages of composites lies in the ability to optimize properties in desired directions. If the composite material properties are well understood and design is done properly, directional optimization can lead to considerable weight savings. Another advantage to composite materials is the relatively high toughness with respect to the individual constituents. Thorough understanding of the constitutive response of composites requires knowledge of the formation and propagation of damage. In particular, it is of interest to obtain the overall material response for cracks which propagate through the matrix material and interact with strong and stiff fibers. In addition, the potential debonding of the fiber is important for the toughening characteristics of the material.

Within the last decade ceramic matrix composites have received considerable attention as a light-weight, high temperature material. There exist many different models for the overall response resulting from the matrix cracking process in ceramic matrix composites; reference was made to several of these models in Chapter 1. As was discussed in Chapter 3, a number of the matrix cracking models are based on fiber-matrix unit cell analysis using shear-lag approximations (*e.g.*, Budiansky *et al.*, 1986; Dharani and Tang, 1990; Danchaivijit and Shetty, 1993). More recently, He *et al.* (1994) have used both a shear-lag analysis and finite element solutions to study the fiber-matrix unit cell. In their numerical model, the matrix crack spacing and debond length were predetermined. It was found that the shear-lag and numerical results differed for small fiber debonds.

The above mentioned shear-lag models primarily study the crack bridging (with fiber debonding) mechanism. Details of crack trapping cannot be determined from such models. Recently extensive study of three-dimensional crack propagation in fiber reinforced brittle matrix composites was performed by Xu *et al.*, (1994). In their investigation, Xu *et al.* studied the overall fracture toughness through numerical simulations of planar and non-planar crack trapping and deflection. It was found that low values of interface toughness resulted in crack deflection and minimal toughening from the crack trapping mechanism. It was postulated, however, that for low interface toughness, the toughness of the composite would be improved through energy dissipation mechanisms associated with bridging effects. In the present investigation the overall behavior of a ceramic matrix composite will be simulated by a numerical model of a fiber-matrix unit cell. The unit cell model will allow for the development of multiple matrix cracks and fiber debonding.

The numerical model developed in the present study is based on a cohesive element formulation similar to that of Needleman (1987). Since this original paper, the cohesive law has been to include shear failure in the cohesive zone (Tvergaard, 1990; Needleman, 1990a,b), and more recently a coupled normal and shear response was developed by Xu and Needleman (1993). All of these cohesive element models have studied plastically deforming materials with interfaces. Ortiz and Suresh (1993) employed cohesive elements in their investigation of intergranular fracture in ceramic materials, and Ungsuwarungsri and Knauss (1987) studied fracture of composites and adhesives. The cohesive element formulation has also been used in a dynamic setting by Camacho and Ortiz (1995) to study impact damage in brittle materials and by Maurisch and Ortiz (1995) to simulate high speed machining. The present formulation closely parallels that of Ortiz and Suresh (1993). However, differences include an axisymmetric formulation, a cohesive law using an uncoupled shear and normal response, and the possibility of frictional sliding after cohesive elements have lost their load carrying capability. In addition, the main results are derived within a dynamic setting with viscous damping included.

A large part of this chapter is devoted to the finite element formulation. A time independent formulation is first presented and the details of how contact and friction were incorporated are described. The finite element simulations for an axisymmetric penny shaped Dugdale crack are compared with the analytical solution. Next the composite unit cell is described and shortcomings of the time independent formulation are discussed. Inertial effects and viscous damping are added in order to obtain converged solutions. The effects of matrix and interface toughness and interface strength parameters are presented. In addition, the interaction of cracks in the matrix with the fiber and the fiber-matrix interface are visualized. The implications of these interactions with respect to debonding of the fiber and subsequent, additional matrix cracks are considered.

6.2 Time Independent Formulation

For standard displacement based finite elements, the time independent form of the principle of virtual work is used as the starting point:

$$\int_{\Omega_o} \mathbf{P} : \nabla \hat{\mathbf{u}} \, \mathrm{d}V_o = \int_{\Omega_o} \mathbf{f} \cdot \hat{\mathbf{u}} \, \mathrm{d}V_o + \int_{\Gamma_o} \mathbf{t} \cdot \hat{\mathbf{u}} \, \mathrm{d}S_o \tag{6.2.1}$$

where Ω_o represents volume integration of the reference configuration, Γ_o is the surface integral of the reference configuration, ∇ is the material gradient, $\hat{\mathbf{u}}$ are the virtual displacements, $\mathbf{P}$ are the first Piola-Kirchhoff stresses, and $\mathbf{f}$ and $\mathbf{t}$ are the body forces and boundary tractions, respectively. Following the notation of Bathe (1982), discretization of Eq. 6.2.1 with finite elements gives the following equilibrium equations:

$$\mathbf{Kd} = \mathbf{R}_b + \mathbf{R}_s - \mathbf{R}_i + \mathbf{R}_c \ , \tag{6.2.2}$$

where $\mathbf{K}$ is the stiffness matrix of the assemblage, $\mathbf{d}$ are the nodal displacements, $\mathbf{R}_b$, $\mathbf{R}_s$, $\mathbf{R}_i$ and $\mathbf{R}_c$ are loads from body forces, element surface forces, element initial stresses and concentrated forces, respectively. Although infinitesimal displacements and strains are assumed, as will be shown in Section 6.2.1, the cohesive element formulation gives a non-linear material (stress-strain) response. In addition, since contact is possible, the changing

boundary condition can also result in non-linearities. For these reasons, it is necessary to iterate to find the equilibrium solution.

The basic problem in non-linear analysis reduces to finding the state of equilibrium of a body under given applied loads. Assuming that external loads are applied as a given function of time, then the equilibrium condition reduces to

$$\mathbf{R}^t - \mathbf{F}^t = 0 \,, \tag{6.2.3}$$

where $\mathbf{R}^t$ represents the external forces (at time t) described in Eq. 6.2.2 and $\mathbf{F}^t$ are the nodal point forces (internal forces) which correspond to the element stresses at time t. Incremental analysis assumes that the solution at time t is known and that the solution for time $t + \Delta t$ is desired. With Δt a suitable time increment, equilibrium requires that

$$\mathbf{R}^{t+\Delta t} - \mathbf{F}^{t+\Delta t} = 0 \,. \tag{6.2.4}$$

Since the solution at time t is known, the following can be written:

$$\mathbf{F}^{t+\Delta t} = \mathbf{F}^t + \mathbf{F} \tag{6.2.5}$$

where $\mathbf{F}$ are the increment in nodal forces corresponding to the increment in element displacements and stresses from time t to time $t + \Delta t$. These incremental forces can be approximated as follows:

$$\mathbf{F} \doteq \mathbf{K}^t \mathbf{d} \,, \tag{6.2.6}$$

where $\mathbf{K}^t$ is a tangent stiffness matrix and $\mathbf{d}$ represents the incremental nodal displacements. If the tangent stiffness matrix is revised with each iteration, the method is referred to as "full Newton-Raphson iteration." There are variants of the stiffness matrix update which are group as "modified" Newton-Raphson iteration. For all the simulations in the present investigation, Full Newton-Raphson Iteration was used. Combining Equations 6.2.6, 6.2.5 and 6.2.4 yields

$$\mathbf{K}^t \mathbf{d} = \mathbf{R}^{t+\Delta t} - \mathbf{F}^t \,, \tag{6.2.7}$$

where **d**, the incremental nodal displacements, are the only unknowns in the system of equations. Using the calculated incremental nodal displacements, the total displacements (solution) at time $t + \Delta t$ can approximated as

$$\mathbf{d}^{t+\Delta t} \doteq \mathbf{d}^t + \mathbf{d} \,, \tag{6.2.8}$$

where $\mathbf{d}^t$ is the known displacement vector at time t. Presumably, one could simply take the solution at $t + \Delta t$ as the correct solution and then restart the iteration process with the next load increment $(t + 2\Delta t)$. However, if non-linearity is severe, because of the approximation in Eq. 6.2.6, it is likely that after only one iteration, increasing the time step and using the approximate solution would incur significant errors and/or be unstable. Thus it is necessary to insure that Eq. 6.2.4 is satisfied before increasing the time step. This can be accomplished by comparing either normalized (usually the square root of the sum of the squares) nodal forces or displacements of the current iteration and the first iteration. If the ratio of normalized forces or displacements for the two iterations is less than a given tolerance, then the solution is assumed to have converged. For the simulations described herein, convergence on nodal displacements was used.

The finite element program used was a modified version of FEAP which was originally programmed by R.L. Taylor at the University of California, Berkeley. The modifications were done by Professor M. Ortiz at Brown University. The simulations described in this chapter were all axisymmetric. Four noded quadrilaterals were used to model the bulk of the mesh. These elements, which will be referred to as "bulk" elements, used linear shape functions and 4 integration (Gaussian quadrature) points. Axisymmetric cohesive elements were used to allow for the initiation and propagation of cracks. In the next two sub-sections, the cohesive elements are described in detail. All elements where thoroughly checked with consistency tests, patch tests (for the bulk elements) and single element simulations. In addition, geometries with known analytical solutions were compared to numerical solutions.

6.2.1 Cohesive Element Formulation

The cohesive elements used in the present investigation have some similarities to the original element developed by Needleman (1987). Similarities include the following: a continuum formulation which assumes the existence of a cohesive zone (Dugdale, 1960; Barenblatt, 1962); surface elements which form an interface between either the boundary or other continuum finite elements; and an interfacial constitutive relation (cohesive law) which specifies the traction across the surface element for given displacement jumps across the element surface.

The formulation for the present cohesive elements closely parallels that of Ortiz and Suresh (1993). Ortiz and Suresh used 6 noded surface elements which had three quadrature points and which could represent quadratic opening displacements. For the current formulation, 4 noded elements with two quadrature points were used. In Fig. 6.2.1 an undeformed and a deformed 4 noded cohesive element are shown. The value of the jump in shear (normal) displacement at each quadrature point was determined using linear shape functions and the relative displacements of nodes tangential (normal) to the surface of the element. Shear (normal) stresses at each quadrature point were calculated from the shear (normal) displacements and the cohesive law. Internal variables at each quadrature point keep track of different stages of the deformation (*e.g.*, undamaged, failed, *etc.*). In this way, it is possible that an element will fail at one quadrature point but not at the other.

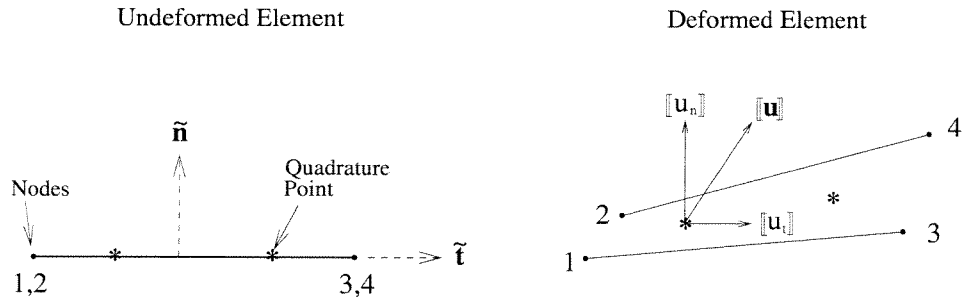

FIG. 6.2.1 A schematic of an undeformed and deformed cohesive element with coordinates and jump displacements indicated.

The cohesive law determines the stress that is transmitted across the element and the energy released by failure. In this respect there are distinct differences between the cohesive law used presently and those used previously. In Needleman (1987,1990a,1990b) the interfacial (cohesive) law was determined from either an exponential or polynomial potential function. Since the cohesive law gives traction as a function of opening displacement, the area under the curve is J/m^2 or work per area. Therefore the shape of the potential was determined by a critical interfacial strength and by the work of separation per unit area. Tvergaard (1990) developed a cohesive law which allowed debonding of a whisker by normal separation as well as by tangential separation. In Xu and Needleman (1993), the interfacial law was determined from a potential that couples the interfacial shear and normal tractions. The normal response of the interface was taken to have the universal exponential form (Universal Binding Energy) presented by Rose *et al.* (1983) for atomistically sharp planes. The shear response had a similar form, but it was symmetric for positive and negative shearing. Despite the attention to atomistics, the formulation was continuum, and it was found that the exact shape of the interfacial law was not important for the final results. The use of a potential for deriving the tractions has the following two distinct advantages: a) it is possible to couple the shear and normal response consistently and b) the work of separation is path independent. In Ungsuwarungsri and Knauss (1987) a formulation with non-linear springs was developed. The springs followed a stress-displacement (q-w) law for which the area under the curve represented the fracture energy. After presenting results for two trapezoidal and two triangular $q(w)$ functions, a procedure was proposed for determining the details of the cohesive law from experiments.

As illustrated in Fig. 6.2.2, in Ortiz and Suresh (1993) the cohesive law was linear in both normal and shearing tractions up until a specified critical stress. The area under the cohesive law curve is the critical energy release rate ($\mathcal{G}_c$). By specifying the critical stress and critical energy release rate, the cohesive law was completely determined. Other,

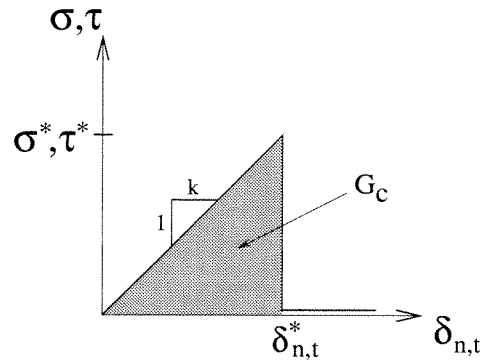

FIG. 6.2.2 Cohesive law for normal displacement jumps from Ortiz and Suresh (1993).

interfacial laws have been proposed that are more complex. For example, in Xu *et al.* (1995), tension-shear coupling is accounted for through an atomic level interlayer potential.

For the present simulations it was desired for the cohesive elements to be transparent (*i.e.*, transmit 100% of the load and not to add to the deformation of the body) until the critical stress was reached. In terms of Fig. 6.2.2, this is equivalent to using a very large initial stiffness (k) for the cohesive elements. However, in order to specify a reasonable critical stress and critical energy release rate, it was decided that the cohesive law should be box shaped. This is similar to the Dugdale-Barenblatt formulation with constant stress in the cohesive zone. The resulting normal and shear cohesive laws are shown in Fig. 6.2.3. The variable s denotes displacement jumps in the tangential direction and g refers to displacement jumps in the normal direction; σ and τ are the corresponding shear and normal cohesive stresses. Note that the shear law is anti-symmetric about the ordinate, and for negative g, contact is approximated by large compressive stresses. A similar concept was used in Camacho and Ortiz (1995), where instead of a box shaped law, a triangular cohesive law was followed with the stress ramped down linearly from a critical stress as a function of the jump in displacement.

As was previously mentioned, an internal variable was used to keep track of where each quadrature point was in terms of the shear and normal cohesive laws. The internal variable was updated after a converged (equilibrium) solution was found. The terminology used is "undamaged" for points along the initial linear slope; "yielding" for points along the

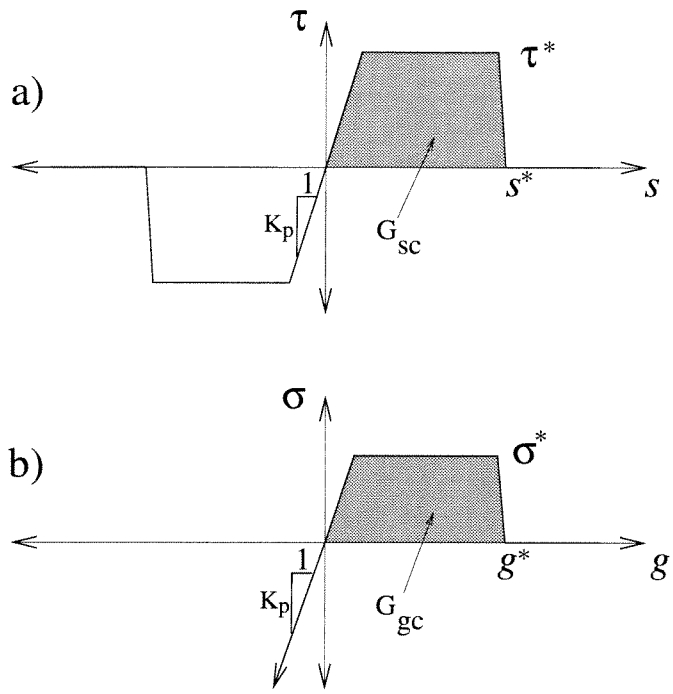

FIG. 6.2.3 The cohesive laws for a) shear displacement and b) normal displacement.

top of the cohesive law box; and "failed" for points beyond the cohesive law box (beyond the critical displacements). The cohesive law for yielding and failed elements has a small (10^{-7}), but finite slope, to avoid numerical difficulties. The normal and shear responses are uncoupled and any quadrature point may be yielding in tension and undamaged in shear, or *vice versa*. Naturally, quadrature points may also be both undamaged or both yielding. If the direction of displacement reverses while a quadrature point is either undamaged or yielding, the cohesive law curve is still followed, albeit in the opposite direction. Once a quadrature point has failed in either tension or shear, then the stresses calculated at that quadrature point reflect the condition that tension cannot not be supported; compressive stresses are possible with approximation of contact described above. As will be described in Section 6.2.2, elements with failed quadrature points will only transmit shear stress when there is friction. Schematics of the cohesive laws for failed quadrature points are shown in

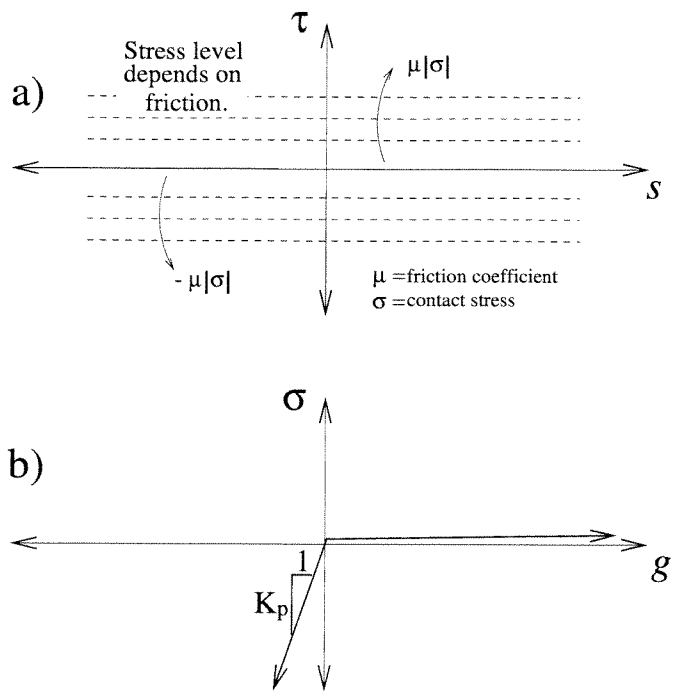

FIG. 6.2.4 The a) shear and b) normal cohesive laws for failed quadrature points.

Fig. 6.2.4. The possible paths to failure (with exaggerated yielding zones) are visualized in stress space in Fig. 6.2.5.

There are two remaining aspects of the cohesive elements which merit discussion. For a cracked body under load, the cohesive zone model allows for the calculation of a cohesive (or plastic) zone size. This calculation can be done in terms of the far-field stresses and the cohesive (or critical) stress (see Eq. 6.2.26). Alternatively, a zone size can be written in terms of the far-field stresses, critical energy release rate and Lamé constants. For plane stress the relation is as follows:

$$r_p = \frac{\pi E}{8(1-\nu^2)} \frac{\mathcal{G}_c}{\sigma_o^2} . \tag{6.2.9}$$

For a valid simulation, it is necessary that for the specified material properties, several cohesive elements span the cohesive zone (*i.e.*, cohesive elements are smaller than the plastic zone size).

The stresses for the cohesive law presented above are given as a function of opening displacement. The fact that displacements are used in the cohesive law introduces a length

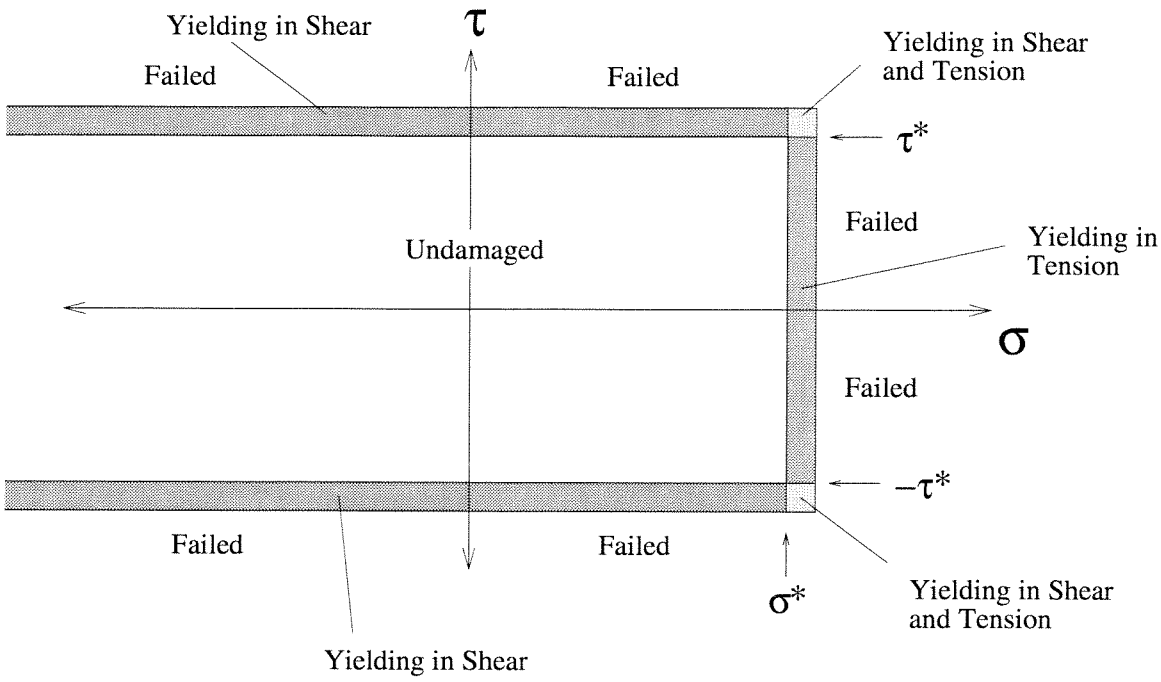

FIG. 6.2.5 An illustration of the failure surface for cohesive elements (with exaggerated yielding) in stress space.

scale into the problem. In discussion by Needleman (1987), the length scale, called the "characteristic length" was related to opening (or sliding) displacement of the cohesive element at which point the element no longer carries load (*i.e.*, g^* or s^* in Fig. 6.2.3). Furthermore, the ratio between the characteristic length and the radius of an inclusion determined whether the decohesion of the inclusion proceeded in a "ductile" or "brittle" manner. In other words, the characteristic length to inclusion radius ratio influenced the toughness ($\mathcal{G}_c$) of the material. However, in Needleman (1990a) it was noted that for large specimen dimensions with respect to the characteristic length, the mesh dimensions do not effect the results. This problem can be visualized with a single bulk and single cohesive element subjected to uniaxial tension. The overall strain at failure is written as

$$\epsilon_f = \frac{\sigma_o}{E} + \frac{\mathcal{G}_c}{\sigma_o L} \,. \tag{6.2.10}$$

where σ_o is the critical stress in the cohesive element and L is the length of the bulk element. Clearly, the length of the bulk element will effect the results when $L\sigma_o$ is the same order of magnitude as $\mathcal{G}_c$. It is important to choose dimensions to avoid this problem.

6.2.2 Friction Formulation

As has been discussed, when the opening displacement of a cohesive element is greater than g^* and/or the sliding displacement is greater than $|s^*|$ the cohesive element is assumed to have failed. In this situation, as illustrated in Fig. 6.2.4, the element no longer can transmit tensile stresses. When there is contact (compressive normal stress), it is realistic that shear loads could be carried through friction. Thus, for failed cohesive elements, a Coulomb friction formulation is added.

The friction formulation (Ortiz, 1995) summarized below is analogous to non-associative plasticity, and is described in detail in Giannakopoulos (1989). Since this is a non-linear problem, the equations are written at step $n+1$ in terms of the current (n) variables. The relevant equations are as follows:

$$\begin{aligned} \sigma_{n+1} &= \sigma_n + E(g_{n+1} + g_n) \\ \tau^f_{n+1} &= \tau^f_n + E(s_{n+1} + s_n) - E\Delta\lambda \operatorname{sgn}(\tau^f_{n+1}) \end{aligned} \tag{6.2.11}$$

where sgn(·) is the signum function (sgn(x)=$x/|x|$), E is the predictor modulus (a large number) and $\Delta\lambda$ is the proportional load factor. In addition, there is another relation for Coulomb friction which forms the "Yield Surface,"

$$\left|\tau^f_{n+1}\right| + \mu\sigma_{n+1} = 0\,. \tag{6.2.12}$$

Now, the following equations constitute the "Elastic Predictors:"

$$\begin{aligned} \tilde{\sigma}_{n+1} &= \sigma_n + E(g_{n+1} + g_n) \\ \tilde{\tau}^f_{n+1} &= \tau^f_n + E(s_{n+1} + s_n) \\ \Delta\tilde{\lambda} &= 0\,. \end{aligned} \tag{6.2.13}$$

After calculating the stress using Eq. 6.2.13, the predicted stresses are checked to see if one has gone beyond the yield surface. Thus, the following equations determine if the "Yield Condition" has *not* been met:

$$\left|\tilde{\tau}^f_{n+1}\right| + \mu\tilde{\sigma}_{n+1} < 0 \begin{cases} YES, & \tau^f_{n+1} = \tilde{\tau}^f_{n+1} \\ & \sigma_{n+1} = \tilde{\sigma}_{n+1} \\ & \text{exit} \\ NO, & \text{"Plastic Corrector"} \end{cases} \tag{6.2.14}$$

As indicated in Eq. 6.2.14, if the yield condition is violated, then the "plastic corrector" must be applied. In other words, the stresses are adjusted through the following equations to lie on the yield surface:

$$\sigma_{n+1} = \tilde{\sigma}_{n+1} \tag{6.2.15a}$$

$$\tau^f_{n+1} = \tilde{\tau}^f_{n+1} - E\Delta\lambda\,\mathrm{sgn}(\tau^f_{n+1}) \tag{6.2.15b}$$

$$\left|\tau^f_{n+1}\right| + \mu\sigma_{n+1} = 0\,. \tag{6.2.16}$$

This method is called the method of "radial return." It is graphically visualized in Fig. 6.2.6 for both three dimensions (friction in the plane) and two dimensions (plane problems with one dimensional sliding).

Now it is left to implement the above formulation for the cohesive elements. The three unknowns ($\Delta\lambda$, σ_{n+1}, and τ^f_{n+1}) are related in Equations 6.2.15a, 6.2.15b and 6.2.16. In what follows, the steps for solving for $\Delta\lambda$ are given. Since the sign of elastic predictor is known, then the sign of the plastic corrector is also known, *i.e.*,

$$\mathrm{sgn}(\tau^f_{n+1}) = \mathrm{sgn}(\tilde{\tau}^f_{n+1})\,. \tag{6.2.17}$$

Therefore, with the definition of the sgn function, it can be written that:

$$\tau^f_{n+1} = \left|\tau^f_{n+1}\right|\,\mathrm{sgn}(\tilde{\tau}^f_{n+1}). \tag{6.2.18}$$

However, Eq. 6.2.18 can be rewritten using both Eq. 6.2.15a and Eq. 6.2.16 as

$$\tau^f_{n+1} = -\mu\tilde{\sigma}_{n+1}\,\mathrm{sgn}(\tilde{\tau}^f_{n+1})\,. \tag{6.2.19}$$

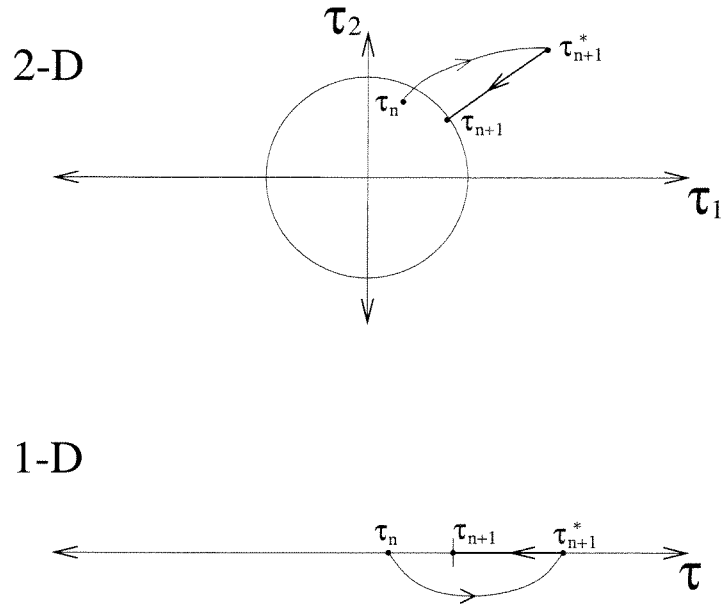

FIG. 6.2.6 The method of "radial return" for correction of frictional stresses in three and two dimensions (2-D or 1-D sliding, respectively).

Substituting Eq. 6.2.19 into Eq. 6.2.15b and using Eq. 6.2.17 gives

$$-\mu\tilde{\sigma}_{n+1}\,\mathrm{sgn}(\tilde{\tau}^f_{n+1}) = \tilde{\tau}^f_{n+1} - E\Delta\lambda\,\mathrm{sgn}(\tau^f_{n+1}). \tag{6.2.20}$$

Noting that $(\mathrm{sgn}(\star))^2 = (\star)$, Eq. 6.2.20 can be further simplified by multiplying both sides by $\mathrm{sgn}(\tilde{\tau}^f_{n+1})$:

$$-\mu\sigma_{n+1} = \tilde{\tau}^f_{n+1}\,\mathrm{sgn}(\tilde{\tau}^f_{n+1}) - E\Delta\lambda\,. \tag{6.2.21}$$

The first term on the right hand side of Eq. 6.2.21 is the absolute value of $\tilde{\tau}^f_{n+1}$, and therefore the solution for $\Delta\lambda$ is

$$\Delta\lambda = \frac{1}{E}\left(\left|\tilde{\tau}^f_{n+1}\right| + \mu\tilde{\sigma}_{n+1}\right)\,. \tag{6.2.22}$$

This quantity is necessarily greater than zero; otherwise the plastic predictor would not have been employed.

With the addition of friction, the tangent stiffness matrix must be accordingly revised. There are three possible situations which can arise:

i. no contact (and hence no resistance to sliding)
ii. contact and insufficient shear stress for sliding (within the yield surface)
iii. contact and frictional sliding (passed the yield surface and corrected)

For each situation, there is a different tangent stiffness. At step $n+1$, the element tangent stiffness matrix, K^e, can be written as follows:

$$K^e = \begin{pmatrix} \frac{\partial \tau^f_{n+1}}{\partial s_{n+1}} & \frac{\partial \sigma_{n+1}}{\partial s_{n+1}} \\ \frac{\partial \tau^f_{n+1}}{\partial g_{n+1}} & \frac{\partial \sigma_{n+1}}{\partial g_{n+1}} \end{pmatrix} . \tag{6.2.23}$$

For case (i), the stresses are zero and hence the gradients are also zero. In actuality, as is the case with the failed cohesive elements described in Section 6.2.1, the diagonal terms of the tangent stiffness matrix are give a very small value ($\approx 10^{-7}$) to avoid numerical difficulties. For case (ii), since the stresses have not exceeded the yield surface, from Eq. 6.2.11, with $\Delta\lambda = 0$, it is seen that the gradients in Eq. 6.2.23 are equal to E along the diagonal and zero off the diagonal. For case (iii), the gradients of the plastic correctors in Eq. 6.2.23 must be calculated. Using Equations 6.2.15b, 6.2.13 and 6.2.22, the plastic corrector stresses can be written as follows:

$$\begin{aligned} \sigma_{n+1} &= \sigma_n + E(g_{n+1} + g_n) \\ \tau^f_{n+1} &= \tau^f_n + E(s_{n+1} + s_n) - \left\{ \left| \tau^f_n + E(s_{n+1} + s_n) \right| + \mu[\sigma_n + E(g_{n+1} + g_n)] \right\} \\ &\qquad \times \operatorname{sgn}(\tau^f_n + E(s_{n+1} + s_n)) . \end{aligned} \tag{6.2.24}$$

Expressions for three of the the partial derivatives in the K^e matrix can be written as

$$\begin{aligned} \frac{\partial \sigma_{n+1}}{\partial s_{n+1}} &= 0 \\ \frac{\partial \sigma_{n+1}}{\partial g_{n+1}} &= E \\ \frac{\partial \tau^f_{n+1}}{\partial s_{n+1}} &= -\mu E \operatorname{sgn}(\tau^f_n + E(s_{n+1} + s_n)) \\ &= -\mu E \operatorname{sgn}(\tilde{\tau}^f_{n+1}) . \end{aligned}$$

The fourth component of Eq. 6.2.23 is calculated after noting that the derivative of an absolute value is the sgn function and that a derivative of the sgn function is a delta function,

$$\frac{\partial \tau^f_{n+1}}{\partial g_{n+1}} = E - \operatorname{sgn}(\tilde{\tau}^f_{n+1})\, E \operatorname{sgn}(\tilde{\tau}^f_{n+1}) - (\left|\tilde{\tau}^f_{n+1}\right| + \mu\tilde{\sigma}_{n+1})\, \delta(\tilde{\tau}^f_{n+1})\, E\ .$$

However, since the plastic corrector is being used, necessarily, $\tilde{\tau}^f_{n+1} \neq 0$, which implies that $\delta(\tilde{\tau}^f_{n+1}) = 0$ and therefore

$$\frac{\partial \tau^f_{n+1}}{\partial g_{n+1}} = 0\ .$$

In summary, the new tangent stiffness matrix for case (iii) is

$$K^e = E \begin{pmatrix} 0 & 0 \\ -\mu \operatorname{sgn}(\tilde{\tau}^f_{n+1}) & 1 \end{pmatrix}\ . \tag{6.2.25}$$

The above Coulomb friction is implemented for failed cohesive elements. The friction formulation is non-linear and thus requires iteration for finding converged solutions. The iteration can be carried in the same way as that for the intact cohesive elements (*i.e.*, Newton-Raphson iteration). Note that since Eq. 6.2.25 is unsymmetric, the global stiffness matrix may also be unsymmetric, and the appropriate matrix solver is required.

6.2.3 An Axisymmetric Dugdale Crack

It was desired to validate the cohesive formulation with a problem that has an analytical solution. It was found that there are solutions to the crack opening displacement (COD) of a Dugdale penny shaped crack in a large cylinder. After giving a brief description of the Dugdale-Barenblatt model, the analytical solution for the COD is described, and finally, the results from the numerical simulations are compared to the analytical solution.

To eliminate the stress singularity at the tip of a crack, the Dugdale-Barenblatt (Dugdale, 1960; Barenblatt, 1962) cohesive zone was formulated. In this model, there is assumed to be a cohesive zone (line), across which the stresses are constant. This is analogous to

having a line of perfectly plastic material at a crack tip. Although in the original model constant stresses were assumed for the cohesive zone, more recently investigations have been done by Ungsuwarungsri and Knauss (1988) for non-constant stresses in the cohesive zone; it was anticipated that microstructural details of the deformation would determine the form of the cohesive stresses. Most of the formulations and analysis of the cohesive zone model have been done for plane problems. For penny shaped cracks the concept is similar; however, the cohesive line is replaced by a cohesive annulus. In Fig. 6.2.7, a cross-section of a large cylinder loaded in the far-field by σ^{∞} and with a penny shaped crack at the origin is sketched. The shaded detail is enlarged on the right-hand side of the figure and stresses at the crack tip are schematically illustrated. The original crack has length a and c is the original crack length *plus* the "yielded" portion of the cohesive zone. The stresses in the region $a < r < c$ are the cohesive stresses denoted by σ_o.

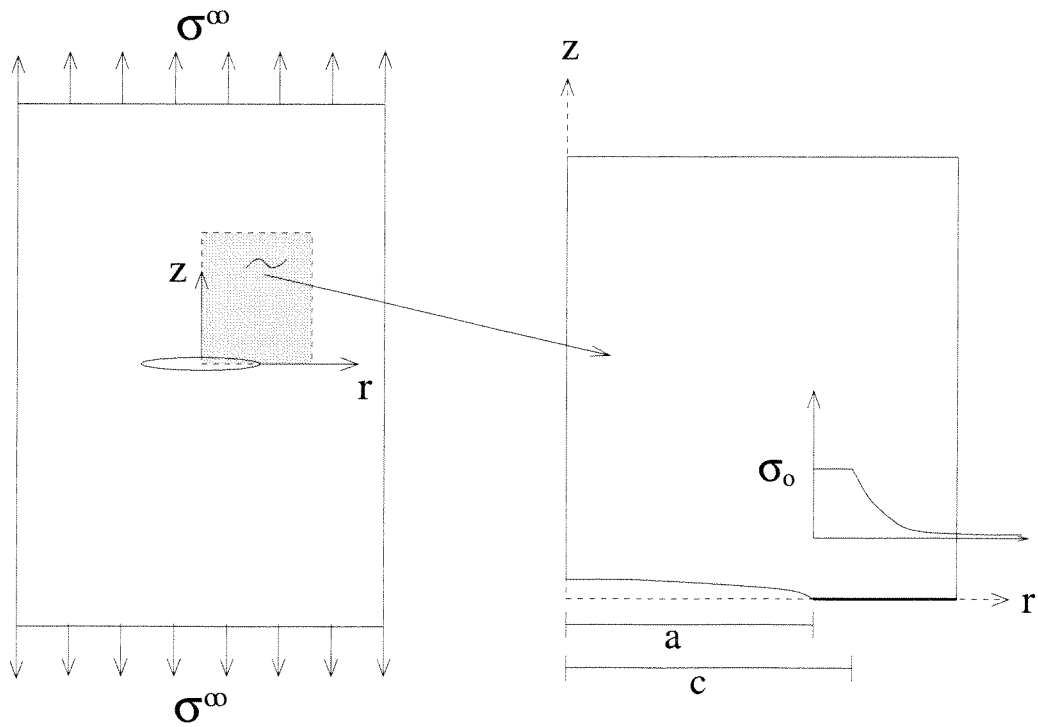

FIG. 6.2.7 A schematic of the problem of a Dugdale penny shaped crack in a cylinder

In order to calculate the crack opening displacements (COD) for a penny shaped Dugdale crack in a cylinder, it is first necessary to determine the size of the cohesive zone as

a function of the far-field and cohesive stress. In terms of the variables defined in Fig. 6.2.7, Tada (1973) provides the following relation:

$$\frac{a}{c} = \sqrt{1 - \left(\frac{\sigma^{\infty}}{\sigma_o}\right)^2} \tag{6.2.26}$$

For calculating the COD, Olesiak and Wnuk (1968) superposed the solutions for the following two problems with a crack in a cylinder: (I) a crack of length c loaded in the far-field and (II) a crack of length c which has tractions (equivalent to the cohesive stresses) applied to the region $a < r < c$. The solution is written for the regions from $0 \leq {}^{\mathrm{r}}/_{\mathrm{c}} < {}^{\mathrm{a}}/_{\mathrm{c}}$ and ${}^{\mathrm{a}}/_{\mathrm{c}} < {}^{\mathrm{r}}/_{\mathrm{c}} < 1$. Integrals of the form

$$\int R(p, s)\mathrm{d}p \,,$$

where s is the square root of a cubic or quadratic polynomial in p, are encountered in the solution. In terms of elliptic integrals the COD solutions are as follows:

$$w(r, z=0) = \pm\frac{4(1-\nu^2)c\sigma_o}{\pi E}\left[\frac{\sigma^{\infty}}{\sigma_o}\sqrt{1-\rho^2} - \sqrt{\frac{1-m^2}{1-\rho^2}} + m\mathrm{E}(\mu_1, \frac{\rho}{m})\right] \qquad 0 \leq \rho < m \tag{6.2.27}$$

$$w(r, z=0) = \pm\frac{4(1-\nu^2)c\sigma_o}{\pi E}\left[\sqrt{1-\rho^2}\left(\frac{\sigma^{\infty}}{\sigma_o} - \frac{1}{\sqrt{1-m^2}}\right) + \frac{m^2-\rho^2}{\rho}\mathrm{F}(\mu_2, \frac{m}{\rho}) + \rho\mathrm{E}(\mu_2, \frac{m}{\rho})\right] \qquad m < \rho < 1 \tag{6.2.28}$$

where $\rho = {}^{\mathrm{r}}/_{\mathrm{c}}$, $m = {}^{\mathrm{a}}/_{\mathrm{c}}$, F and E are elliptic integrals of the first and second kind, respectively, and with

$$\mu_1 = \sin^{-1}\sqrt{\frac{1-m^2}{1-\rho^2}} \qquad \mu_2 = \sin^{-1}\sqrt{\frac{1-\rho^2}{1-m^2}}.$$

The elliptic integrals in the above equations were solved numerically (Press *et al.*, 1992).

The crack opening profiles derived analytically in Eq. 6.2.27 and Eq. 6.2.28 are for constant cohesive stress with infinite critical energy release rate. In other words, the crack only deforms the material and does not propagate through the material. For the finite element simulations the initial slope of the cohesive law (K_p) was picked as large as possible without causing significant ill-conditioning of the global stiffness matrix. Since relevant quantities were normalized, the critical stress (σ_o in the above analytical solution), Young's modulus and Poisson's ratio were arbitrarily set to 0.01, 1.0 and 0.25, respectively. Forces were applied proportionally at the boundary of the mesh to simulate stresses in the far-field. Since this analysis was only to verify that the cohesive elements are formulated consistently, the mesh was not significantly refined. For symmetry reasons, only one quadrant of the cross section of the cylinder needed to be analyzed. Cohesive elements were placed along the r axis at $r > a$, and bulk elements composed the rest of the mesh. The nodes composing the lower half of the cohesive elements were restricted to move only in the radial direction. Displacements were measured at the bulk element nodes originally at $z = 0$. The problem had approximately 3000 degrees of freedom with a mesh with 10 elements in two logarithmic zones in the vertical direction and 75 elements in three logarithmic zones in the horizontal direction. This led to considerable refinement in the crack tip region but not away from the crack tip. For various values of the far-field stress, the COD resulting from the simulations are plotted along with the analytical COD in Fig. 6.2.8. For low far-field stresses the analytical and numerical agreement is excellent. This was not the case for a courser mesh, especially in the region *behind* the crack tip. It is believed that further refinement would improve the agreement for higher far-field stresses. In particular, a radially refined mesh around the crack tip would help significantly. In any case, the similarity between the CODs in the cohesive zone indicates that the method is in good agreement with the Dugdale-Barenblatt cohesive formulation.

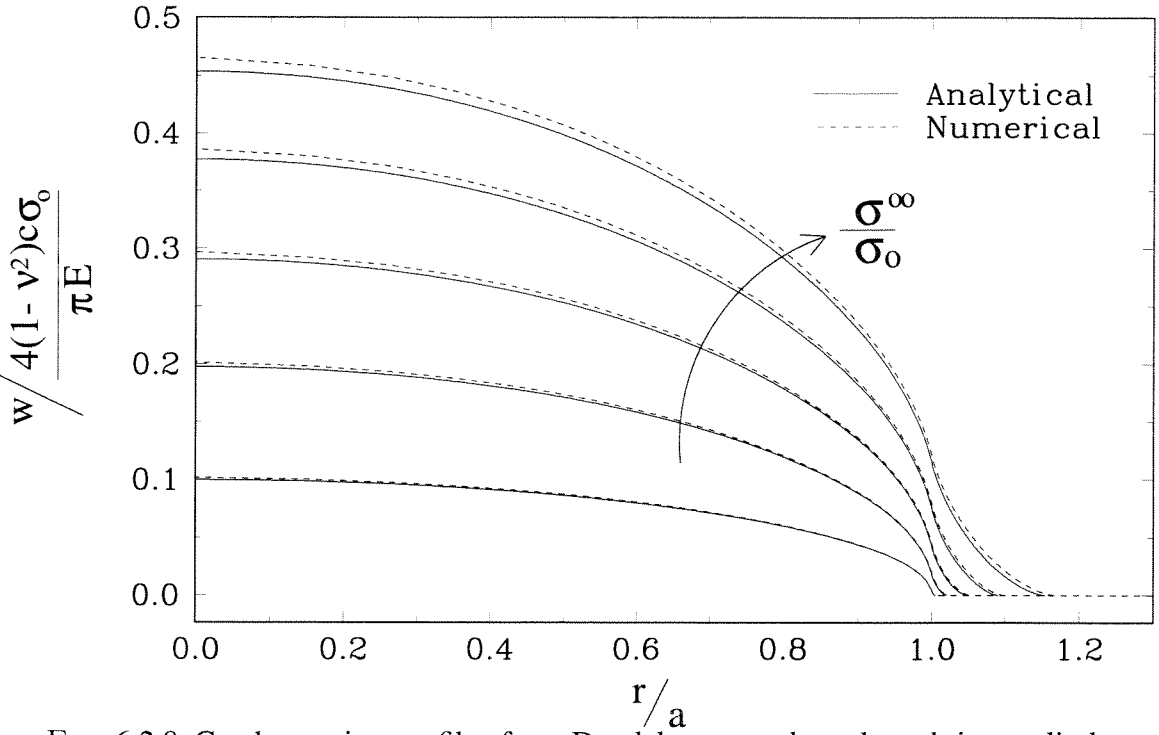

FIG. 6.2.8 Crack opening profiles for a Dugdale penny shaped crack in a cylinder under increasing far-field tension.

6.3 Composite Unit Cell Model

The goal of this numerical investigation is to model the constitutive behavior of a brittle matrix composite which is undergoing damage. Constitutive behavior can be modeled by analyzing a representative element, or unit cell of the material under question. In Fig. 6.3.1 a cross section of a damaged unidirectional fiber composite is sketched. The shaded region in this figure is an axisymmetric unit cell which is a representative volume element of the composite. The full unit cell with all of the elements which are used to discretized it is shown in Fig. 6.3.2. The boundary at the bottom of the cell is restricted to move in the r direction only. Necessarily, the line of nodes along $r = 0$ cannot move in the r direction because of axisymmetry. Displacements are applied to the nodes along the top boundary in the z direction; these nodes are free to move in the r direction. With these boundary conditions, the unit cell represents a repeating unit in the z direction. In order for the unit cell to repeat in the r direction, it is required that the boundary at the outer diameter of

the composite cylinder is restricted to remain straight. This then simulates the condition of having surrounding material constraining the composite cylinder. Although the outer diameter must remain straight, the nodes must be free to move in the z direction, and they must be able to move (albeit simultaneously) in the r direction. The introduction of this restraint is discussed in Section 6.3.1.

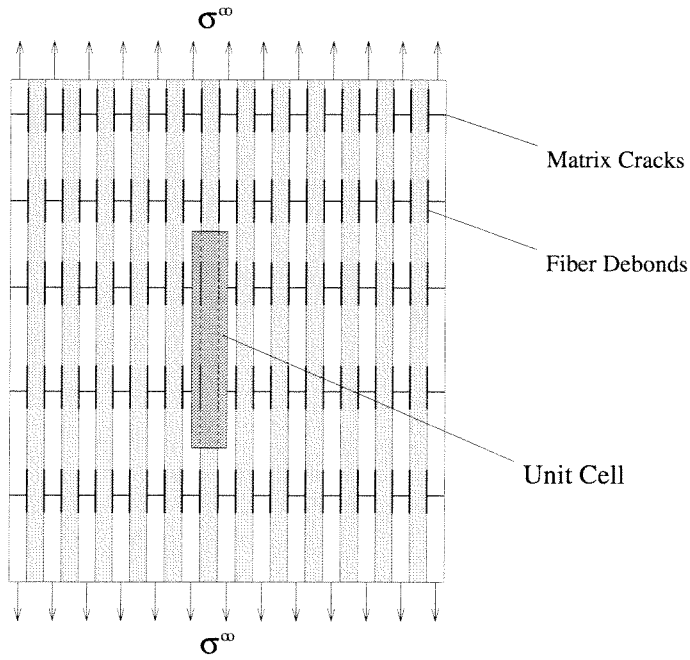

FIG. 6.3.1 A sketch of a damaged fiber composite with the unit cell for numerical simulations indicated.

As was discussed in Chapter 2, damage in a fiber composite material propagates gradually. If the behavior of only one unit cell represents the overall behavior of the composite, then every section of the composite will have the same damage as the unit cell at the same point in the simulation. This does not represent gradual damage. Therefore it is necessary to assume that at a given point in a simulation only a certain percentage of unit cells are active. Although in the present investigation this type of averaging is not applied, during presentation of the results, the implications of averaging will be discussed.

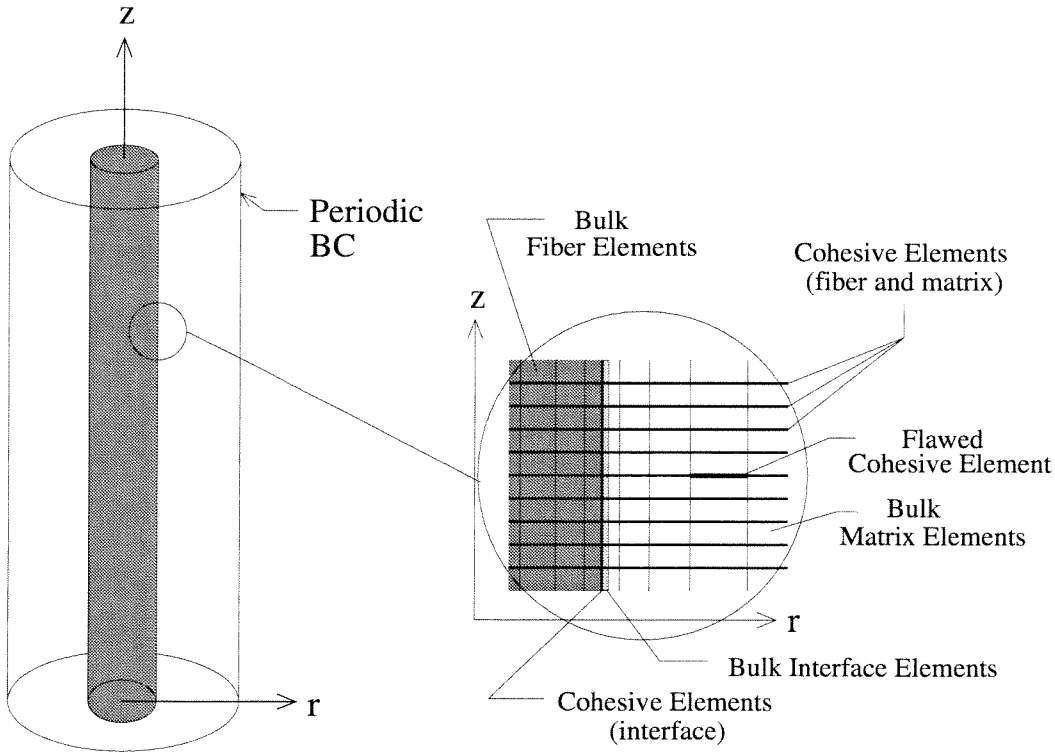

FIG. 6.3.2 Schematic of the discretization of the fiber unit cell.

6.3.1 Penalty Elements

Constraints, such as the one introduced in Section 6.3, are usually introduced by either Lagrange multipliers or the penalty method. The Lagrange multiplier method has the disadvantage that it introduces additional unknowns; whereas the disadvantage of the penalty method is the introduction of large numbers in the global stiffness matrix, thereby causing ill-conditioning. It was chosen to use the penalty method primarily for its simple implementation and also because the global stiffness matrix is already filled with large numbers from the stiff undamaged cohesive elements.

As the name implies, the penalty method works by introducing nodal forces which "penalize" the mesh for non-equal displacements. For the present formulation, a two node element is constructed. Assume that the local displacement (r, z) components for the two nodes of the element are written as (u_1, u_2) and (u_3, u_4), and it is desired that $u_1 = u_3$.

The following equations are assembled into the global equations:

$$\begin{aligned} f_1 &= k(u_1 - u_3) \\ f_3 &= -k(u_1 - u_3), \end{aligned} \tag{6.3.1}$$

where f_1 and f_3 are element nodal forces and k is called the penalty stiffness and is a large number. Thus, for the above constraint, large forces are introduced when u_1 is very different from u_3. The penalty element stiffness matrix which is assembled into the global stiffness matrix,

$$\begin{pmatrix} k & 0 & -k & 0 \\ 0 & 0 & 0 & 0 \\ -k & 0 & k & 0 \\ 0 & 0 & 0 & 0 \end{pmatrix},$$

obviously contains large numbers in the penalty stiffness terms. The largest possible value for k depends on both the other element stiffness values and the specimen dimensions. In the next section, selection of the element material properties, the specimen dimensions and the penalty stiffness are described.

6.3.2 Normalization and Parameter Selection

For the unit cell described above and shown in Fig. 6.3.2, there are three element types and nine material groups. For the time independent formulation, the bulk axisymmetric elements require specifying the material Young's modulus and Poisson's ratio. The cohesive elements need critical energy release rates for the shear and normal direction, critical stresses in the shear and normal direction, a coefficient of friction, an initial stiffnesses (and friction modulus for predicting the friction stress), and a nearly zero stiffness (for the 'deforming' and 'failed' sections of the cohesive law). As has been mentioned above, the penalty elements require a penalty stiffness.

The material that is being modeled was described in detail in Chapter 2. It consists of unidirectional SiC fibers reinforcing a CAS (calcium aluminosilicate) matrix. The fiber radius is approximately 7.5μm, and the volume fraction of fibers is approximately 40%. All dimensions of the unit cell were normalized by the fiber diameter. As determined by

the volume fraction of fibers, the outer diameter of the composite cell is at a radius of 1.58 (normalized by the fiber radius). For the present investigation no bulk interface layer was used; its properties were taken to be the same as the matrix. The moduli of the bulk matrix and fiber elements were all normalized by the initial composite modulus (140 GPa). The Poisson's ratios were 0.299 and 0.222 for the fiber and matrix, respectively. The critical stresses in the normal direction were assumed to be equal to the maximum tensile stresses. Because of the lack of information on the failure of ceramics in shear, critical stresses in the shear direction were taken to be equal to those in the normal direction. Both critical stresses are normalized by the initial composite modulus. To start the cracking process in a controlled fashion, one cohesive element was given a low strength and toughness. It would be even more realistic to assume that there was a statistical distribution of flaws throughout the composite, however, that was not done for the present simulations.

The critical energy release rate in the normal direction was assumed based on typical values in the literature. The critical energy release rate for Nicalon fibers is not accurately known. In addition, it is probable that the microstructure changes from amorphous to crystalline during processing (Cooper, 1994). This would have important implications for the toughness. For the present simulations, since it was not desired to simulate fiber breakage, the fiber normal critical energy release rate was set to 5 kJ/m^2, a value in the upper range of tough monolithic ceramics. The normal critical energy release rate for the matrix was provided in Chapter 3. For the present purposes it is taken to be 0.02 kJ/m^2. For the shear critical energy release rate, in the work of Palaniswamy and Knauss (1978), it was found that experiments fit theory very well for $K_{IIc} = \sqrt{\frac{2}{3}} K_{Ic}$, where K_{IIc} and K_{Ic} are the mode I and mode II critical stress intensity factors, respectively. Thus, in terms of critical energy release rates, the shear energy release rate is taken to be two-thirds of the normal energy release rate. The critical energy release rate has units of J/m^2 $= \mathrm{Pa} \cdot \mathrm{m}$, and is therefore normalized by the composite modulus times the fiber radius. As was discussed in Section 6.2.1, since the ratio of $\mathcal{G}_c$ to $L\sigma_o$ must be small, it was necessary to scale all

$\mathcal{G}_c$ by 10^{-3}. Since this is a parametric study and as long as dimensions related to r_p (see Eq. 6.2.9) are satisfied this is deemed acceptable.

The stiffnesses of the cohesive and penalty elements were chosen to avoid ill-conditioning of the global stiffness matrix. Ill-conditioning is checked for in terms of the loss of significant digits. If more than 7 significant digits (out of 16 double precision digits) were lost, the program execution stopped. Thus, for maximum dimensions of order 1, the maximum cohesive element stiffness and frictional predictor stiffness were approximately 10^7. The penalty stiffness depends on the element size; its maximum value was approximately 10^7 times the smallest element height. The zero stiffness associated with deforming or failed cohesive elements was set to an arbitrary non-zero value of 10^{-7}. The coefficient of friction was set to 0.25, however, for the present simulations, it was not found to have a significant effect.

6.3.3 Shortcomings of the Time Independent Formulation

Simulations were performed with the formulation outlined above. Despite significant reduction in the time step for the Newton-Raphson iteration procedure, convergence was always lost when large numbers of cohesive elements were failing. It is probable that the energy released by the cracking could locally produce the "snap-back" behavior illustrated in Fig. 6.3.3, where λ represents loading forces and u represents displacements. If this is the case, a full or modified Newton-Raphson iteration scheme would not maintain convergence. Methods such as line search and arc-length (see Crisfield, 1983) can often be used to maintain convergence in the presence of severe non-linearities. The line search procedure was not successful in maintaining convergence. A modified arc-length procedure in which the problem was controlled by the node with the highest velocity (Needleman, 1975) was also unsuccessfully implemented. It was anticipated that the convergence problems could be solved by allowing very few cohesive elements to fail during any given time step. It was decided to indirectly enforce this "slow cracking" by adding inertia to the problem. This

is physically realistic since in the presence of rapid cracking, inertial terms are significant. In what follows the addition of time dependent terms to the finite element formulation is discussed.

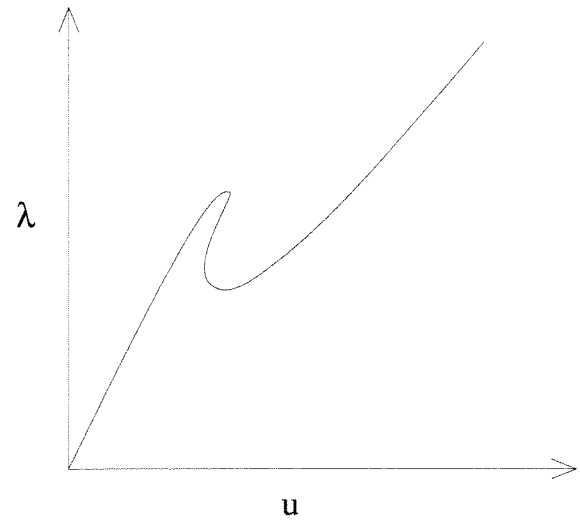

FIG. 6.3.3 A schematic of the "snap-back" behavior which may be locally present during time independent numerical solutions.

6.4 Time Dependant Formulation

As was mentioned above, it appeared that stability was lost when cohesive elements started failing rapidly and strain energy was released. It was necessary to slow the cracking processes. This was accomplished by adding inertial terms, and thereby changing the problem from elastostatic to elastodynamic. In addition, it was decided that viscous damping terms would also be needed. The principle of virtual work with time dependent terms is written at step $n+1$ as follows:

$$\int_{\Omega_o} \mathbf{P}_{n+1} : \nabla \hat{\mathbf{u}} \, \mathrm{d}V_o = \int_{\Omega_o} (\mathbf{f}_{n+1} - \rho \mathbf{a}_{n+1} - \kappa \mathbf{v}_{n+1}) \cdot \hat{\mathbf{u}} \, \mathrm{d}V_o + \int_{\Gamma_o} \mathbf{t}_{n+1} \cdot \hat{\mathbf{u}} \, \mathrm{d}S_o \ , \tag{6.4.1}$$

where ρ is the mass density, $\mathbf{a}_{n+1}$ are the accelerations at step $n+1$, κ is the viscous damping parameter, $\mathbf{v}_{n+1}$ are the velocities at step $n+1$, and all other terms are the same as those described in Eq. 6.2.1. Weak enforcement of equilibrium through Eq. 6.4.1 and subsequent discretization gives the following semi-discrete equations of motion:

$$\mathbf{Ma} + \mathbf{Cv} + \mathbf{Kd} = \mathbf{R}\,, \tag{6.4.2}$$

where **M** is the mass matrix, **C** is the damping matrix, **K** is the tangent stiffness matrix and **R** is the vector of applied forces.

Direct solution of Eq. 6.4.2 can be accomplished using a Newmark Method (Newmark, 1959). The family of equations to be solved are written as

$$\mathbf{Ma}_{n+1} + \mathbf{Cv}_{n+1} + \mathbf{Kd}_{n+1} = \boldsymbol{R}_{n+1} \tag{6.4.3a}$$

$$\mathbf{d}_{n+1} = \mathbf{d}_n + \Delta t\mathbf{v}_n + \Delta t^2[(1/2 - \beta)\mathbf{a}_n + \beta\mathbf{a}_{n+1}] \tag{6.4.3b}$$

$$\mathbf{v}_{n+1} = \mathbf{v}_n + \Delta t[(1-\gamma)\mathbf{a}_n + \gamma\mathbf{a}_{n+1}], \tag{6.4.3c}$$

where Eq. 6.4.3b and Eq. 6.4.3c are finite difference formulas which determine the approximate solution at step $n+1$ given the known approximate solution at step n. The parameters β and γ are the Newmark parameters which determine the stability and accuracy of the algorithm under considerations. Discussion of the selection of (β, γ) will follow shortly.

The Newmark implementation used in the present investigation is known as the "a-form." Following Hughes (1987), the first step of the solution process is to define predictors,

$$\begin{aligned} \tilde{\mathbf{d}}_{n+1} &= \mathbf{d}_n + \Delta t\mathbf{v}_n + \frac{\Delta t^2}{2}(1-2\beta)\mathbf{a}_n \\ \tilde{\mathbf{v}}_{n+1} &= \mathbf{v}_n + \Delta t(1-\gamma)\mathbf{a}_n\,. \end{aligned} \tag{6.4.4}$$

Thus, Eq. 6.4.3b and Eq. 6.4.3c can be rewritten in terms of the predictors as

$$\begin{aligned} \mathbf{d}_{n+1} &= \tilde{\mathbf{d}}_{n+1} + \beta\Delta t^2\mathbf{a}_{n+1} \\ \mathbf{v}_{n+1} &= \tilde{\mathbf{v}}_{n+1} + \gamma\Delta t\mathbf{a}_{n+1}. \end{aligned} \tag{6.4.5}$$

Then, the following recursion relation determines a_{n+1}:

$$(\mathbf{M} + \gamma\Delta t\mathbf{C} + \beta\Delta t^2 K)\mathbf{a}_{n+1} = \mathbf{R}_{n+1} - \mathbf{C}\tilde{\mathbf{v}}_{n+1} - \mathbf{K}\tilde{\mathbf{d}}_{n+1}. \tag{6.4.6}$$

Note that the right-hand side of Eq. 6.4.6 is known. The solution process is begun by specifying $\mathbf{a}_o$ or calculating it from $\mathbf{M}\mathbf{a}_o = \mathbf{R} - \mathbf{C}\mathbf{v}_o - \mathbf{K}\mathbf{d}_o$. Next the recursion relation (Eq. 6.4.6) is used and finally Eq. 6.4.5 are used to calculate the displacements and velocities at step $n + 1$.

Selection of the Newmark parameters, (β, γ), determines the solution method and the stability and accuracy. For the parameters $(1/2, 1/4)$, the method is that of average acceleration (trapezoidal rule); it is implicit, unconditionally stable and of second order accuracy. For parameter selection $(0, 1/2)$, the method is the central difference method, and it is explicit, second order accurate and unconditionally stable for $\Delta t/T \leq \Omega_{\text{crit}}/2\pi = 1/\pi$, where Ω_{crit} is the critical sampling frequency and $T = 2\pi/\omega$ is the period of vibration. For determining the period of vibration, it is necessary to know the maximum natural frequency. Typically the maximum natural frequency is the Rayleigh wave speed divided by the smallest element dimension. Other combinations of (β, γ) can be used. For $2\beta \geq \gamma \geq 1/2$ the scheme is always unconditionally stable. For $\gamma \geq 1/2$ and $\beta < \gamma/2$, the stability is dependent on the critical sampling frequency. For $\gamma \neq 1/2$ the scheme is not second order accurate and numerical (algorithmic) damping is present. For the present simulations, the Newmark parameters are selected for implicit solution and unconditional stability. The cost of solving implicitly is offset by the ability to take larger time steps. In addition, for reasons explained in the next paragraph, numerical damping is also added.

As described by Hughes (1987), higher modes of vibration are induced by the discretization process and are not representative of the partial differential equations. For this reason, it is desirable and/or necessary to add numerical (algorithmic) damping. For the Newmark Method, this is accomplished by choosing $\gamma > 1/2$ and selecting the appropriate β to maximize high frequency dissipation. As given by Hughes (1987), for viscous damp-

ing ratios less than one and $\gamma \geq {}^1/_2$, for unconditional stability, β should be calculated as follows:

$$\beta \geq \frac{(\gamma + {}^1/_2)^2}{4} . \tag{6.4.7}$$

Hughes (1983) shows that viscous damping does not damp the artificial higher modes. Although numerical damping is effective in removing the artificial vibrations, it has the unfortunate side-effect of relegating the scheme to first-order accuracy. For this reason, there has been considerable research into alternative methods of numerical damping (see Hughes, 1987). For the present simulations, despite the loss in accuracy, the "a-form" implementation of the Newmark Method with minimal numerical damping ($\gamma > {}^1/_2$) is employed.

6.4.1 Parameters Revisited

The cohesive and friction formulation described above are implemented in the time dependent scheme without any changes. It is, however, necessary to add mass terms to the bulk elements. As discussed by Hughes (1983), there are a number of different methods for adding mass to the finite element formulation. For the present investigation, mass was incorporated as "consistent mass," which distributes mass throughout the element in the following fashion:

$$\mathbf{M}^e = \int_{\Omega^e} \mathbf{N}^e \rho (\mathbf{N}^e)^T \mathrm{d}\Omega ,$$

where $\mathbf{M}^e$ is the element mass matrix, Ω^e is the element volume, $\mathbf{N}^e$ are the element shape functions and ρ is the density. The density used for the matrix and fiber bulk elements was the real (un-normalized) density for each material (2700 and 2500 ${}^{\mathrm{kg}}/_{\mathrm{m}^3}$, respectively).

As was mentioned above, damping is added both numerically and through viscosity. Both of these parameters were determined in an *ad hoc* fashion. It was found that for both parameters there were choices which led to minimal spurious oscillations with rapid solution. The numerical damping for all results reported herein was set with $\gamma = 0.6$ and (using Eq. 6.4.7) $\beta = 0.3025$, and therefore provides an unconditionally stable algorithm.

Rayleigh damping is a convenient way of calculating the viscous damping matrix, **C**, without altering the solution algorithm. The damping matrix is given as follows:

$$\mathbf{C} = a\mathbf{M} + b\mathbf{K} \, ,$$

where **M** is the mass matrix, **K** is the stiffness matrix, and a and b are two proportionality constants. In terms of the proportionality constants and the undamped frequency of vibration, ω, the damping ratio can be written as (Bathe, 1982)

$$\zeta = \frac{\frac{a}{\omega} + b\omega}{2} \, .$$

Thus, it is seen that the mass proportional damping is primarily effective at lower frequencies and the stiffness proportional term damps the higher frequencies. For the current simulations it was desired to remove high frequency oscillations, and therefore a was set to zero. Since viscous damping is stiffness proportional, it varies with the mesh size.

The primary goal of the present composite unit cell simulations was to obtain quasi-static results, and although inertial effects are included in the formulation, the rate of application of displacements was very low and simulations advanced to large values of time. Within this framework the propagation of waves within the model were not of interest, and thus viscous damping was not studied in detail. At the same time, it was found that for the composite unit cell, the numerical and viscous damping parameters did not alter the point of first cracking (initial drop in the stress-strain curve), but that the details of the crack propagation were changed. For this reason, when making comparisons for computations with different material properties, the numerical and viscous damping parameters were held constant. A secondary goal of the simulations was to observe the rate dependence of the cohesive elements. In this situation the viscous damping is sure to have an important effect on the wave propagation. Every material should have a certain amount of internal damping, however, there is no way to correlate viscous damping with internal damping. The influence of damping parameters will be shown in the results of the one-dimensional dynamic and quasi-static simulations.

6.4.2 One-Dimensional Results

One dimensional simulations were used to study the effects of damping parameters and to verify that cohesive elements performed properly within the time dependent formulation. First, single bulk elements were tested as spring oscillators in the radial and axial directions. The amplitudes and frequencies of vibration were checked with respect to the analytical solutions. Next, a simple mesh consisting of 6 bulk elements along the z axis was constructed. In the middle of this row of bulk elements was a single cohesive element. Displacements were applied linearly with time in the z direction at the top bulk element. In addition, initial velocities equal to the displacement rate were also applied at the top bulk element. Nodes were free to move only in the z direction. Stresses were monitored in the top and bottom elements of the bar.

Relatively high displacement rates ($\dot{u} = 10^{-4}$) were used to illustrate the wave propagation features, including the attenuation of waves by damping. For no damping and minimal numerical damping ($\gamma = 0.6,\ \beta = 0.3025$) the stress versus time curves are plotted in Fig. 6.4.1 for bulk elements at the top and the bottom of the 1-D bar. It is noted that the results with numerical damping are initially nearly identical to those without damping. The "stair-step" increase in stress versus time is a direct consequence of the reflection of waves within the bar, and the drop in the stress-strain curve is the result of failure of the cohesive element. The release wave from the failure causes the two halves of the bar to continue to oscillate. The numerical damping causes the magnitude of these oscillations to gradually decrease with time. The tension spike just before the drop is stress is a consequence of the discrete nature of the problem. For fewer elements the tension spike was more significant, and for smaller elements the frequency of the spike was greater. The tension pulse propagates throughout the body even after it is vibrating freely. Viscous damping was added to the solution and in Fig. 6.4.2, the stress versus time is plotted for a bulk element at the top and the bottom of the 1-D bar. The addition of damping reduces the oscillations and nearly

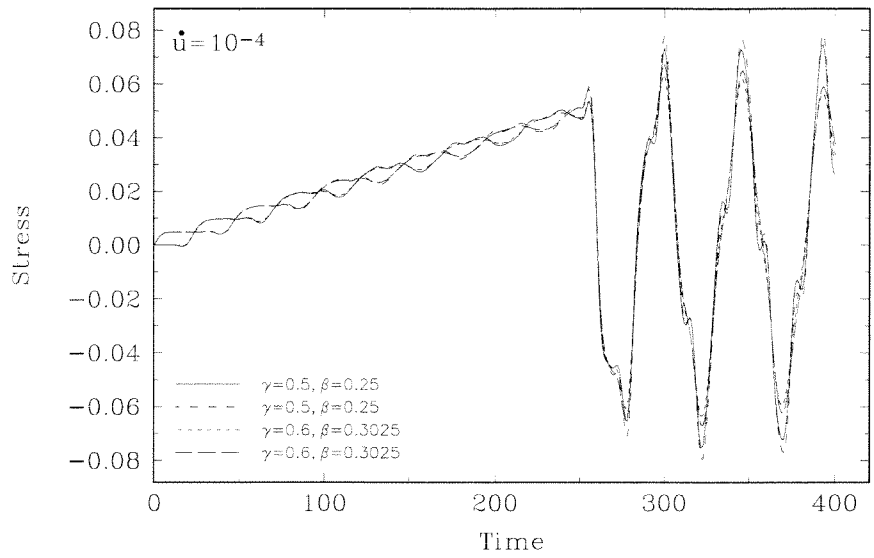

FIG. 6.4.1 Stresses versus time at both ends of a 1-D bar with no damping and with minimal numerical damping, as indicated.

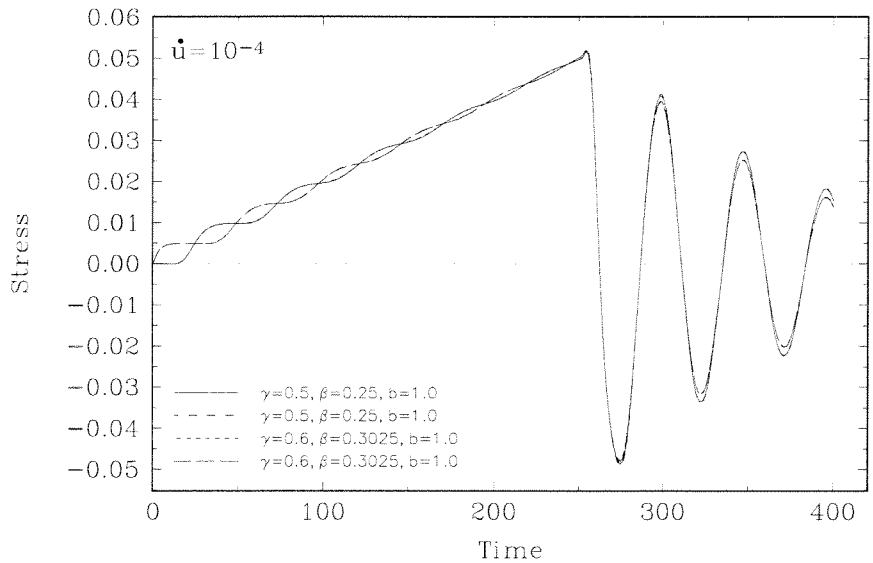

FIG. 6.4.2 Stresses versus time at the top and bottom a 1-D bar with viscous damping and with viscous damping and numerical damping, as indicated.

eliminates the tension spike. As was the case with the data in Fig. 6.4.1, the addition of numerical damping did not significantly alter the viscous damping results.

The 1-D bar geometry was also used to for quasi-static simulations. In Fig. 6.4.3, for reduced time rate of change of the applied displacements ($\dot{u} = 10^{-6}$), the stresses versus time are plotted. To achieve the required stress for failure in a reasonable number

of iterations the time step was increased. In the region before failure no wave propagation effects are seen. The high frequency oscillations after failure are most likely a consequence of the large time step. Although it cannot be seen in Fig. 6.4.3 because the curves overlap, the numerical damping was effective in reducing the high frequency, post-failure oscillations. It is seen that numerical damping has no effect on when the cohesive element fails. Viscous damping effects were similar to the numerical damping effects, and in particular, the point of failure was not altered.

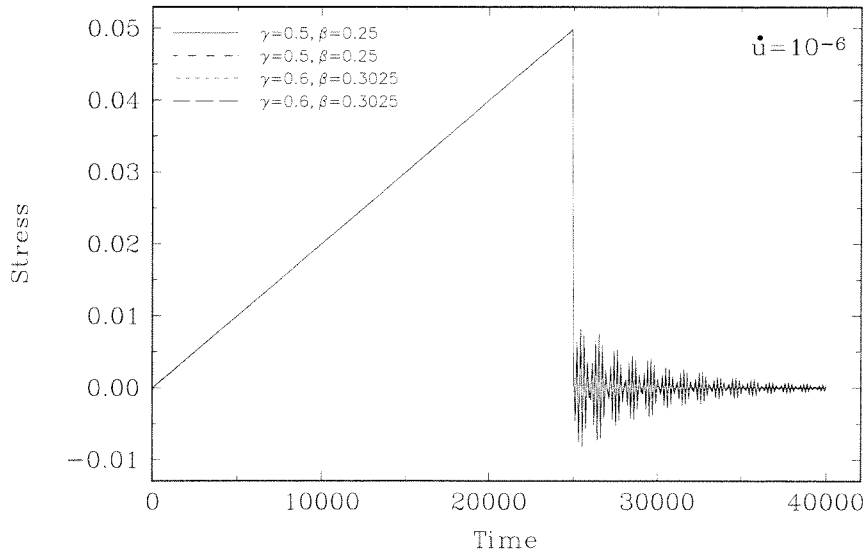

FIG. 6.4.3 Quasi-static stress versus time at the top and bottom a 1-D bar with no damping and with minimal numerical damping.

6.5 Composite Results

Two different mesh heights were investigated for the composite unit cell simulations. In Fig. 6.5.1 the tall mesh is shown. This mesh has approximately 22,000 degrees of freedom. Note that the cohesive elements are not visible since they initially have zero thickness. A shorter mesh, which was one tenth the height of the mesh in Fig. 6.5.1, was used for most of the simulations in this section. The shorter mesh has approximately 3,000 degrees of freedom. For all the simulations presented, the number of horizontal elements was fixed at 36. The elements were logarithmically spaced through the matrix, with the

majority of the elements in the region next to the fiber-matrix interface. Since the cohesive elements are present throughout the mesh, cracks could potentially form at any location. Therefore, it is necessary to have a relatively fine vertical spacing of elements. For a 0.5 (normalized) high mesh, simulations with 10, 20 and 50 elements were performed. It was found that the initial drop in load carrying capability was identical for the two finer meshes. Although, there were slight differences in the transverse (debonding) response for the three different element densities, it was decided to run all simulations with 20 elements per 0.5 unit height.

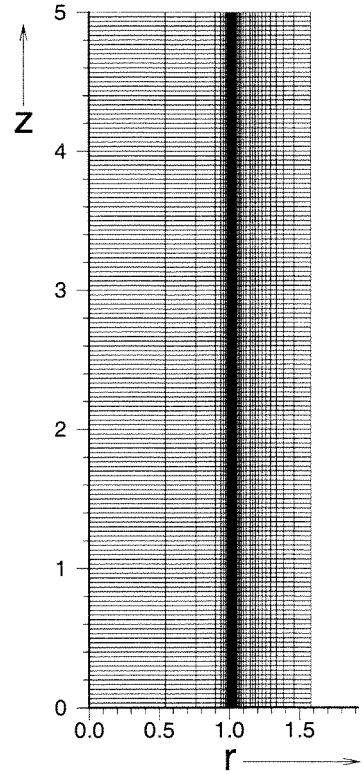

FIG. 6.5.1 A finite element mesh used for simulations of a fiber-matrix unit cell.

The shorter mesh was necessary because of the large number of iterations required for solution made parametric studies with large numbers of elements impractical. To further reduce the total time needed for a complete simulation, a time stepping scheme which automatically varied the time step was implemented. If, after several iterations, convergence was not achieved, restart data was retrieved from memory and the time step was decreased. To ensure accurate solutions, the time step was restricted not to exceed a

given value. The time step ranged quite significantly from large values in elastic regions to very small values when cohesive elements were failing. The shorter mesh was usually deformed to a strain level of 0.07%. For the lower strain rate simulations ($\dot{\epsilon} = 2 \times 10^{-8}$) such strain levels were achieved in anywhere from 700 to 2500 converged time steps, depending on the material properties (sequence of cracking). Each time step required varying numbers of iterations, but on average, for the smaller mesh, 11 seconds of CRAY Y-MP2E/232 CPU time was required for each time step. The larger mesh required on average 125 seconds per time step.

6.5.1 Interface Strength and Toughness

The benefits of properly choosing the interface strength in composites is well known (*e.g.*, Evans and Marshall, 1989). Strong interfaces will cause a matrix crack to propagate through the fiber, while weaker interfaces will allow the matrix crack to debond the fiber. Xu *et al.* (1994) illustrated that strong interfaces enhance toughening by crack trapping, while weaker interfaces increase toughening through debonding and crack bridging.

In Fig. 6.5.2 the axial stress-strain curves for five simulations are shown. As indicated in the figure, the interface for two of the simulations had the same strength and different toughnesses, and the other two simulations had different strengths with fixed toughnesses. A fifth simulation with an even stronger interface is also included in Fig. 6.5.2. After an initially linear stress-strain response, there is a sharp drop in stress followed by another linear portion. For the weakest interface, the sharp drop in stress occurs slightly earlier. For the strongest and toughest interface, the the final linear portion occurs at higher stresses than for the weaker interfaces.

The initial modulus of the stress-strain curve in Fig. 6.5.2 is equivalent to the rule of mixtures modulus, E_c,

$$E_c = c_f E_f + c_m E_m \ , \tag{6.5.1}$$

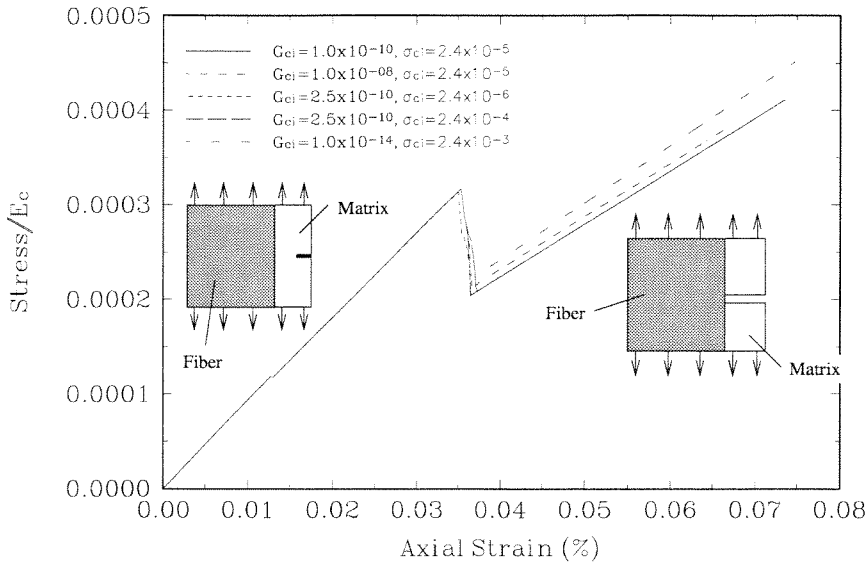

FIG. 6.5.2 Axial stress-strain curves for comparison of interface strength and toughness.

where c_f, c_m and E_f, E_m are volume fractions and Young's moduli of the fiber and the matrix, respectively. The composite modulus E_c is 130 GPa. At a stress of approximately 17.5 MPa, the slight drop in the stress-strain curve is due to the failure of the flawed cohesive element. The sharp drop in the stress-strain behavior at approximately 45 MPa is the result of propagation of the matrix crack. There are many points in the stress-strain curve during this drop, however, the time step is so small, that the increase in displacement is not resolved on the scale of the abscissa in Fig. 6.5.2. Recalling that the simulations are performed in displacement control, it was expected that the ability of the composite to maintain its load carrying capability would be lost as the matrix cracks propagated, and that following propagation of matrix crack, the composite response would be linear and related to only the modulus of the fiber. For a completely debonded interface the magnitude of the drop and the subsequent fiber loading modulus can be verified using the rule of mixtures with c_m equal to zero in Eq. 6.5.1. These situations are indicated schematically in Fig. 6.5.2. For the cases when the interface is not completely debonded, a portion of the matrix is loaded in shear, and thus the matrix continues to help carry load. It is noted that the drop for the stronger interfaces is delayed, possibly due to crack trapping. In the current

simulations, although it is believed that more evidence of crack trapping would result from better selection of parameters, the effects of axisymmetry could also be obscuring the ability of a tough and/or strong interface toughness to inhibit propagation of the matrix crack.

The propagation of the matrix crack leads to a degradation of the composite modulus. The degradation of the composite modulus was observed in the experiments with the fiber reinforced ceramic matrix composite discussed in Chapter 2. However, for the experiments, the modulus degraded gradually since not all matrix crack propagated at the same instant. As was discussed earlier in this chapter, this behavior can be simulated in the numerical model by implementing an averaging scheme which assumes that only a certain percentage of fiber-matrix unit cells are active at a give stage of the simulation. In this way the degradation of the composite modulus would be gradual.

The axial stress versus transverse strain curves for the various interface parameters are shown in Fig. 6.5.3. The properties of the interface have various effects on the transverse strain response. All of the stress-strain curves show reversals in transverse stress which begin at the point of matrix cracking. Since the load is dropping during matrix cracking, the reversal also occurs during the drop in load. For the weakest interface, since the interface has begun to fail when the flawed cohesive element fails, there is additional non-linearity in the transverse strain earlier than for the other simulations. The extent of the reversal depends on whether the interface has completely debonded. For completely debonded interfaces, the transverse strain returns to zero because of the axisymmetry. The oscillations in the transverse strain data are the result of damped vibrations of the annular matrix. Both the toughest and the strongest interfaces do not return to zero because these interfaces have not completely debonded. For the case of the strongest interface which remained intact, it is noted that there is a dual reversal. The initial slope of the transverse strain curve for the uncracked interface is related to the composite Poisson's ratio and the final slope is related to the fiber Poisson's ratio. In the experiments with the fiber reinforced ceramic matrix composite described in Chapter 2 reversals in transverse strain were also observed.

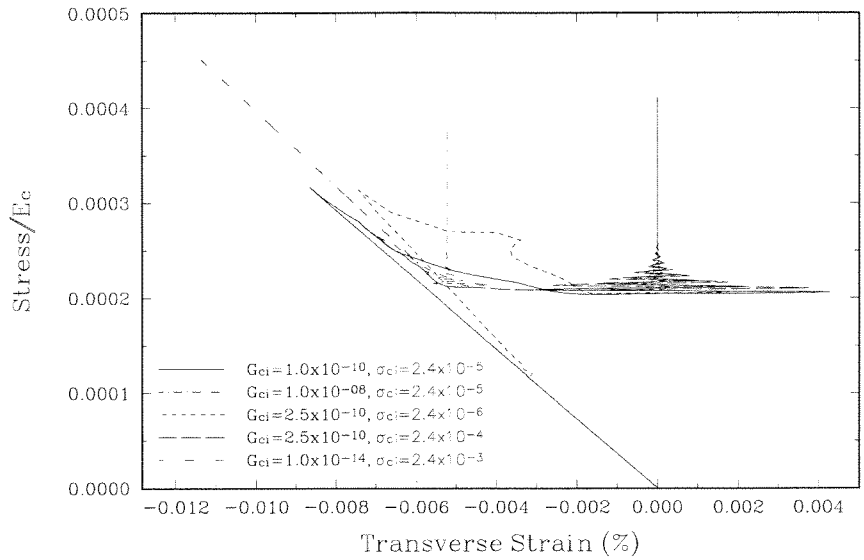

FIG. 6.5.3 The axial stress versus transverse strain curves for the various interface toughnesses and strengths.

In the present simulations the fiber was given a relatively high strength and thus was not permitted to fracture. Nevertheless, in Fig. 6.5.4, the effect of the interface strength is illustrated by a plot of stresses in the fiber for the five different interface properties discussed above. As indicated by the schematic in Fig. 6.5.4, the stresses are plotted at a location in the fiber which is close to the interface and on the plane of the matrix crack. For the toughest interface and the two strongest interfaces, it is seen that the stresses in the fiber are elevated during propagation of the matrix crack. For the case of the strongest interface, the stress concentration is quite severe. This indicates that for tough and/or strong interfaces, the propagation of the matrix crack can increase the stresses in the fiber, possibly causing the fiber to fracture.

6.5.2 Matrix Toughness

A parametric study of the matrix toughness was also performed. In Fig. 6.5.5 axial stress-strain curves for three different values of matrix toughness are shown. For the two least tough matrices the stress-strain response was qualitatively similar to that described in Section 6.5.1. As expected, for the tougher matrix, the matrix crack propagates at a higher

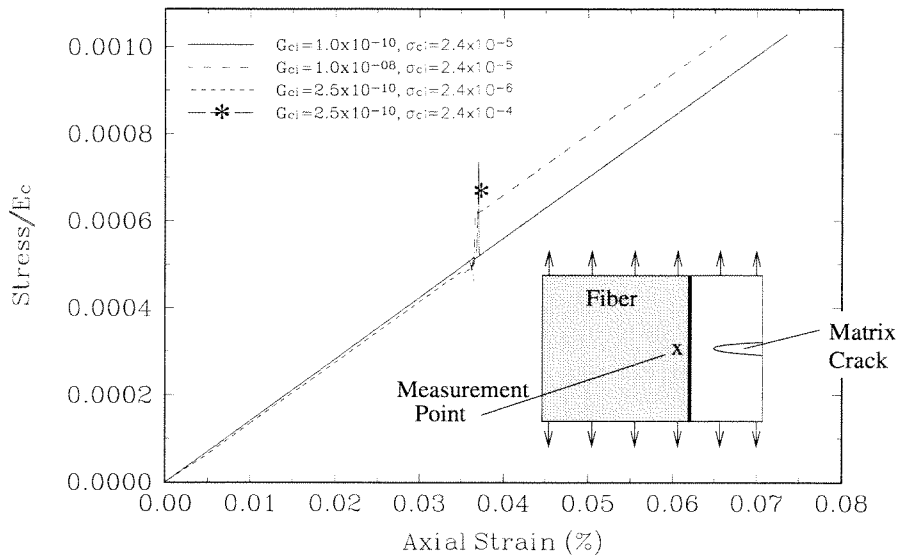

FIG. 6.5.4 A comparison of the stresses in a fiber on the plane ahead of a matrix crack for four different interface strengths and toughnesses.

load. For the toughest matrix, the matrix crack stops and requires significant further loading before propagating to the fiber. In Fig. 6.5.6, the sequence of matrix and interface cracking for the most and least tough matrix is shown. The point at which the interface cracking curve intersects its matrix cracking curve defines the percentage of cracked matrix when the interface cracking begins. This point of intersection is indicated by the circled regions in Fig. 6.5.6. For the low matrix toughness, the matrix crack has propagated approximately 80% of the distance to the fiber before the interface debonding (cracking) begins. For the high matrix toughness, interface debonding (cracking) begins once the matrix crack has propagated only 50% of the distance to the fiber. This result is expected since the toughness defines the amplitude of the stresses ahead of the crack tip. However, it also appears that the stress field from the matrix crack interacts with the fiber and can in some cases be blunted until the interface has cracked (debonded). This indicates that the relative toughness of the matrix, interface, and fiber may all play a role in the crack trapping and debonding process.

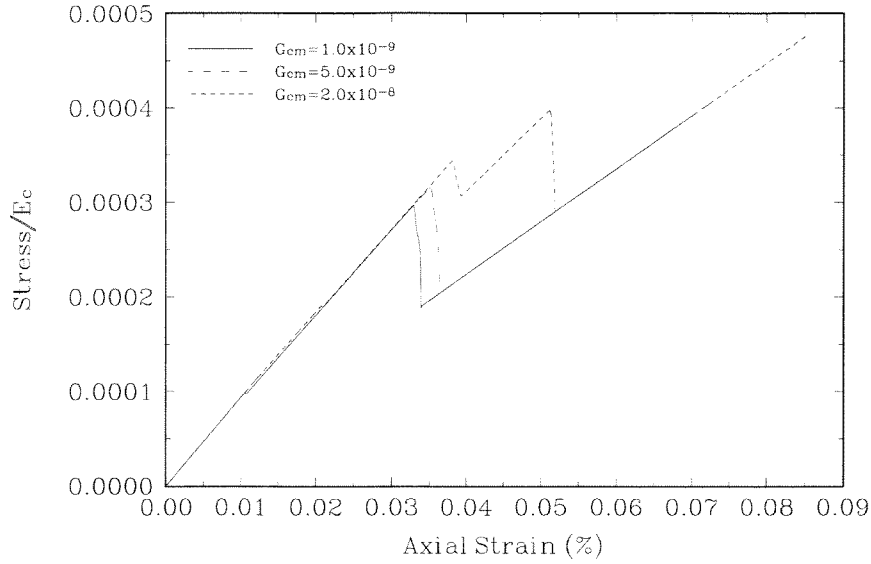

FIG. 6.5.5 Stress-strain curves for three different values of matrix toughness.

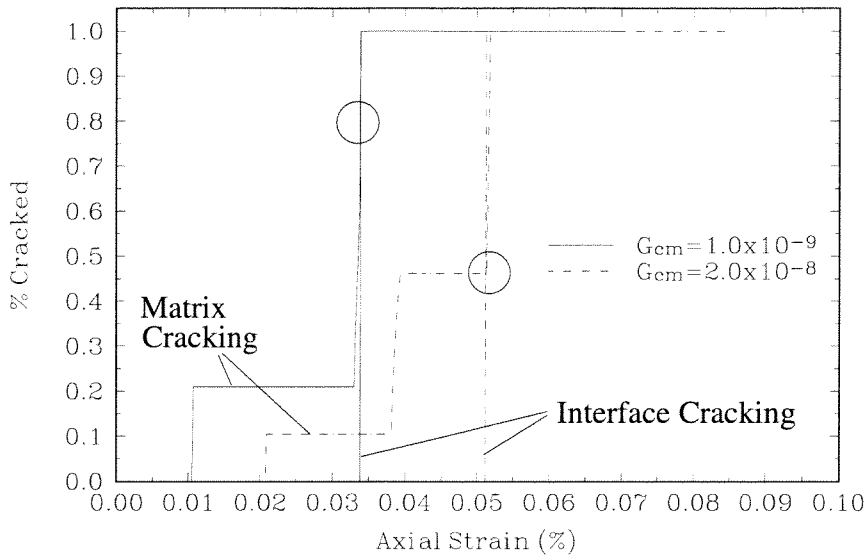

FIG. 6.5.6 The percentage of cracked matrix and interface for two matrix toughness values.

6.5.3 Loading Rate Effects

In their work on computational modeling of impact damage in brittle materials, Camacho and Ortiz (1995) noted that, in the cohesive element formulation, the stress needed to cause cohesive failure is rate dependent. Camacho and Ortiz (1995) derived the following relation by considering a stress pulse of duration τ and magnitude σ_i traveling at a speed c

towards a line of flaws and cohesive elements:

$$\sigma_i = \sigma_f \frac{\exp(\tau/t_c)}{\exp(\tau/t_c) - 1} \ , \tag{6.5.2}$$

where σ_f is the critical stress of the cohesive element, $t_c = \rho c \delta^* / 2\sigma_f$ with ρ being the material mass density and δ^* the critical displacement for cohesive failure. Thus, for shorter pulse durations, the stress necessary to cause cohesive failure increases rapidly. For long (quasi-static) times, the stress necessary to cause cohesive failure approaches the critical stress of the cohesive element (σ_f). For the current cohesive formulation, the same time dependence (Eq. 6.5.2) is present.

For fiber-matrix unit cell simulations, the effect of strain rate on the stress-strain curve is shown in Fig. 6.5.7. At the higher strain rate ($\dot{\epsilon} = 2 \times 10^{-6}$) the drop in stress is gradual, and it is delayed with respect to the lower strain rate ($\dot{\epsilon} = 2 \times 10^{-8}$) simulation. This can be seen in terms of percent cracking in Fig. 6.5.8, where the percent cracking of the matrix and the interface is plotted versus strain for the low and high strain rate simulations. For other choices of material parameters, it was found that the interface could completely debond even before the matrix flaw started to propagate. This is believed to be related to wave propagation effects in the fiber and matrix. Since the fiber is stiffer, the wave speed is higher, and therefore there will be a shear loading caused by different wave speeds in the matrix and the fiber.

The degree to which the numerical simulations at different strain rates parallel the experimental results in Chapters 2 and 5 for fiber reinforced materials is unknown. As was the case for the numerical simulations, in the experiments it was also found that matrix cracking is delayed for higher rates of loading. However, this delay may be caused by the dynamics of propagation of the matrix cracks and their interactions with the fibers and the debond cracks. It is not known to what extent the dynamics of crack propagation are simulated in the present numerical model; nor is it known to what extent the rate dependence of the cohesive model plays a role. Further investigation of this subject is required.

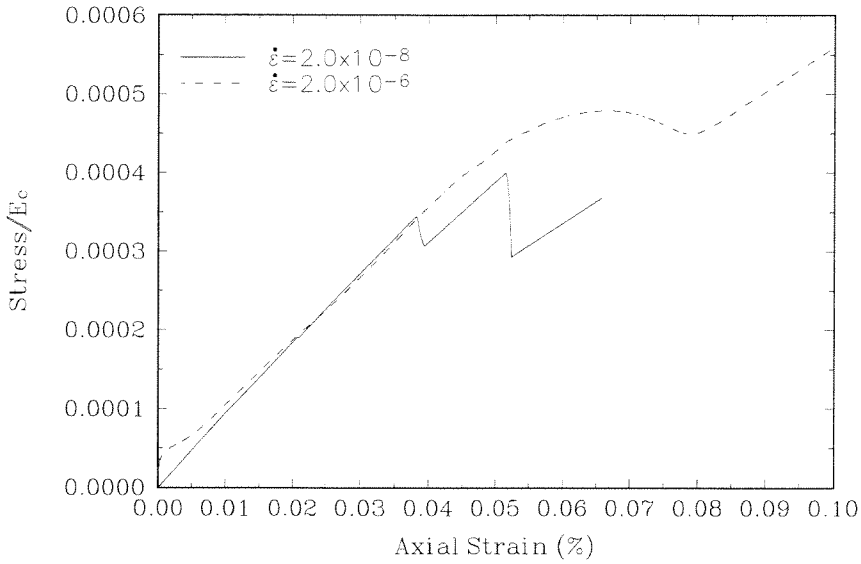

FIG. 6.5.7 The effect of displacement rate on the axial stress-strain curve for fixed cohesive parameters ($\mathcal{G}_{ci} = 1 \times 10^{-9}$, $\mathcal{G}_{cm} = 2 \times 10^{-8}$, $\sigma_{ci} = 2.4 \times 10^{-5}$).

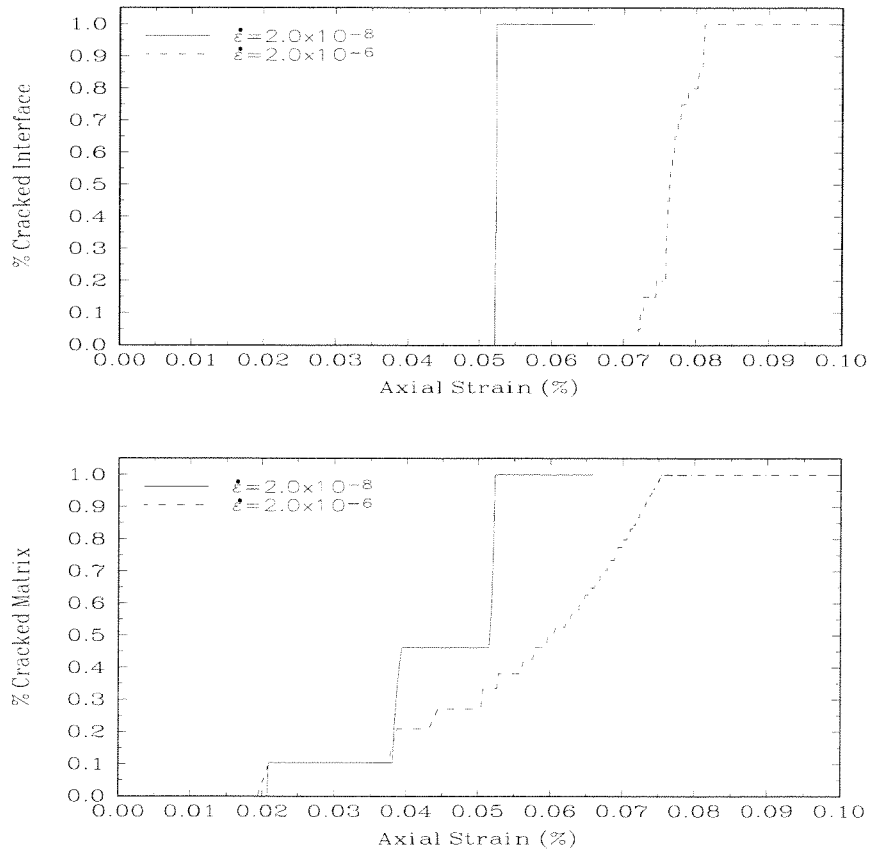

FIG. 6.5.8 The effect of displacement rate on the cracking of the interface and matrix (top and bottom plots, respectively) for the simulations at different strain rates shown in Fig. 6.5.7.

6.5.4 Flaw Initiation and Propagation

As was the case for the experiments in Chapter 2, it was desired to determine the sequence and extent of cracking in the numerical simulations. For this purpose, the numerical simulations were performed at low strain rates ($\dot{\epsilon} = 2 \times 10^{-8}$), and the long unit cell described earlier was used so as to avoid crack interactions with the boundary. The interface toughness ($\mathcal{G}_{ci}$) and strength (σ_{ci}) was set to 1.0×10^{-9} and 2.4×10^{-5}, respectively, and the matrix toughness ($\mathcal{G}_{cm}$) was 2.0×10^{-8}. In Fig. 6.5.9, the radial stress at six different strain levels is shown. The contours clearly show the propagation of the matrix crack towards the fiber-matrix interface. It is seen that the interface is deforming extensively well before the matrix crack reaches it. In addition, there are two symmetric lobes associated with the matrix crack which interact with the interface. It is seen that these lobes have compressive stresses which initially cause non-continuous deformation of the interface. At later loading stages the lobes appear to be pinned to the interface and subsequently separate due to stresses from the matrix crack which have caught up to the lobes. These simulations show the importance of the anisotropic nature of the fiber-matrix unit cell.

6.5.5 Debonding Criteria

Debonding is essential for toughening fiber reinforced composites. In the absence of debonding matrix cracks propagate through the fibers and catastrophic failure occurs at very low strain levels. Cook and Gordon (see Gordon, 1979) studied crack tip fields and concluded that debonding occurs *before* the crack reaches the interface when the interface strength is 1/5 the strength of the matrix. This will henceforth be referred to as the Cook-Gordon Mechanism. More recently, He and Hutchinson (1989) developed a criterion for debonding that is based on the ratio between the interface toughness and the fiber toughness (referred to as the He and Hutchinson Criterion).

The He and Hutchinson Criterion was established by assuming cracked configurations and then determining the direction of further propagation. The initial configuration contains

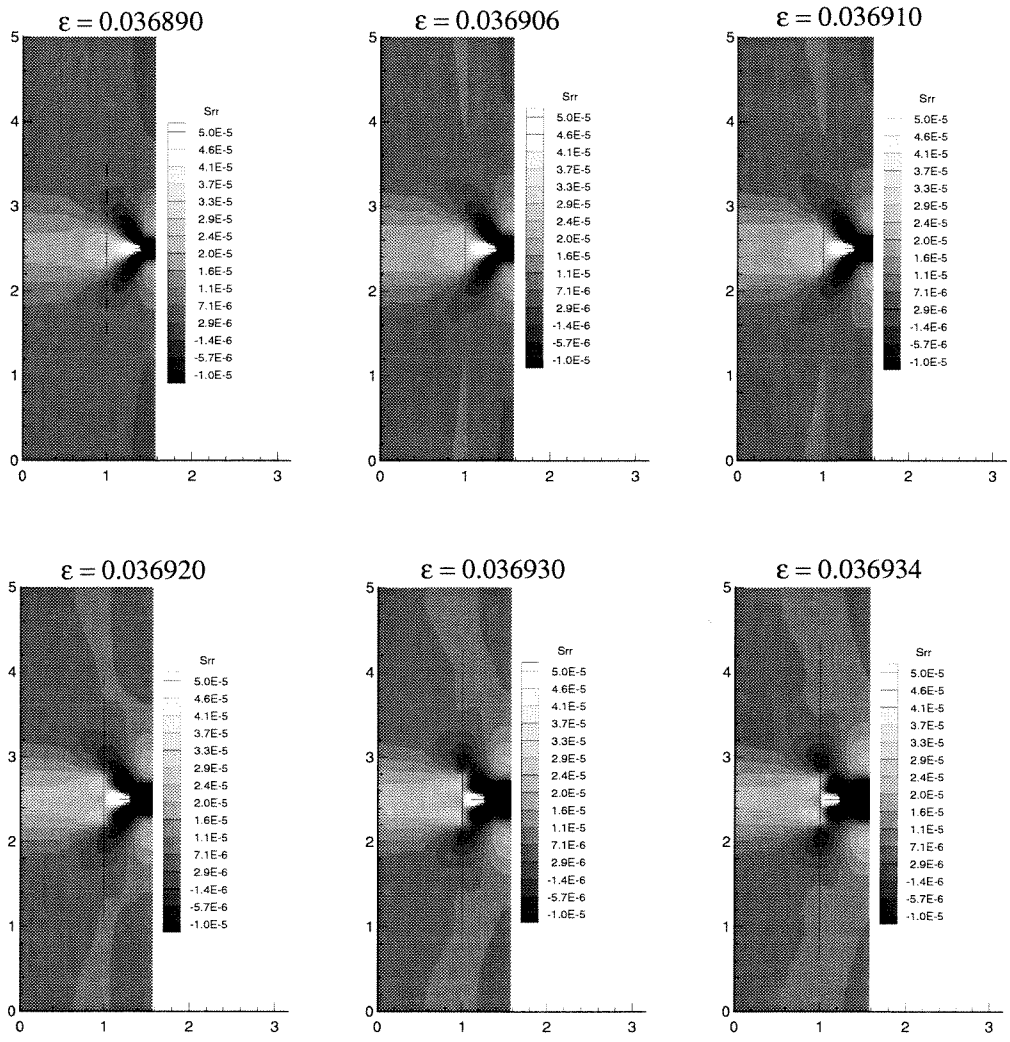

FIG. 6.5.9 Six contour plots of the radial stresses for increasing far-field displacement (from left to right and top to bottom).

a crack in the matrix which ends at the interface. This crack configuration could occur for composites with very strong interfaces. For this situation it was determined that the ratio between the interface and fiber toughnesses determine the cracking sequence as follows:

$$\frac{\mathcal{G}_{ci}}{\mathcal{G}_{fi}} \begin{cases} \leq \frac{1}{4} & \text{debonding} \\ > \frac{1}{4} & \text{fiber cracking.} \end{cases}$$

In light of the results for a very strong interface shown in Fig. 6.5.4, it is realized that the fiber must be very tough to avoid failure due to the stress concentration. Typically in

composites, there is a tendency to use very stiff, brittle fibers. Therefore the numerical simulations show that a very strong interface is undesirable.

For composites with a very weak interface, the stress concentration in the fibers are avoided because debonding occurs before the matrix crack reaches the fiber-matrix interface. In this situation the He and Hutchinson Criterion is not valid because the assumed crack configurations do not exist. The Cook-Gordon Mechanism addressed the debonding of the interface by a matrix crack away from the interface. This mechanisms is shown schematically in Fig. 6.5.10.

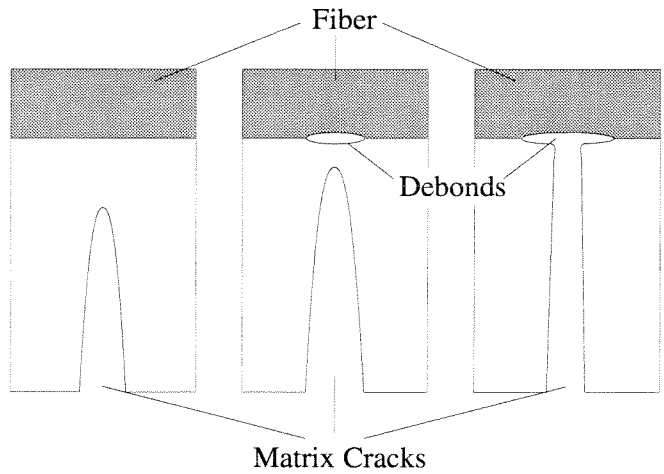

FIG. 6.5.10 A schematic of Cook-Gordon Mechanism for stopping cracks at weak interfaces.

The Cook-Gordon Mechanisms approximated the maximum tension stresses on the plane of a crack as being approximately 1/5th the maximum opening stresses. Therefore their assumption was that for interfaces that are 1/5th the strength of the matrix, debonding will occur before the matrix crack reaches the interface.

In the present results we have postulated that the Cook-Gordon Mechanisms is active in the experiments discussed in Chapter 2. In addition, there has been clear evidence of debonding ahead of the crack tip during numerical simulations. There are several refinements of the Cook-Gordon Mechanism that require attention. For one, the matrix to interface ratio of 1/5th does not take into account the variation of the stress field due to the

presence of fibers. In addition, intuitively, it is logical that the matrix toughness should enter the formulation of a debonding criterion since the toughness will determine the magnitude of the stresses ahead of the matrix crack. Thus, in summary, it is seen that there is still need for a debonding criterion for weak interface composites which accounts for the anisotropy of the cracked material, the strength and toughness of the interface and the toughness of the matrix.

6.6 Summary

Finite element simulations using cohesive elements have been used to study the deformation of fiber reinforced composites. Cohesive elements were included in the discretization of an axisymmetric fiber-matrix unit cell so that cracks could form in the radial direction anywhere in the fiber and matrix and in the axial direction along the fiber-matrix interface. The cohesive elements were governed by critical energy release rates and critical failure stresses in the shear and normal directions. A frictional formulation was added such that failed cohesive elements could slide with Coulomb friction. In order to obtain converged solutions for the unit cell simulation, inertia and viscosity were added to the formulation. The resulting dynamic problem was solved implicitly with the Newmark Method and with minimal numerical damping.

The cohesive method was validated for axisymmetry by comparing the analytical and numerical solutions of a Dugdale penny shaped crack in a large cylinder. In addition, the wave propagation in and subsequent failure of a one dimensional bar was analyzed.

At the point when the matrix crack propagated to the fiber-matrix interface, the fiber-matrix unit cell simulations revealed a sharp drop in the axial stress-strain response. Debonding of the interface generally occured well before the matrix crack reached the interface. The transverse strain response depended on the extent of debonding. When large sections of the interface were still intact there was an initial reversal in the transverse strain when

the matrix cracks propagated and a second reversal occured due to Poisson contraction of the fiber.

Several features of the experimental results with a fiber reinforced ceramic matrix composite were simulated numerically. In terms of modeling the response of a complete fiber reinforced composite, it would be necessary to incorporate an averaging scheme which incorporates the percentage of active unit cells at a given point in the loading history. In this way, simulation of gradual propagation of cracks through a composite would be achieved, and the overall composite stress-strain response would have a gradual leveling off followed by a re-stiffening response.

Parametric studies of the interface strength and toughness and the matrix toughness were performed on short unit-cell models. It was found that strong interfaces led to high stress concentrations in the fiber. In such situations, catastrophic brittle failure would occur since the matrix crack would propagate through the fiber and not be deflected onto the interface. The crack trapping mechanisms of strong interfaces were not clearly identified, possibly due to the effects of axisymmetry. Matrix toughness was found to have important effects regarding the onset of debonding and also in terms of trapping the propagating matrix crack. The source of rate dependence in the cohesive model was observed and the implications were discussed.

The flaw initiation and propagation was studied with a long fiber-matrix unit cell. The interaction of the stress fields from the matrix crack with the fiber and fiber-matrix interface are quite complicated. As was the case for the shorter unit cell, the interface debonds before the arrival of the matrix crack. Compressive lobes from the matrix crack appear to inhibit the formation of debonds near the plane of the matrix crack. Away from the plane of the matrix crack shear stresses dominate and the debonding mechanism is active. It is possible that for longer simulations additional matrix cracks would form.

The propagation of debond cracks before the matrix crack reaches the interface is consistent with the Cook-Gordon Mechanism (see Gordon, 1979). Previously established

debonding criteria (*e.g.*, He and Hutchinson, 1989) assume that the matrix crack has reached the interface, and depending on the ratio between the interface and fiber toughness, the matrix crack could continue to propagate either into the fiber or along the interface. This result establishes the upper bound for interface toughness of very strong interfaces (*i.e.*, interfaces that will not debond before the matrix crack reaches the fiber). For weak interface composites, a debonding criteria is needed which will account for the strength of the interface and the toughness of the matrix. Future study along these lines is needed.

The numerical model presented in this chapter could be used for a number of related studies. In particular, in the above only a cohesive (zero thickness) interface was incorporated. The effects of a finite thickness interface could provide a basis for future study. In addition, residual stresses have been postulated to play an important role in fiber reinforced composites. The effect of residual stresses could easily be incorporated in future numerical simulations.

CHAPTER 7

Conclusions

7.1 Summary

The evolution of damage in a unidirectional ceramic matrix composite was studied. The damage was characterized with post-test microscopy and through *in situ* strain, acoustic emission and ultrasonic sensing. The following mechanisms were observed: matrix cracking, fiber bridging, debonding and fiber pull-out. The monotonic loading history for loading in the fiber direction was divided into five "zones of deformation." Each individual zone was assumed to be dominated by a single damage mechanism. It was shown that the experimental measurements could be explained in terms of fiber and matrix material properties, the material processing and the postulated zones of deformation.

After the onset of damage in brittle matrix composites, energy is dissipated during the deformation process. From the axial stress-strain curve and quantitative knowledge of the change in the axial modulus, it was possible to calculate the percentage of unrecoverable energy that was dissipated at each stage of the loading history. Results indicated that debonding plays a significant role in dissipating energy during the useful life of a brittle matrix composites.

The applicability of two models of matrix cracking was investigated. It was found that a traditional shear-lag model required detailed information about several material properties. This posed problems since, in general, the *in situ* properties of brittle matrix composites are, in general, not well known. A second model of matrix cracking based on penny shaped cracks was used to calculate the change in axial modulus as a function of crack density. It

was found that the shape of the crack density function could be determined from acoustic emission results.

The formation and propagation of damage in ceramic matrix composites was found to be strain rate dependent. For quasi-static experiments at higher strain rates, the stress at which the axial modulus degrades was nearly twice as high as that for lower strain rate experiments. In addition, significant differences in the transverse strain behavior for higher and lower strain rate experiments was observed. Acoustic emission results for higher strain rate experiments indicate that the onset and subsequent saturation of matrix cracking is delayed for higher rates of loading.

Experiments with a model composite were performed to further investigate the details of damage formation in brittle matrix composites. The primary advantages of the model composite system were its simple geometry and the ability to quantify the stress state during damage initiation and propagation. In particular, the propagation of debond cracks could be visualized. For the model composite, at higher rates of loading, periodic cracks in the matrix were inhibited and debonds were prominent. It is believed that the same rate dependent transition in damage propagation was present in the higher loading rate deformation of the actual fiber reinforced ceramic matrix composite.

To model the overall composite response in the presence of growing matrix and debond cracks, numerical (finite element) simulations were undertaken. A cohesive element formulation was implemented and a fiber-matrix axisymmetric unit cell was discretized to allow cracking throughout the fiber and the matrix in the radial direction. In addition the fiber could be debonded from the matrix. A parametric study of the matrix toughness and the interface toughness and strength demonstrate the importance of these parameters on the axial load carrying capability and the transverse strain. The details of crack propagation and subsequent debonding of the fiber were visualized for a unit cell. The effect of loading rate on the axial response was also noted.

During these investigations, several new aspects of the deformation of composites have been realized. It was observed that there was transverse damage induced anisotropy in the SiC/CAS unidirectional composite; this most likely was the result of a layered microstructure and preferential debonding of the fiber-matrix interface. As has already been noted, debonding was found to be an important mechanism from the standpoint of dissipating energy (*i.e.*, improving the toughness). Along these lines, although other authors have noted that the transverse strain in unidirectional composites will undergo a reversal during uniaxial tension loading in the fiber direction, it has not been thoroughly explained. In addition, the second reversal in transverse strain has not been previously documented. In the present study, reversals have been explained based on material properties and the evolution of damage. The numerical modeling also provided new information related to debonding of the fiber-matrix interface. As a result of high tensile stresses at the tips of the matrix cracks, it was found that the fiber-matrix interface debonds before the matrix crack actually reaches the interface. The has important implications for the development of debonding criteria.

The importance of strain rate on the deformation of ceramic matrix composites has not yet been documented in the literature. In the present investigation the dependence of damage propagation on strain rate was found to be quite significant. The work with a model composite material also represents the first time that the details of matrix crack and debond crack formation have been experimentally reproduced in an easily analyzed configuration.

7.2 Macroscopic Composite Response

The initial and final behavior of a fiber reinforced composite can be determined from the properties of the matrix, interface and fiber. For a unidirectional composite with weak fiber-matrix interfaces, the material response for loading in the fiber direction is shown schematically in Fig. 7.2.1. This figure indicates that the composite response is linear up until the point that the matrix reaches its failure strain (ϵ_m^f). The composite modulus (E_c)

is slope of this initial linear region, and it can be determined from a rule of mixtures. If the fiber-matrix interfaces were sufficiently strong and tough, the composite would fail catastrophically at a maximum strain of ϵ_m^f. Instead, with weaker interfaces, the fibers play an important role. Just before propagation of a macroscopic crack through the composite, the stress-strain response is nearly linear and correlates with the modulus and volume fraction of the fibers. The ultimate stress and strain of the composite is related to the ultimate stress and strain of the fiber bundle (σ_f^f and ϵ_f^f in Fig. 7.2.1). Laminate response can be characterized similarly by properly adjusting the total volume fraction of fibers to be that of the load carrying fibers. The details of the composite response between the initially linear region and the fiber loading region are schematically denoted by the dashed line in Fig. 7.2.1. These details were the subject of this dissertation. The loading path denoted by the dashed line was found to be strain rate dependent and was important in terms of dissipating unrecoverable energy. This has implications for improving the toughness of composites and for life prediction modeling.

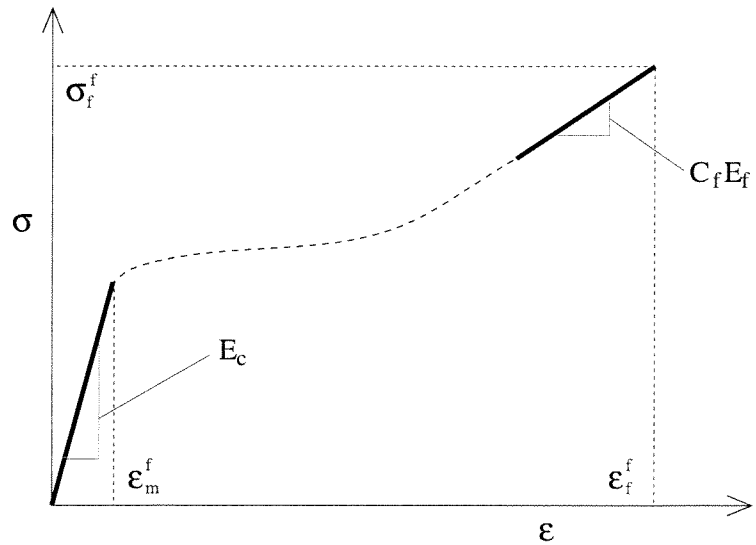

FIG. 7.2.1 A schematic of the response of a fiber reinforced composite.

The two phase nature of composites is advantageous for several reasons. First, the toughness of the material is improved through crack stopping and deflecting mechanisms

and bridging and sliding mechanisms. Also, because the fibers are very small, the existence of critical Griffith flaws is minimized, and therefore the fiber strength is relatively high. Furthermore, large statistical variations in the individual constituents do not lead to catastrophic failure since each phase absorbs some of the statistical variations of other phase. The improvement of composites is often discussed in terms of extending the initial linear region and improving the ultimate strength. In terms of the discussion above, the lengthening of the elastic region can be accomplished by choosing a matrix with a high failure strain. It must be chosen so as to maintain the condition that upon over-stressing of the matrix, matrix cracks will debond the fibers and not propagate through the fibers. The ultimate strength and strain to failure of the composite can be enhanced through improvements of the fiber bundle properties.

7.3 Future Work

As with most research projects, the work in a dissertation answers some questions and raises many more. In the present work, there are several issues that require further investigation.

As was discussed in Chapter 3, the *in situ* properties of brittle matrix composites are not well known. This is due to the lack of experimental data on the individual constituents and the likelihood that the constituent properties are significantly altered during processing of the material. Detailed knowledge of the material properties is necessary for modeling purposes. In particular, for the numerical model discussed in this work, the critical energy release rates and critical stresses for failure of all constituents were needed. In the discussion of the numerical parameters (see Section 6.3.2), it was observed that there is, in general, a lack of information on the failure of ceramics in shear and that composite interfaces are also not well characterized. In addition, the residual stresses have not been quantified. It is probable that residual stresses play a significant role; their effect could be investigated using the numerical model discussed in this work. The results of investigation into the *in situ*

properties of ceramic matrix composites would have important implications for choosing the optimal constituents and processing methods.

As was discussed in Section 6.5.5, for composites with weak interfaces, matrix cracks tend to debond the interface before reaching it, *a la* the Cook-Gordon Mechanism (see Gordon, 1979). A debonding criterion which accounts for the interface strength and toughness, as well as the matrix toughness, is required. In addition, considering the strain rate effects discussed in Chapters 4 and 5, ultimately, a debonding criterion would need to account for the dynamics of matrix crack propagation.

Another area of interest relates to the layered microstructure observed in ceramic matrix composites. In terms of modeling efforts, the uniformity of composite microstructure is typically not addressed. Experimentally, the details of the damage formation with respect to the layered structure have not been investigated. Knowledge of the advantages and/or disadvantages of such microstructural features is important for determining the proper processing techniques for ceramic matrix composites.

The long range goal of modeling brittle matrix composites requires detailed understanding of the dominant damage mechanisms at all stages of various thermomechanical loading histories. This has been started for unidirectional laminates at room temperature. It is necessary to do similar studies at higher temperatures. In addition, future composite structures will be composed of cross-ply laminates. The study of laminate response at room temperature and high temperatures is another important area of research. Both unidirectional and cross-ply laminates of ceramic matrix composite also require further study under thermomechanical fatigue and creep loading. Although preliminary research under these loading conditions has been done, the deformation mechanisms are not well understood. Higher rates of loading also form an important area of investigation. In this dissertation, the effect of loading rate on unidirectional laminates has been documented. Further study of the damage transition with loading rate needs to be undertaken, and similar studies of the effect of loading rate on cross-ply laminates should also be performed.

The use of metals as structural engineering materials has been made possible by extensive research over many decades. Advanced ceramic matrix composites are a relatively new class of materials which is and will continue to change rapidly. Research must keep up with these changes and suggest new changes in order to take advantage of the properties of ceramic matrix composites in future structural engineering applications.

REFERENCES

American Society for Testing and Materials, 1993, "Practice for Verification of Specimen Aligment Under Tensile Loading," *1993 Annual Book of ASTM Standards*, Vol. 03.01, No. E-1012.

Ashby, M.F. and Jones, D.R.H., 1980b, *Engineering Materials 2: An Introduction to Microstructures, Processing and Design.* Oxford: Pergamon Press.

Aveston, J., Cooper, G.A. and Kelly, A., 1971, "Single and Multiple Fracture," *The Properties of Fibre Composites*, Guilford, UK, IPC Science and Technology Press, pp. 15–26.

Aveston, J. and Kelly, A., 1973, "Theory of Multiple Fracture of Fibrous Composites," *J. Mater. Sci.*, Vol. 8, pp. 352–362.

Aveston, J., Mercer, R.A. and Sillwood, J.M., 1971, *Composites-Standards, Testing and Design*, Conference Proceedings, National Physical Laboratory, Surry, England, Guildford IPC Science and Technology Press, pp. 93–102.

Barenblatt, G.I., 1962, "Mathematical Theory of Equilibrium Cracks," *Advances in Applied Mechanics*, Vol. VII, Eds., New York, Academic Press, pp. 59–129.

Barsoum, M.W., Kangutkar, P. and Wang, A.S.D., 1992, "Matrix Crack Initiation in Ceramic Matrix Composites Part I: Experiments and Test Results," *Comp. Sci. Tech.*, Vol. 44, pp. 257–269.

Bathe, H.J., 1982, *Finite Element Procedures in Engineering Analysis.* New Jersey: Prentice-Hall, Inc..

Beyerle, D.S., Spearing, S.M., Zok, F.W. and Evans, A.G., 1992, "Damage and Failure in Unidirectional Ceramic-Matrix Composites," *J. Am. Ceram. Soc.*, Vol. 75, pp. 2719–2725.

Bischoff, E., Rühle, M., Sbaizero, O. and Evans, A.G., 1989, "Microstructural Studies of the Interfacial Zone of a SiC-Fiber-Reinforced Lithium Aluminum Silicate Glass-Ceramic," *J. Am. Ceram. Soc.*, Vol. 72, pp. 741–745.

Botsis, J. and Beldica, C., 1994, "Strength Characteristics and Fatigue-Crack Growth in a Composite with Long Aligned Fibers," *Int. J. Fract.*, Vol. 69, pp. 27–50.

Botsis, J. and Shafiq, A.B., 1992, "Crack Growth Characteristics of an Epoxy Reinforced with Long Aligned Glass Fibers," *Int. J. Fract.*, Vol. 58, pp. R3–R10.

Brennan, J.J. and Prewo, K.M., 1982, "Silicon Carbide Fibre Reinforced Glass-Ceramic Matrix Composites Exhibiting High Strength and Toughness," *J. Mater. Sci.*, Vol. 17, pp. 2371–2383.

Budiansky, B., Evans, A.G. and Hutchinson, J.W., 1995, "Fiber-Matrix Debonding Effects on Cracking in Aligned fiber Ceramic Composites," *Int. J. Sol. Struct.*, Vol. 32, pp. 315–328.

Budiansky, B., Hutchinson, J.W. and Evans, A.G., 1986, "Matrix Fracture in Fiber-Reinforced Ceramics," *J. Mech. Phys. Sol.*, Vol. 34, pp. 167–189.

Butkus, L.M., Holmes, J.W. and Nicholas, T., 1993, "Thermomechanical Fatigue Behavior of a Silicon Carbide Fiber-Reinforced Calcium Aluminosilicate Composite," *J. Am. Ceram. Soc.*, Vol. 76, pp. 2817–2825.

Cady, C.M., Mackin, T.J. and Evans, A.G., 1995, "Silicon Carbide/Calcium Aluminosilicate: A Notch-Insensitive Ceramic-Matrix Composite," *J. Am. Ceram. Soc.*, Vol. 78, pp. 77–82.

Camacho, G.T. and Ortiz, M., 1995,"Computational Modelling of Impact Damage in Brittle Materials," submitted to the *Int. J. Sol. Struct.*

Cao, H.C., Bischoff, E., Sbaizero, O., Ruhle, M., Evans, A.G., Marshall, D.B. and Brennan, J.J., 1990, "Effect of Interfaces on the Properties of Fiber-Reinforced Ceramics," *J. Am. Ceram. Soc.*, Vol. 73, pp. 1691–1699.

Charalambides, P.G. and Evans, A.G., 1989, "Debonding of Residually Stressed Brittle-Matrix Composites," *J. Am. Ceram. Soc.*, Vol. 72, pp. 746–53.

Cho, C., Holmes, J.W. and Barber, J.R., 1992, "Distribution of Matrix Cracks in a Uniaxial Ceramic Composite," *J. Am. Ceram. Soc.*, Vol. 75, pp. 316–324.

Cooper, R.F., 1994, University of Wisconsin, Madison, Personal Communication.

Cranmer, D.C., 1991, "Workshop on Assessment of Testing Methodology for Glass, Glass-Ceramic and Ceramic Matrix Composites," *J. Res. NIST*, Vol. 96, pp. 493–501.

Crisfield, M.A., 1983, "An Arc-Length Method Including Line Searches and Accelerations," *Int. J. Num. Meth. Engin.*, Vol. 19, pp. 1269–1289.

Dally, J.W. and Riley, W.F., 1991, *Experimental Stress Analysis.* New York: McGraw-Hill, Inc..

Danchaivijit, S. and Shetty, D.K., 1993, "Matrix Cracking in Ceramic-Matix Composites," *J. Am. Ceram. Soc.*, Vol. 76, pp. 2497–2504.

Daniel, I.M. and Anastassopoulos, G., 1995, "Failure Mechanisms and Damage Evolution in Cross-Ply Ceramic-Matrix Composites," *Int. J. Sol. Struct.*, Vol. 32, pp. 341–355.

Daniel, I.M., Anastassopoulos, G. and Lee, J-W., 1993, "The Behavior of Ceramic Matrix Fiber Composites under Longitudinal Loading," *Comp. Sci. Tech.*, Vol. 46, pp. 105–113.

Deng, H. and Nemat-Nasser, S., 1992, "Microcrack Arrays in Isotropic Solids," *Mech. Mater.*, Vol. 13, pp. 15–36.

Dharani, L.R. and Recker, R.L., 1991, "Growth of Longitudinal Matrix Damage in Unidirectional Composites," *Eng. Fract. Mech.*, Vol. 38, pp. 185–195.

Dharani, L.R. and Tang, H., 1990, "Micromechanics Characterization of Sublaminate Damage," *Int. J. Fract.*, Vol. 46, pp. 123–140.

Dollar, A. and Steif, P.S., 1989, "A Tension Crack Impinging Upon Frictional Interfaces," *J. Appl. Mech.*, Vol. 56, pp. 291–298.

Dollar, A. and Steif, P.S., 1992, "Interface Blunting of Matrix Cracks in Fiber-Reinforced Ceramics," *J. Appl. Mech.*, Vol. 59, pp. 796–803.

Dugdale, D.S., 1960, "Yielding of Steel Sheets Containing Slits," *J. Mech. Phys. Sol.*, Vol. 8, pp. 100–104.

Eitzen, D.G. and Wadley, H.N.G., 1984, "Acoustic Emission: Establishing the Fundamentals," *J. of Res. of the Nat. Burea of Stand.*, Vol. 89, pp. 75–91+.

Evans, A.G., 1990, "Perspective on the Development of High Toughness Ceramics," *J. Am. Ceram. Soc.*, Vol. 73, pp. 187–206.

Evans, A.G. and Charles, E.A., 1976, "Fracture Toughness Determinations by Indentation," *J. Am. Ceram. Soc.*, Vol. 59, pp. 371–372.

Evans, A.G. and Marshall, D.B., 1989, "The Mechanical Behavior of Ceramic Matrix Composites," *Acta Metall. Mater.*, Vol. 37, pp. 2567–2583.

Freund, L.B., 1992, "The Axial Force Needed to Slide a Circular Fiber Along a Hole in an Elastic-Material and Implications for Fiber Pull-out," *Eur. J. Mech. A/Sol.*, Vol. 11, pp. 1–19.

Geubelle, P.H. and Knauss, W.G., 1994, "Crack-Propagation at and Near Bimaterial Interfaces—Linear Analysis," *J. Appl. Mech.*, Vol. 61, pp. 560–566.

Giannakopoulos, A.E., 1989, "The Return Mapping Method for the Integration of Friction Constitutive Relations," *Comp. & Struct.*, Vol. 32, pp. 157–167.

Gordon, J.E., 1979, *The New Science of Strong Materials.* London: Pitman Publishing Limited.

Gu, P., 1993, "Multilayer Material with an Interface Crack," *J. Appl. Mech.*, Vol. 60, pp. 1052–1054.

Habib, F.A., Taylor, R.A.J., Cooke, R.G. and Harris, B., 1993, "Fatigue Damage in SiC/CAS Composites," *Composites*, Vol. 24, pp. 157–165.

Harris, B., Habib, F.A. and Cooke, R.G., 1992, "Matrix Cracking and the Mechanical Behavior of SiC-CAS Composites," *Proc. Roy. Soc. Lond.*, Vol. 437, pp. 109–131.

Hashin, Z., 1983, "Analysis of Composites Materials–A Survey," *J. Appl. Mech.*, Vol. 50, pp. 481–505.

He, M-Y. and Hutchinson, J.W., 1989a, "Crack Deflection at an Interface between Dissimilar Elastic Materials," *Int. J. Sol. Struct.*, Vol. 25, pp. 1053–1067.

He, M-Y and Hutchinson, J.W., 1989, "Kinking of a Crack Out of an Interface," *J. Appl. Mech.*, Vol. 56, pp. 270–278.

He, M.Y., Wu, B.-X., Evans, A.G. and Hutchinson, J.W., 1994, "Inelastic Strains due to Matrix Cracking in Unidirectional Fiber-Reinforce Composites," *Mech. Mater.*, Vol. 18, pp. 213–229.

Holmes, J.W. and Cho, C., 1992, "Experimental Observations of Frictional Heating in Fiber-Reinforced Ceramics," *J. Am. Ceram. Soc.*, Vol. 75, pp. 929–938.

Hughes, T.J.R., 1983, "Analysis of Transient Algorithms with Particular Reference to Stability Behavior," *Computational Methods for Transient Analysis*, T. Belytschko and T.J.R. Hughes, Eds., Amsterdam, North-Holland, pp. 67–155.

Hughes, T.J.R., 1987, *The Finite Element Method — Linear Static and Dynamic Finite Element Analysis.* New Jersy: Prentice-Hall, Inc..

Hutchinson, J.W. and Jensen, H.M., 1990, "Models of Fiber Debonding and Pullout in Brittle Composites with Friction," *Mech. Mater.*, Vol. 9, pp. 139–163.

Kander, R.G. and Siegmann, A., 1992, "The Effect of Strain Rate on Damage Mechanisms in a Glass/Polypropylene Composite," *J. Comp. Mater.*, Vol. 26, pp. 1455–1472.

Krandikar, P. and Chou, T-W., 1993, "Characterization and Modeling of Microcracking and Elastic Moduli Changes in Nicalon/CAS Composites," *Comp. Sci. Tech.*, Vol. 46, pp. 253–263.

Katz, A.P. and Kerans, R.J., 1988, "Structural Ceramics Program at AFWAL Materials Lab," *Am. Ceram. Soc. Bull.*, Vol. 67, pp. 1360–1366.

Kerans, R.J., Hay, R.S., Pagano, N.J. and Parthasarathy, T.A., 1989, "The Role of the Fiber-Matrix Interface in Ceramic Composites," *Am. Ceram. Soc. Bull.*, Vol. 68, pp. 429–442.

Kerans, R.J. and Parthasarathy, T.A., 1991, "Theoretical Analysis of the Fiber Pullout and Pushout Tests," *J. Am. Ceram. Soc.*, Vol. 74, pp. 1585–1596.

Kim, R.Y. and Pagano, N.J., 1991, "Crack Initiation in Unidirectional Brittle-Matrix Composites," *J. Am. Ceram. Soc.*, Vol. 74, pp. 1082–1090.

Kim, H.S., Yong, J.A., Rawlings, R.D. and Rogers, P.S., 1991, "Interfacial Behavior of Fibre Reinforced Glass Ceramic Composite at Elevated Temperature," *Mat. Sci. Tech.*, Vol. 7, pp. 155–157.

Krajcinovic, D., 1989, "Damage Mechanics," *Mech. Mater.*, Vol. 8, pp. 117–197.

Kuo, W-S. and Chou, T-W., 1995, "Multiple Cracking of Unidirectional and Cross-Ply Ceramic Matrix Composites," *J. Am. Ceram. Soc.*, Vol. 78, pp. 745–755.

Lambros, J.M. and Rosakis, A.J., 1995, to appear in *Proc. Roy. Soc. Lond.*

Lamon, J., Rebillat, F. and Evans, A.G., 1995, "Microcomposite Test Procedure for Evaluating the Interface Properties of Ceramic Matrix Composites," *J. Am. Ceram. Soc.*, Vol. 78, pp. 401–405.

Lankford, J., Couque, H. and Nicholls, A., 1992, "Effect of Dynamic Loading on Tensile Strength and Failure Mechanisms in a SiC Fibre Reinforced Ceramic Matrix Composite," *J. Mater. Sci.*, Vol. 27, pp. 930–936.

Laracurzio, E. and Ferber, M.K., 1994, "Methodology for the Determination of the Interfacial Properties of Brittle-Matrix Composites," *J. Mater. Sci.*, Vol. 29, pp. 6152–6158.

Laws, N., 1985, "A Note on Penny-Shaped Cracks in Transversely Isotropic Materials," *Mech. Mater.*, Vol. 4, pp. 209–212.

Lee, Y.J., Lambros, J. and Rosakis, A.J., 1995,"Analysis of Coherent Gradient Sensing (CGS) by Fourier Optics," to appear in *Optics and Lasers in Eng.*

Llorca, J. and Singh, R.N., 1991, "Influence of Fiber and Interfacial Properties on Fracture-Behavior of Fiber-Reinforced Ceramic Composites," *J. Am. Ceram. Soc.*, Vol. 74, pp. 2882–2890.

Luh, E.Y. and Evans, A.G., 1987, "High-Temperature Mechanical Properties of a Ceramic Matrix Composite," *J. Am. Ceram. Soc.*, Vol. 70, pp. 466–469.

Mackin, T.J., Purcell, T.E., He, M.Y. and Evans, A.G., 1995, "Notch Sensitivity and Stress Redistribution in 3 Ceramic-Matrix Composites," *J. Am. Ceram. Soc.*, Vol. 78, pp. 1719–1728.

Mah, T., Mendiratta, M.G., Katz, A.P., Ruh, R. and Mazdiyasni, K.S., 1985a, "Room-Temperature Mechanical Behavior of Fiber-Reinforced Ceramic-Matrix Composites," *J. Am. Ceram. Soc.*, Vol. 68, pp. C27–C30.

Mah, T., Mendiratta, M.G., Katz, A.P., Ruh, R. and Mazdiyasni, K.S., 1985b, "High-Temperature Mechanical Behavior of Fiber-Reinforced Ceramic-Matrix Composites," *J. Am. Ceram. Soc.*, Vol. 68, pp. C248–C251.

Marshall, D.B., 1992, "Analysis of Fiber Debonding and Sliding Experiments in Brittle Matrix Composites," *Acta Metall. Mater.*, Vol. 40, pp. 427–441.

Marshall, D.B., Cox, B.N. and Evans, A.G., 1985, "The Mechanics of Matrix Cracking in Brittle-Matrix Fiber Composites," *Acta Metall. Mater.*, Vol. 33, pp. 2013–2021.

Marshall, D.B. and Evans, A.G., 1985, "Failure Mechanisms in Ceramic-Fiber/Ceramic-Matrix Composites," *J. Am. Ceram. Soc.*, Vol. 68, pp. 225–231.

Marshall, D.B. and Oliver, W.C., 1987, "Measurement of Interfacial Mechanical Properties in Fiber-Reinforced Ceramic Composites," *J. Am. Ceram. Soc.*, Vol. 70, pp. 542–548.

Marshall, D.B. and Ritter, J.E., 1987, "Reliability of Advanced Structural Ceramics and Ceramic Matrix Composites–A Review," *Am. Ceram. Soc. Bull.*, Vol. 66, pp. 309–317.

Mauge, C. and Kachanov, M., 1994, "Effective Elastic Properties of an Anisotropic Material with Arbitrarily Oriented Interacting Cracks," *J. Mech. Phys. Sol.*, Vol. 43, pp. 561–584.

Maurisch, T. and Ortiz, M., 1995, submitted to the

McCartney, L.N., 1992, "Mechanics for the Growth of Bridged Cracks in Composite Materials: Part I. Basic Principles," *J. Comp. Tech. Res.*, Vol. 14, pp. 133–147.

Meyer, D.W., Cooper, R.F. and Plesha, M.E., 1993, "High-Temperature Creep and the Interfacial Mechanical Response of a Ceramic Matrix Composite," *Acta Metall. Mater.*, Vol. 41, pp. 3157–3170.

Murty, M.V.R.K., 1964, "The Use of a Single Plane Parallel Plate as a Lateral Shearing Interferometer with a Visible Gas Laser Source," *Appl. Optics*, Vol. 3, pp. 853–857.

Nardone, V.C. and Prewo, K.M., 1988, "Tensile Performance of Carbon-Fibre-Reinforced Glass," *J. Mater. Sci.*, Vol. 23, pp. 168–180.

Needleman, A., 1975, "Bifurcation of Elastic-Plastic Spherical Shells Subject to Internal Pressure," *J. Mech. Phys. Sol.*, Vol. 23, pp. 357–367.

Needleman, A., 1987, "A Continuum Model for Void Nucleation by Inclusion Debonding," *J. Appl. Mech.*, Vol. 54, pp. 525–531.

Needleman, A., 1990, "An Analysis of Tensile Decohesion Along an Interface," *J. Mech. Phys. Sol.*, Vol. 38, pp. 289–324.

Needleman, A., 1990, "An Analysis of Decohesion Along an Imperfect Interface," *Int. J. Fract.*, Vol. 42, pp. 21–40.

Nemat-Nasser, S. and Hori, M., 1993, *Micromechanics: Overall Properties of Heterogeneous Materials.* New York: North-Holland.

Newmark, N.M., 1959, "A Method of Computation for Structural Dynamics," *J. Eng. Mech. Div.*, Vol. ASCE, pp. 67–94.

Olesiak, Z. and Wnuk, M., 1968, "Plastic Energy Dissipation Due to a Penny-Shaped Crack," *Int. J. Fracture Mech.*, Vol. 4, pp. 383–395.

Ortiz, M., 1995, California Institute of Technology, Personal Communication.

Ortiz, M. and Suresh, S., 1993, "Statistical Properties of Residual Stresses and Intergranular Fracture in Ceramic Materials," *J. Appl. Mech.*, Vol. 60, pp. 77–84.

Pagano, N.J., 1992, Wright-Patterson AFB, Dayton, Ohio, Personal Communication.

Pagano, N.J. and Brown, H.W., 1993, "The Full-Cracking Mode in Unidirectional Brittle-Matrix Composites," *Composites*, Vol. 24, pp. 69–83.

Palaniswamy, K. and Knauss, W.G., 1978, *Mechanics Today*, S. Nemat-Nasser, Eds., Vol. 4, pp. 87–148.

Park, Y.H. and Holmes, J.W., 1992, "Finite Element Modelling of Creep Deformation in Fibre-Reinforced Ceramic Composites," *J. Mater. Sci.*, Vol. 27, pp. 6341–6351.

Parthasarathy, T.A., Jero, P.D. and Kerans, R.J., 1991, "Extraction of Interface Properties from a Fiber Push-Out Test," *Scr. Met. Mat.*, Vol. 25, pp. 2457–2462.

Phillips, D.C., 1974, "Interfacial Bonding and the Toughness of Carbon Fiber Reinforced Glass and Glass-Ceramics," *J. Mater. Sci.*, Vol. 9, pp. 1847–54.

Press, W.H., Flannery, B.P., Teukolsky, S.A. and Vetterling, W.T., 1988, *Numerical Recipes: The Art of Scientific Computing.* Cambridge: Cambridge University Press.

Prewo, K.M. and Brennan, J.J., 1980, "High Strength Silicon Carbide Fibre-Reinforced Glass-Matrix Composites," *J. Mater. Sci.*, Vol. 15, pp. 463–468.

Prewo, K.M., Johnson, B. and Starrett, S., 1989, "Silicon Carbide Fibre-Reinforced Glass-Ceramic Composite Tensile Behavior at Elevated Temperature," *J. Mater. Sci.*, Vol. 24, pp. 1373–1379.

Pryce, A.W. and Smith, P.A., 1992, "Behavior of Unidirectional and Cross-Ply Ceramic Matrix Composites Under Quasi-Static Tensile Loading," *J. Mater. Sci.*, Vol. 27, pp. 2695–2704.

Rosakis, A.J., 1993, "Application of Coherent Gradient Sensing (CGS) to the Investigation of Dynamic Fracture Problems," *Optics and Lasers in Eng.*, Vol. 19, pp. 3–41.

Sørensen, B.F., 1993, "Effect of Fibre Roughness on the Overall Stress-Transverse Strain Response of Ceramic Composites," *Scr. Met. Mat.*, Vol. 28, pp. 435–439.

Sørensen, B.F., Talreja, R. and Sørensen, O.T., 1992, "Damage Development in a Ceramic Matrix Composite under Mechanical Loading," *Proc. 5th European Conf. on Comp. Mater.*, A.R. Bunsell, J.F. Jamet and A. Massiah, Eds., ECCM-5, Bordeaux, France, April 7-10, pp. 129–139.

Spearing, S.M. and Zok, F.W., 1993, "Stochastic Aspects of Matrix Cracking in Brittle Matrix Composites," *J. Eng. Mat. Tech.*, Vol. 115, pp. 314–318.

Stuart, R., 1992, Corning Inc., Corning, New York, Personal Communication.

Tada, H., 1973, *The Stress Analysis of Cracks Handbook.* Pennsylvania: Del Research Corporation.

Talreja, R., 1991, "Continuum Modelling of Damage in Ceramic Matrix Composites," *Mech. Mater.*, Vol. 12, pp. 165–180.

Termonia, Y., 1992, "Effect of Strain Rate on the Mechanical Properites of Composites with a Weak Fibre/Matrix Interface," *J. Mater. Sci.*, Vol. 27, pp. 4878–4882.

Tippur, H.V., 1992, "Coherent Gradient Sensing – A Fourier Optics Analysis and Applications to Fracture," *Appl. Optics*, Vol. 31, pp. 4428–4439.

Tippur, H.V., Krishnaswamy, S. and Rosakis, A.J., 1991, "Optical Mapping of Crack Tip Deformations Using the Methods of Transmission and Reflection Coherent Gradient Sensing – A Study of Crack Tip K-Dominance," *Int. J. Fract.*, Vol. 52, pp. 91–117.

Tippur, H.V. and Rosakis, A.J., 1991, "Quasi-Static and Dynamic Crack-Growth Along Bimaterial Interfaces – A Note on Crack-Tip Field-Measurements Using Coherent Gradient Sensing," *Exp. Mech.*, Vol. 31, pp. 243–251.

Tvergaard, V., 1990, "Effect of Fibre Debonding in a Whisker-Reinforced Metal," *Mat. Sci. Eng.*, Vol. A125, pp. 203–213.

Ungsuwarungsri, T. and Knauss, W.G., 1987, "The Role of Damage-Softened Material Behavior in the Fracture of Composites and Adhesives," *Int. J. Fract.*, Vol. 35, pp. 221–241.

Ungsuwarungsri, T. and Knauss, W.G., 1988, "A Nonlinear Analysis of an Equilibrium Craze: Part II–Simulations of Craze and Crack Growth," *J. Appl. Mech.*, Vol. 55, pp. 52–58.

Vaidya, R.U. and Chawla, K.K., 1994, "Effect of Strain Rate on the Fracture of Ceramic Fibre Reinforced Glass Matrix Composites," *J. Mater. Sci.*, Vol. 29, pp. 3535–3541.

Walter, M.E. and Ravichandran, G., 1995, "An Experimental Investigation of Damage Evolution in a Ceramic Matrix Composite," *J. Eng. Mat. Tech.*, Vol. 117, pp. 101–108.

Wang, A.S.D., Huang, X.G. and Barsoum, M.W., 1992, "Matrix Crack Initiation in Ceramic Matrix Composites Part II: Models and Simulation Results," *Comp. Sci. Tech.*, Vol. 44, pp. 271–282.

Wang, S-W. and Parvizi-Majidi, A., 1992, "Experimental Characterization of the Tenisile Behavior of Nicalon Fibre-Reinforced Calcium Aluminosilicate Composites," *J. Mater. Sci.*, Vol. 27, pp. 5483–5496.

Weber, C.H., Lofvander, J.P.A. and Evans, A.G., 1994, "Creep Anisotropy of a Continuous-Fiber-Reinforced Silicon-Carbide Calcium Aluminosilicate Composite," *J. Am. Ceram. Soc.*, Vol. 77, pp. 1745–1752.

Weihs, T.P. and Nix, W.D., 1991, "Experimental Examination of the Push-Down Technique for Measuring the Sliding Resistance of Silicon Carbide Fibers in a Ceramic Matrix," *J. Am. Ceram. Soc.*, Vol. 74, pp. 542–534.

Weitsman, Y. and Zhu, H., 1993, "Multi-Fracture of Ceramic Composites," *J. Mech. Phys. Sol.*, Vol. 41, pp. 351–388.

Wijeyewickrema, A.C. and Keer, L.M., 1991, "Matrix Fracture in Brittle Matrix Fiber-Reinforced Composites," *Int. J. Sol. Struct.*, Vol. 28, pp. 43–65.

Wooh, S-C. and Daniel, I.M., 1994, "Real-Time Ultrasonic Monitoring of Fiber-Matrix Debonding in Ceramic-Matrix Composite," *Mech. Mater.*, Vol. 17, pp. 379–388.

Wu, X. and Holmes, J.W., 1993, "Tensile Creep and Creep-Strain Recovery Behavior of Silicon Carbide Fiber/Calcium Aluminosilicate Matrix Ceramic Composites," *J. Am. Ceram. Soc.*, Vol. 76, pp. 2695–2700.

Xia, Z.C. and Hutchinson, J.W., 1994, "Matrix Cracking of Cross-Ply Ceramic Composites," *Acta Metall. Mater.*, Vol. 42, pp. 1933–1945.

Xu, G., Argon, A.S. and Ortiz, M., 1995, "Nucleation of Dislocations from Crack Tips under Mixed-Modes of Loading — Implications for Brittle against Ductile Behavior of Crystals," *Phil. Mag.*, Vol. 72, pp. 415–451.

Xu, G., Bower, A.F. and Ortiz, M., 1994, "Three-Dimensional Analysis of Crack Propagation in Fiber-Reinforced Brittle Matrix Composites," *Fracture and Damage in Quasibrittle Structures*, Z.P. Bazant, Z. Bittnar, M. Jirasek and J. Mazars, Eds., London, E&FN, pp. 589–602.

Xu, X-P. and Needleman, A., 1993, "Void Nucleation by Inclusion Debonding in a Crystal Matrix," *Modelling Simul. Mater. Sci. Eng.*, Vol. 1, pp. 111–132.

Zhu, H. and Weitsman, Y., 1994, "The Progression of Failure Mechanisms in Unidirectionally Reinforced Ceramic Composites," *J. Mech. Phys. Sol.*, Vol. 42, pp. 1601–1632.

APPENDIX A

ASTM Standard on Bending

The bending strain at the mid-point of a tensile specimen is commonly calculated as a percentage of the axial strain. The axial strain is defined as the average value of four different strain readings ($\epsilon_1 - \epsilon_4$) on the mid-point of the specimen gage section:

$$\epsilon_a = \frac{\epsilon_1 + \epsilon_2 + \epsilon_3 + \epsilon_4}{4}.$$

If ϵ_1 and ϵ_3 measure strain on opposite sides of the specimen, the bending strain is defined (ASTM Standard E-1012, 1993) as:

$$\epsilon_b = \frac{|\epsilon_1 - \epsilon_3| - |\epsilon_2 - \epsilon_4|}{2},$$

where $|\quad|$ denotes absolute value. Thus the normalized percent bending is:

$$\epsilon_{pct} = \frac{\epsilon_b}{\epsilon_a} \times 100.$$

APPENDIX B

Acoustic Emission Setup

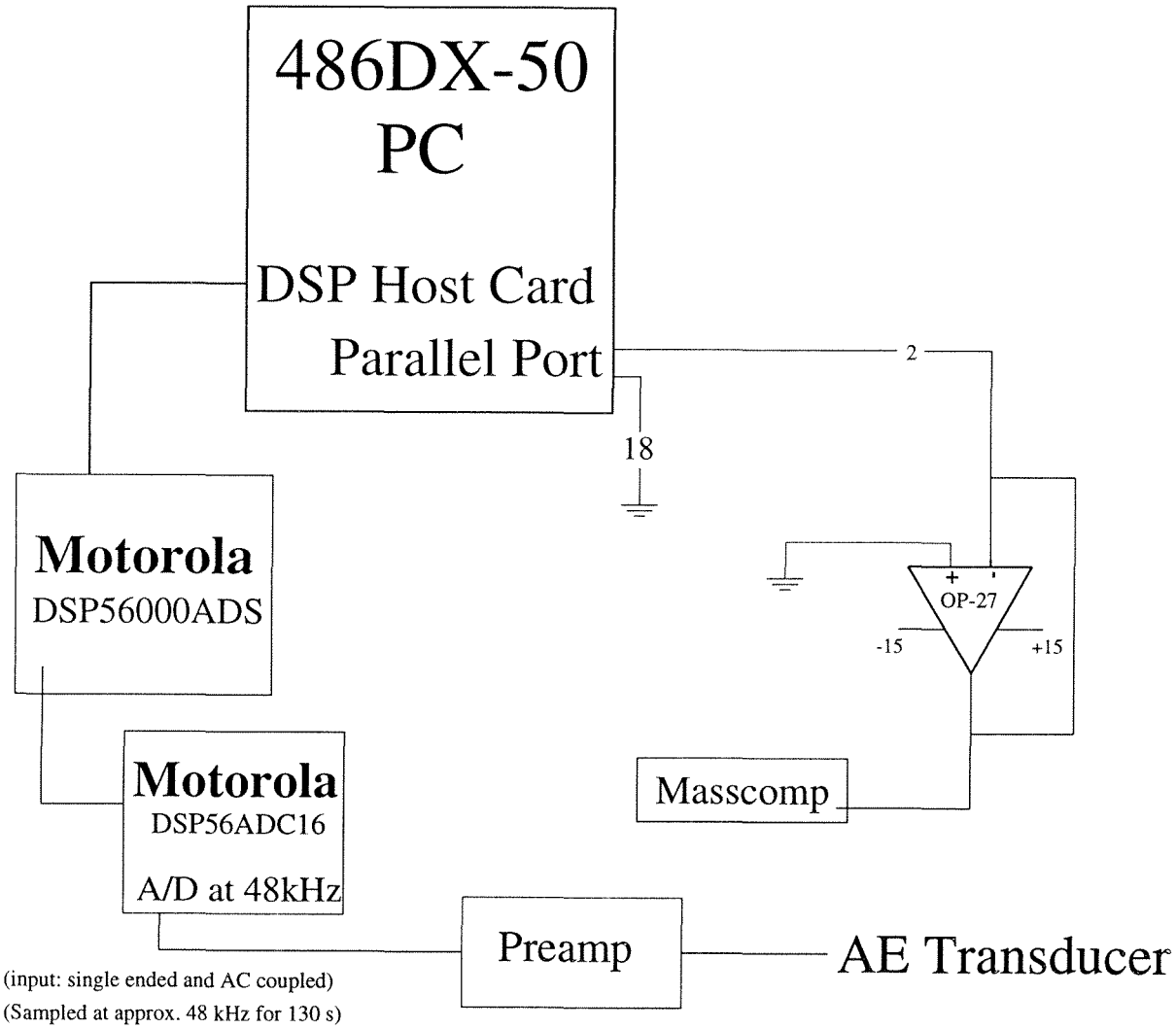

APPENDIX C

Ultrasonics Setup

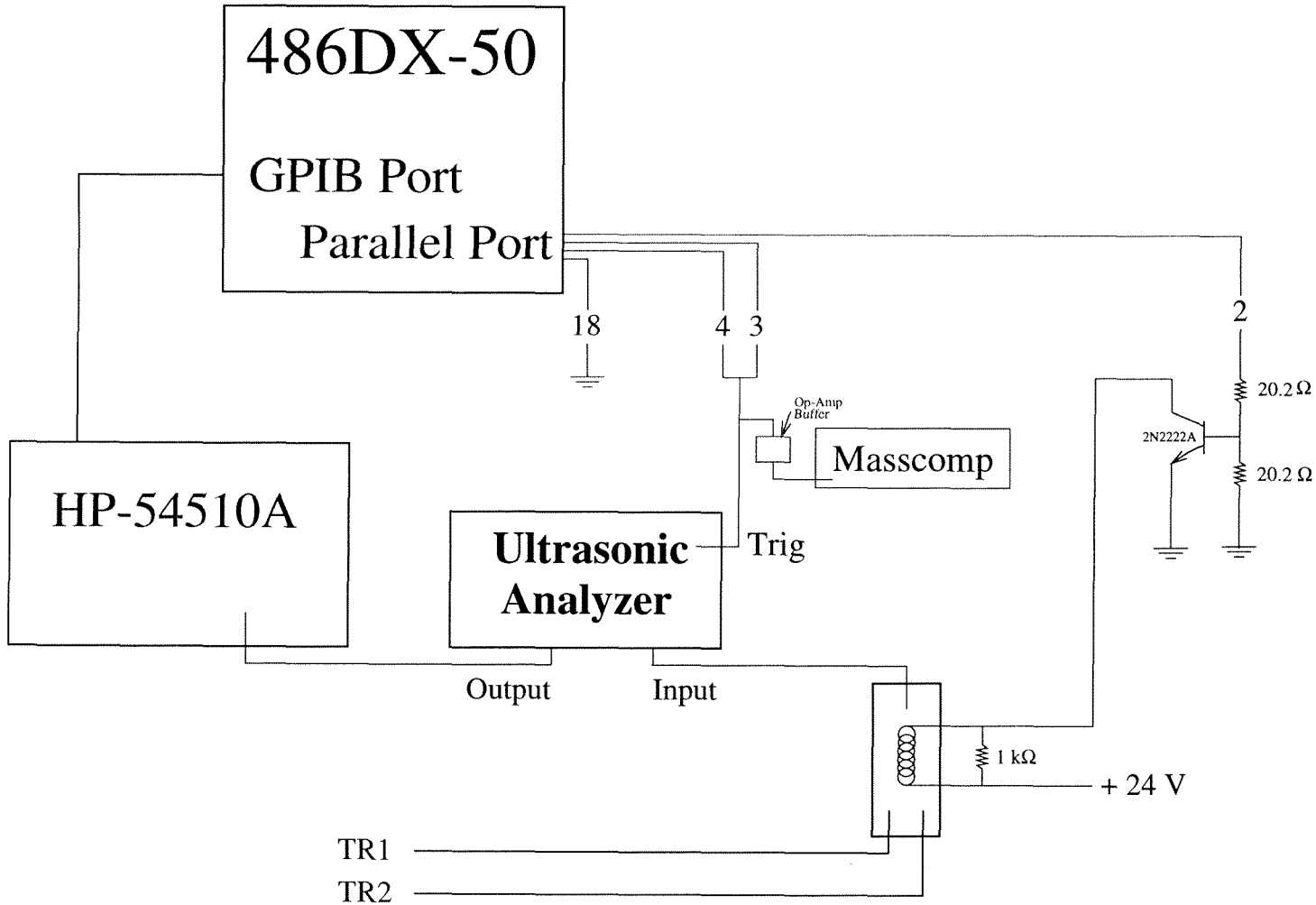

APPENDIX D

LVDT Driver Electronics